NASA/TM-2003-21621/Rev-Vol III

James L. Mueller, Giulietta S. Fargion and Charles R. McClain, Editors
J. L. Mueller, Andre Morel, Robert Frouin, Curtiss Davis, Robert Arnone, Kendall Carder, Z.P. Lee, R.G. Steward, Stanford Hooker, Curtis D. Mobley, Scott McLean, Brent Holben, Mark Miller, Christophe Pietras, Kirk D. Knobelspiesse, Giulietta S. Fargion, John Porter and Ken Voss, Authors.

Ocean Optics Protocols For Satellite Ocean Color Sensor Validation, Revision 4, Volume III:

Radiometric Measurements and Data Analysis Protocols

National Aeronautical and
Space administration

Goddard Space Flight Space Center
Greenbelt, Maryland 20771

January 2003

NASA/TM-2003-

Ocean Optics Protocols For Satellite Ocean Color Sensor Validation, Revision 4, Volume III:

Radiometric Measurements and Data Analysis Protocols

James L. Mueller, CHORS, San Diego State University, San Diego, California
Giulietta S. Fargion, Science Applications International Corporation, Beltsville, Maryland
Charles R. McClain, Goddard Space Flight Center, Greenbelt, Maryland

J. L. Mueller
CHORS, San Diego State University, San Diego, California
Andre Morel
Laboratoire d'Oceanographie, Universite Pierre et Marie Curie, Villefranche-sur-Mer, France
Robert Frouin
Scripps Institution of Oceanography, University of California, San Diego, California
Curtiss Davis
Naval Research Laboratory, Washington, District of Columbia
Robert Arnone
Naval Research Laboratory, Stennis Space Center, Mississippi
Kendall Carder, Z.P. Lee, and R.G. Steward
University of South Florida, St. Petersburg, Florida
Stanford Hooker and Brent Holben
NASA Goddard Space Flight Center, Greenbelt, Maryland
Curtis D. Mobley
Sequoia Scientific Inc., Redmond, Washington
Scott McLean
Satlantic Inc., Halifax, Nova Scotia, Canada
Mark Miller
Department of Applied Science, Brookhaven National Laboratory, Upton, New York
Christophe Pietras and Giulietta S. Fargion
SAIC General Sciences Corporation, Beltsville, Maryland
Kirk D. Knobelspiesse
Science Systems and Applications, Inc., Greenbelt Maryland
John Porter
School of Ocean & Earth Science & Technology, University of Hawaii, Hawaii
Ken Voss
Physics Department, University of Miami, Florida

National Aeronautical and
Space administration

Goddard Space Flight Space Center
Greenbelt, Maryland 20771

January 2003

Preface

This document stipulates protocols for measuring bio-optical and radiometric data for the Sensor Intercomparison and Merger for Biological and Interdisciplinary Oceanic Studies (SIMBIOS) Project activities and algorithm development. The document is organized into 7 separate volumes as:

Ocean Optics Protocols for Satellite Ocean Color Sensor Validation, Revision 4

Volume I: Introduction, Background and Conventions
Volume II: Instrument Specifications, Characterization and Calibration
Volume III: Radiometric Measurements and Data Analysis Methods
Volume IV: Inherent Optical Properties: Instruments, Characterization, Field Measurements and Data Analysis Protocols
Volume V: Biogeochemical and Bio-Optical Measurements and Data Analysis Methods
Volume VI: Special Topics in Ocean Optics Protocols
Volume VII: Appendices

The earlier version of *Ocean Optics Protocols for Satellite Ocean Color Sensor Validation*, *Revision 3* (Mueller and Fargion 2002, Volumes 1 and 2) is entirely superseded by the seven Volumes of Revision 4 listed above.

The new multi-volume format for publishing the ocean optics protocols is intended to allow timely future revisions to be made reflecting important evolution of instruments and methods in some areas, without reissuing the entire document. Over the years, as existing protocols were revised, or expanded for clarification, and new protocol topics were added, the ocean optics protocol document has grown from 45pp (Mueller and Austin 1992) to 308pp in Revision 3 (Mueller and Fargion 2002). This rate of growth continues in Revision 4. The writing and editorial tasks needed to publish each revised version of the protocol manual as a single document has become progressively more difficult as its size increases. Chapters that change but little, must nevertheless be rewritten for each revision to reflect relatively minor changes in, *e.g.*, cross-referencing and to maintain self-contained consistency in the protocol manual. More critically, as it grows bigger, the book becomes more difficult to use by its intended audience. A massive new protocol manual is difficult for a reader to peruse thoroughly enough to stay current with and apply important new material and revisions it may contain. Many people simply find it too time consuming to keep up with changing protocols presented in this format - which may explain why some relatively recent technical reports and journal articles cite Mueller and Austin (1995), rather than the then current, more correct protocol document. It is hoped that the new format will improve community access to current protocols by stabilizing those volumes and chapters that do not change significantly over periods of several years, and introducing most new major revisions as new chapters to be added to an existing volume without revision of its previous contents.

The relationships between the Revision 4 chapters of each protocol volume and those of Revision 3 (Mueller and Fargion 2002), and the topics new chapters, are briefly summarized below:

Volume I: This volume covers perspectives on ocean color research and validation (Chapter 1), fundamental definitions, terminology, relationships and conventions used throughout the protocol document (Chapter 2), requirements for specific *in situ* observations (Chapter 3), and general protocols for field measurements, metadata, logbooks, sampling strategies, and data archival (Chapter 4). Chapters 1, 2 and 3 of Volume I correspond directly to Chapters 1, 2 and 3 of Revision 3 with no substantive changes. Two new variables, Particulate Organic Carbon (POC) and Particle Size Distribution (PSD) have been added to Tables 3.1 and 3.2 and the related discussion in Section 3.4; protocols covering these measurements will be added in a subsequent revision to Volume V (see below). Chapter 4 of Volume I combines material from Chapter 9 of Revision 3 with a brief summary of SeaBASS policy and archival requirements (detailed SeaBASS information in Chapter 18 and Appendix B of Revision 3 has been separated from the optics protocols).

Volume II: The chapters of this volume review instrument performance characteristics required for *in situ* observations to support validation (Chapter 1), detailed instrument specifications and underlying rationale (Chapter 2) and protocols for instrument calibration and characterization standards and methods (Chapters 3 through 5). Chapters 1 through 5 of Volume II correspond directly to Revision 3 chapters 4 through 8, respectively, with only minor modifications.

Volume III: The chapters of this volume briefly review methods used in the field to make the *in situ* radiometric measurements for ocean color validation, together with methods of analyzing the data (Chapter 1), detailed measurement and data analysis protocols for in-water radiometric profiles (Chapter 2), above water measurements of remote sensing reflectance (Chapter III-3), determinations of exact normalized water-leaving radiance (Chapter 4), and atmospheric radiometric measurements to determine aerosol optical thickness and sky radiance distributions (Chapter 5). Chapter 1 is adapted from relevant portions of Chapter 9 in Revision 3. Chapter 2 of Volume III corresponds to Chapter 10 of Revision 3, and Chapters 3 through 5 to Revision 3 Chapters 12 through 14, respectively. Aside from reorganization, there are no changes in the protocols presented in this volume.

Volume IV: This volume includes a chapter reviewing the scope of inherent optical properties (IOP) measurements (Chapter 1), followed by 4 chapters giving detailed calibration, measurement and analysis protocols for the beam attenuation coefficient (Chapter 2), the volume absorption coefficient measured *in situ* (Chapter 3), laboratory measurements of the volume absorption coefficients from discrete filtered seawater samples (Chapter 4), and *in situ* measurements of the volume scattering function, including determinations of the backscattering coefficient (Chapter 5). Chapter 4 of Volume IV is a slightly revised version of Chapter 15 in Revision 3, while the remaining chapters of this volume are entirely new contributions to the ocean optics protocols. These new chapters may be significantly revised in the future, given the rapidly developing state-of-the-art in IOP measurement instruments and methods.

Volume V: The overview chapter (Chapter 1) briefly reviews biogeochemical and bio-optical measurements, and points to literature covering methods for measuring these variables; some of the material in this overview is drawn from Chapter 9 of Revision 3. Detailed protocols for HPLC measurement of phytoplankton pigment concentrations are given in Chapter 2, which differs from Chapter 16 of Revision 3 only by its specification of a new solvent program. Chapter 3 gives protocols for Fluorometric measurement of chlorophyll *a* concentration, and is not significantly changed from Chapter 17of Revision 3. New chapters covering protocols for measuring, Phycoerythrin concentrations, Particle Size Distribution (PSD) and Particulate Organic Carbon (POC) concentrations are likely future additions to this volume.

Volume VI: This volume gathers chapters covering more specialized topics in the ocean optics protocols. Chapter 1 introduces these special topics in the context of the overall protocols. Chapter 2 is a reformatted, but otherwise unchanged, version of Chapter 11 in Revision 3 describing specialized protocols used for radiometric measurements associated with the Marine Optical Buoy (MOBY) ocean color vicarious calibration observatory. The remaining chapters are new in Revision 4 and cover protocols for radiometric and bio-optical measurements from moored and drifting buoys (Chapter 3), ocean color measurements from aircraft (Chapter 4), and methods and results using LASER sources for stray-light characterization and correction of the MOBY spectrographs (Chapter 5). In the next few years, it is likely that most new additions to the protocols will appear as chapters added to this volume.

Volume VII: This volume collects appendices of useful information. Appendix A is an updated version of Appendix A in Revision 3 summarizing characteristics of past, present and future satellite ocean color missions. Appendix B is the List of Acronyms used in the report and is an updated version of Appenix C in Revision 3. Similarly, Appendix C, the list of Frequently Used Symbols, is an updated version of Appendix D from Rev. 3. The SeaBASS file format information given in Appendix B of Revision 3 has been removed from the protocols and is promulgated separately by the SIMBIOS Project.

In the Revision 4 multi-volume format of the ocean optics protocols, Volumes I, II and III are unlikely to require significant changes for several years. The chapters of Volume IV may require near term revisions to reflect the rapidly evolving state-of-the-art in measurements of inherent optical properties, particularly concerning instruments and methods for measuring the Volume Scattering Function of seawater. It is anticipated that new chapters will be also be added to Volumes V and VI in Revision 5 (2003).

This technical report is not meant as a substitute for scientific literature. Instead, it will provide a ready and responsive vehicle for the multitude of technical reports issued by an operational Project. The contributions are published as submitted, after only minor editing to correct obvious grammatical or clerical errors.

Table of Contents

CHAPTER 1 ..... **1**

OVERVIEW OF RADIOMETRIC MEASUREMENT AND DATA ANALYSIS METHODS

1.1 INTRODUCTION 1
1.2 IN-WATER RADIOMETRIC PROFILES 1
1.3 ABOVE-WATER REMOTE-SENSING REFLECTANCE 1
1.4 NORMALIZED WATER-LEAVING RADIANCE AND REMOTE-SENSING REFLECTANCE: BIDIRECTIONAL REFLECTANCE AND OTHER FACTORS 3
1.5 SUN AND SKY RADIANCE MEASUREMENTS 3
1.6 FUTURE DIRECTIONS 4
REFERENCES 5

CHAPTER 2 ..... **7**

IN-WATER RADIOMETRIC PROFILE MEASUREMENTS AND DATA ANALYSIS PROTOCOLS.

2.1 INTRODUCTION 7
2.2 MEASUREMENT METHODS 7
Ship Shadow Avoidance 8
Depth Resolution in Profiles 9
Instrument Dark Readings 9
Surface Incident Irradiance 9
Instrument Attitude 10
2.3 ANCILLARY MEASUREMENTS AND LOGS 10
2.4 DATA ANALYSIS METHODS 10
Dark Corrections 11
Instrument Calibration Analysis 11
Depth Offset Adjustments 12
Profile Normalization by Surface Irradiance 12
K-Analysis 13
Extrapolation to the Sea Surface 14
Instrument Self-Shading 15
Finite Bandwidth Correction 18
Raman Corrections 18
REFERENCES 19

CHAPTER 3 ..... **21**

ABOVE-WATER RADIANCE AND REMOTE SENSING REFLECTANCE MEASUREMENT AND ANALYSIS PROTOCOLS

3.1 INTRODUCTION 21
3.2 PROPOSED MEASUREMENT CONCEPTS 22
Method 1: Calibrated radiance and irradiance measurements 22
Method 2: Uncalibrated radiance and reflectance plaque measurements 23
Method 3: Calibrated surface polarized radiance measurements with modeled irradiance and sky radiance 23
Exact Normalized Remote Sensing Reflectance 23
3.3 RADIOMETRIC MEASUREMENT METHODS 23
Field of View Considerations 23
Radiance Measurements 24
Incident Irradiance Measurements 25
Reflectance Plaque Measurements 26
Sun Photometer Measurements 26
Ancillary Measurements and Records 26
3.4 SKY RADIANCE REFLECTANCE OF THE SEA SURFACE 27
Clear Skies 27
Scattered and Broken Clouds 28
Overcast Skies 28

Residual Reflectance Corrections 28
3.5 DISCUSSION AND RECOMMENDATIONS 29
REFERENCES 30

CHAPTER 4 32

NORMALIZED WATER-LEAVING RADIANCE AND REMOTE SENSING REFLECTANCE: BIDIRECTIONAL REFLECTANCE AND OTHER FACTORS
4.1 NOTATIONS AND FUNDAMENTAL DEFINITIONS 32
4.2 PHYSICAL PHENOMENA AT THE INTERFACE 34
4.3 THE IN-WATER RADIANT FIELD: PHYSICAL CONSIDERATIONS 35
Fluorescence and Raman Scattering 38
4.4 PRACTICAL CONSIDERATIONS: THE f, Q AND $\Re$ FACTORS 40
Basic relationships 40
Expressing slant water-leaving radiances 41
4.5 IMPLICATIONS OF BIDIRECTIONALITY IN REMOTE SENSING 42
Satellite remotely sensed radiances 43
Field measurements 44
Other useful relationships 44
4.6 GENERATION AND BEHAVIOR OF THE $\Re$, f, AND Q QUANTITIES 45
The reflection-refraction term $\Re$ 45
Prediction of the f and Q factors 45
Variations of the f-factor 46
Variations of the bidirectional function Q 47
Variations of the f/Q ratio 53
4.7. CORRECTION PROCEDURES FOR BIDIRECTIONALITY 56
REFERENCES 58

CHAPTER 5 60

SUN AND SKY RADIANCE MEASUREMENTS AND DATA ANALYSIS PROTOCOLS
5.0 INTRODUCTION 60
5.1 AUTOMATIC SUN PHOTOMETER AND SKY RADIANCE SCANNING SYSTEMS 60
Description 61
Installation 62
Measurement Protocols 62
Data Analysis 63
Sky radiance Inversion Products 64
Quality Control 64
5.2 SKY RADIANCE DISTRIBUTION CAMERA SYSTEMS 65
Measurement Protocols 65
Data Analysis Protocols 66
5.3 HAND-HELD SUN PHOTOMETERS 66
Installation and Maintenance 67
Measurement Protocols 68
Data Analysis 69
5.4 FAST-ROTATING SHADOW-BAND RADIOMETERS 69
Installation and Maintenance 70
Data Analysis 70
5.5 SIMBIOS PROJECT AOT EXTRACTION PROTOCOLS 72
Extraction of in situ AOT 72
REFERENCES 73

Chapter 1

Overview of Radiometric Measurement and Data Analysis Methods

James L. Mueller

Center for Hydro-Optics and Remote Sensing, San Diego State University, California

1.1 INTRODUCTION

The chapters of this volume cover protocols for determining ***water-leaving radiance*** from shipboard radiometric measurements in-water (Chapter 2) and above-water (Chapter 3). Protocols for determining ***exact normalized water-leaving radiance*** from measured water-leaving radiance are presented in Chapter 4. Finally, protocols for deriving ***aerosol optical depth***, and other ***atmospheric optical properties***, from atmospheric radiometric measurements are described in Chapter 5. Chapters 2 through 5 correspond, respectively, to Chapters 10, 12, 13 and 14 of Revision 3 to the ocean optics protocols document (Mueller and Fargion 2002).

Protocols covering methods for deriving water-leaving radiance from radiometer arrays mounted on buoys are covered in Volume VI, Chapters 2 and 3. Determinations of water-leaving radiance from radiometric measurements on aircraft are discussed in Volume VI, Chapter4.

1.2 IN-WATER RADIOMETRIC PROFILES

Methods for measuring radiometric profiles of spectral upwelled radiance $L_u(z,\lambda)$, downward irradiance $E_d(z,\lambda)$, upward irradiance $E_u(z,\lambda)$ and surface incident irradiance $E_S[t(z),\lambda]$ (above-water) are presented in Chapter 2. The notation $t(z)$ indicates that $E_S[t(z),\lambda]$ is measured simultaneously with the underwater measurements at depth z. The content of this chapter is largely derived from Mueller and Austin (1995), but the presentation was reorganized in Revision 2 of the protocols (Fargion and Mueller 2000), where it appeared as Chapter 9, to treat the topic in a more unified way. Subsequently, there have been only minor editorial changes in this chapter in its appearance as Chapter 10 in Revision 3 (Mueller and Fargion 2002) and here in Revision 4 as Volume III, Chapter 2.

The in-water radiometric measurement methods protocols address ship shadow avoidance, depth resolution in profiles, acquisition of instrument dark readings, and instrument attitude alignment. The protocols identify ancillary measurement and metadata to be acquired and recorded in a log during each radiometric profile measurement. Data analysis recommendations include methods for determining of the respective diffuse attenuation coefficients $K_L(z, \lambda)$, $K_d(z, \lambda)$ and $K_u(z, \lambda)$ profiles, extrapolating $L_u(z, \lambda)$ to the surface to determine $L_u(0^-, \lambda)$ and its transmission through the interface to estimate water-leaving radiance $L_W(\lambda)$ and remote sensing reflectance $R_{RS}(\lambda)$. The omission of directional notation in these quantities (*cf.* below) indicates they are oriented normal to the sea surface, *e.g.* $L_W(\lambda)$ is emitted from the surface in the zenith direction $\theta = 0$. The analysis protocols also address application of instrument calibration factors, dark corrections and depth offsets, as well as a recommended method for instrument self-shading corrections of $L_u(0^-,\lambda)$. The effects that finite bandwidths and Raman scattering have on the radiometric quantities are briefly reviewed, but the present version of the protocols does not include a recommended method for corrections related to either phenomenon. Methods for including Raman scattering corrections in the computation of exact water-leaving radiance $L_{WN}^{ex}(\lambda)$ from $L_W(\lambda)$ are described in Volume III, Chapter 4.

1.3 ABOVE-WATER REMOTE-SENSING REFLECTANCE

Volume III, Chapter 3 presents the provisional protocols for deriving water-leaving radiance from above-water measurements of total radiance leaving the sea surface at a given zenith and azimuth angle, and of sky radiance at associated zenith and azimuth angles. The contents of Chapter 3 have not changed significantly from Revision 2 to the protocols (Fargion and Mueller 2000), where it appeared as Chapter 10, or from Chapter 12 in Revision 3

(Mueller and Fargion 2002). The Mueller and Austin (1995) provisional protocols for above-water radiometric measurements are seriously flawed and should not be used under any circumstances.

Proposed protocols are reviewed in Volume III, Chapter 3 for deriving water-leaving radiance $L_w(\lambda,\theta,\phi \in \Omega_{FOV};\theta_o)$ and remote-sensing reflectance $R_{RS}(\lambda,\theta,\phi \in \Omega_{FOV};\theta_o)$ from above-water measurements of radiance emitted from the sea surface and sky at zenith and azimuth angles (θ,ϕ) and $(\theta_{sky},\phi_{sky})$, respectively, with the sun at zenith angle θ_o. In the convention adopted for these protocols, azimuth angles ϕ are measured relative to the sun's azimuth. The explicit directional notation used in this context arises, because of the directional nature of skylight reflection (Volume III, Chapter 3) and the bidirectional nature of ocean's remote sensing reflectance (Volume III, Chapter 4). Both $L_w(\lambda,\theta,\phi \in \Omega_{FOV};\theta_o)$ and $R_{RS}(\lambda,\theta,\phi \in \Omega_{FOV};\theta_o)$ are Apparent Optical Properties (AOP), which for any combination of Inherent Optical Properties (IOP) in a water mass, are dependent on the incident radiance distribution at the sea surface. For clear sky conditions, variations in surface radiance distribution are governed primarily by variations in solar zenith angle θ_o and aerosol types and amounts. For a given radiance distribution, the radiance measurements are sensitive to the observation angles (θ,ϕ) relative to the sun's principal plane and the unit vector normal to the sea surface, and to a lesser extent, to the magnitude of the radiometer's solid angle field of view Ω_{FOV} sr.

Chapter 3 (Volume III) is organized around 3 alternative proposed $R_{RS}(\lambda,\theta,\phi \in \Omega_{FOV};\theta_o)$ measurement concepts:

1. Calibrated radiance and irradiance measurements;
2. Uncalibrated radiance and reflectance plaque measurements; and
3. Calibrated polarized surface radiance measurements with modeled irradiance and sky radiance.

The discussion of provisional protocols for measurement and analysis methods distinguish between special considerations applicable to methods 1, 2 and 3. Required ancillary measurements include sun photometer measurements of aerosol optical depth, wind speed and direction, and cloud conditions – variables of special significance for removing reflected sky radiance from the measured surface radiance. The sky radiance reflectance of the sea surface, its sensitivity to (θ,ϕ) and θ_o, and proposed methods for estimating it under clear and cloudy sky conditions, are reviewed in Section 3.4 of Volume III, Chapter 3.

Currently, there is no firm basis for recommending any of the three proposed measurement concepts, and the protocols remain provisional in many respects. For any of the three methods, recommended viewing angles are (θ, ϕ) = (40°, 135°). Specific recommendations are also made regarding preferred methods for estimating skylight reflectance under clear and overcast sky conditions; corrections for skylight reflectance under partially cloudy skies are problematic.

The specific recommendations for viewing angles and skylight correction methods are not unanimously endorsed by the co-authors of Chapter 3. Z.P. Lee (personal comm.), for example, takes strong exception to the superiority of the $\theta = 40^o$ viewing angle, especially at wind speeds > 5 m s^{-1} using a radiometer with a 20° FOV (full-angle). In this context, he points out correctly, that the angular and wind-speed dependencies of the reflectance of the sea surface are both much stronger in the range $30° \le \theta \le 40°$ than they are in the range $20° \le \theta \le 40°$. The angular and wind speed W dependencies of surface reflectance $\rho(\theta,\theta',W)$ closely resemble the inverse of the function $\Re(\theta',\theta,W)$ (Volume III, Chapter 4, Figure 4.4), as these attributes of that function are dominated by the factor $[1-\rho(\theta',\theta,W)]$ and $\rho(\theta,\theta',W)=\rho(\theta',\theta,W)$. It is apparent that viewing angle and wind-speed related uncertainties of both skylight reflection from, and upward radiance transmission through, the interface are much larger at the larger viewing angles. As a partial exception to this criticism, a 20° FOV is probably too large for either pointing angle, but the point is otherwise well taken.

There are other comments and criticisms, both from co-authors of Chapter 3 and others, which should be addressed to update and revise the protocols for above-water radiometric measurements and analyses in a future revision to this protocol document. Such revisions must be preceded, however, first by more definitive determinations than have been realized to date of the uncertainty budgets of the proposed methods, and then by

proceedings of some forum convened to discern that a new consensus on this topic has emerged within the ocean color research community.

1.4 NORMALIZED WATER-LEAVING RADIANCE AND REMOTE-SENSING REFLECTANCE: BIDIRECTIONAL REFLECTANCE AND OTHER FACTORS

The water-leaving radiances and remote-sensing reflectances derived by the measurement methods of Volume III, Chapters 2 and 3 are AOP that vary as functions of the solar zenith angle θ_o, the radiance viewing azimuth and zenith angles (θ, ϕ), the earth-sun distance d on a particular day of the year, the transmission of the sun through the earth's atmosphere, and the ocean's Bidirectional Reflectance Distribution Function (BRDF) (Morel and Gentili 1990, 1993, 1996; Morel *et al*. 1995). The ocean's BRDF is a function of the sea state and seawater IOP: $a(\lambda)$, $b(\lambda)$, $b_b(\lambda)$ and scattering phase function $\beta(\lambda,\Psi)/b(\lambda)$. Volume III, Chapter 4 reviews the physical process at the interface and in the water that act, in concert with the vector radiance field transmitted across the interface, to create the ocean BRDF. These processes lead, in turn to the bidirectional properties of water-leaving radiance $L_W(\lambda,\theta,\phi)$, normalized water-leaving radiance $L_{WN}(\lambda)$ (Gordon and Clark 1981), and remote-sensing reflectance $R_{RS}(\lambda,\theta,\phi;\theta_o)$ (Volume III, Chapter 3). A general method is presented, by which radiative transfer solutions for particular boundary conditions (the downward radiance field above the surface and the wind speed dependent surface reflectance) and IOP profiles, may be used to transform $L_{WN}(\lambda)$ to exact normalized water-leaving radiance $L_{WN}^{ex}(\lambda)$, which no longer has bidirectional properties. For vertically homogeneous Case-1 waters with $Chl \leq 3$ mg m^{-3}, Chapter 4 also presents and describes in detail the characteristics of a simplified, approximate solution for transforming $L_{WN}(\lambda)$ to $L_{WN}^{ex}(\lambda)$; the IOP are parameterized as functions of *Chl*, and lookup tables are available on-line over the Internet (Morel and Maritorena 2001). Aside from numbering changes, and correction of a few typographic errors, the contents of Volume III, Chapter 4 (Revision 4) are taken verbatim from Chapter 13 of Revision 3 (Mueller and Fargion 2002).

1.5 SUN AND SKY RADIANCE MEASUREMENTS

Volume III, Chapter 5 covers protocols for measurements to determine the optical thickness of the atmosphere, and atmospheric optical properties derived from sky radiance distributions. Protocols for atmospheric radiometric measurements were addressed only superficially in Mueller and Austin (1995). A new chapter on this subject first appeared as Chapter 11 in Revision 2 to these protocols (Fargion and Mueller 2000), and then with modest editorial revisions as Chapter 14 in Revision 3 (Mueller and Fargion 2002). This material appears here as Volume III, Chapter 5, again with editorial corrections and renumbering. Equation (14.6) in Chapter 14 of Revision 3 (Mueller and Fargion 2001), giving the Rayleigh optical thickness of the standard atmosphere, was written incorrectly (both in form and values of coefficients); the correct relationship appears here as equations (5.16) and (5.17) (Volume III, Chapter 5). There are no other significant changes from Chapter 14 of Revision 3 (Mueller and Fargion 2002).

Chapter 5 provides detailed protocols for two types of radiometric measurements essential to verify atmospheric correction algorithms and to calibrate vicariously satellite ocean color sensors. The first type is a photometric measurement of the direct solar beam to determine the optical thickness of the atmosphere. The intensity of the solar beam can be measured directly, or obtained indirectly from shadow-band radiometer measurements of diffuse global upper hemispheric irradiance. The second type is a measurement of the solar aureole and sky radiance distribution using a radiance distribution camera, or a scanning radiometer viewing in and perpendicular to the solar principal plane. From the two types of measurements, the optical properties and concentration of aerosols can be derived.

Chapter 5 presents measurement protocols for radiometers commonly used to measure direct atmospheric transmittance and sky radiance, namely standard sun photometers, fast-rotating shadow-band radiometers, automating sky scanning systems, and CCD cameras. Discussed are methods and procedures to analyze and maintain quality control over the data, as well as proper measurement strategies for evaluating atmospheric correction algorithms and satellite-derived ocean color products.

1.6 FUTURE DIRECTIONS

Within each of the protocol topics presented in this Volume, there are several areas where additional research is needed to resolve open questions, better determine uncertainty budgets and/or improve the recommended measurement and analysis methods. Topics generally recognized as needing improvement include those described below for each chapter.

Other closely related protocol topic areas are widely recognized as needing improvements, but they do not fall cleanly within any one of the chapters presented here. One example of such a topic is the determination and interpretation of water-leaving radiance from optically shallow water-masses over a reflecting bottom (Hamilton *et al*. 1993; Lee *et al*. 1998, 1999). Another example concerns methods of determining of water-leaving radiance, its uncertainty budget, and its interpretation in very turbid Case 1 and Case 2 water-masses; the more promising candidate approaches to this problem area may well include some combination of in-water and above-water radiometry (e.g. Toole *et al*. 2000) with *in situ* IOP measurements (Volume IV).

Chapter 2: In-Water Radiometry

The need to ***extrapolate*** $\mathbf{L_u}(z,\boldsymbol{\lambda})$ ***upward to determine*** $\mathbf{L_u}(\mathbf{0}^-,\boldsymbol{\lambda})$ is a significant, but poorly understood, source of uncertainty in water-leaving radiance derived from in-water radiometric measurements. As discussed in Section 2.4, the uppermost usable readings in $L_u(z,\lambda)$ profiles are typically in the depth interval $0.5\text{ m} \lesssim z \lesssim 2\text{ m}$, where focusing and defocusing of incident radiance by surface waves typically causes large temporal and spatial variations in $E_d(z,\lambda)$ and $L_u(z,\lambda)$ (bright flashes and shadow-like features) (Zaneveld *et al*. 2001). Cloud cover variations within and between individual profiles, acting through changes in the surface radiance distribution, are a second important source of variability that cannot be completely accounted for by above-water measurements of $E_S(\lambda)$. Variations in the surface slope distribution in response to wind gusts (*e.g*., Cox and Munk 1954) also introduce significant, albeit less obvious, ambient variations in $E_d(z,\lambda)$ and $L_u(z,\lambda)$ profiles. To date, investigations of uncertainty in $L_u(0^-,\lambda)$ and $L_W(\lambda)$ derived from in-water measurements have addressed differences between these quantities derived from selected $L_u(z,\lambda)$ profiles using different methods of analysis in Data Analysis Round Robin (DARR) exercises (Siegel *et al*. 1994; Hooker *et al*. 2002), and comparisons of results from profiles measured using different instrument configuration and deployment methods (Hooker and Maritorena 2000). Neither approach is capable of separating the intrinsic underlying uncertainty due to ambient variability during and between individual measurements from uncertainty associated with different methods of treating the data in its analysis (including subjective judgments by the analyst). Additional research is needed, with possible approaches including more comprehensive DARR evaluations, and new experimental work to improve the statistical characterization of ambient fluctuations of vector radiant fields at and near the air-sea interface.

The provisional protocol for ***instrument self-shading corrections*** of $L_u(0^-,\lambda)$, adapted from Gordon and Ding (1992) and the provisional experimental confirmation by Zibordi and Ferrari (1995), should be extended to more complicated instrument configurations and to account for reflections, as well as shading by the instrument body. The suggested approaches are to model specific sensor aperture and instrument configurations, following the general methodology introduced by Gordon and Ding (1992), and to then pursue controlled experiments extending the methods of Zibordi and Ferrari (1995) to the geometries of those configurations. Instrument configurations for which improved self-shading correction models are needed include:

1. A nadir-viewing sensor aperture located away from the center of a cylindrical instrument housing. The shipboard, profiling version of the Marine Optical System (MOS), used in support of the Marine Optical BuoY (MOBY) observatory (Volume VI, Chapter 2), is one example of such an instrument configuration. Compared to the concentric geometry of the Gordon and Ding (1992) model, this geometry will decrease self-shading when the solar azimuth is on the side of instrument where the aperture is located, and conversely, self-shading will be increased when the solar azimuth is opposite the aperture offset azimuth.
2. An off-center sensor aperture that views outward, at an off-nadir angle, from beneath a cylindrical (or spherical) housing, such as the hull of a bio-optical buoy, for example (Volume VI, Chapter 3).

Intuitively, this viewing geometry offers a further reduction in self-shading when the solar azimuth is within <90° of the sensor offset direction. On the other hand, it is necessary to correct also for the full effect of the ocean's BRDF in this sensor viewing geometry (Volume III, Chapter 4).

3. A small, nadir-viewing sensor aperture mounted on the underside of a narrow, horizontal spar, such as for example, the MOS spectrograph $L_u(z,\lambda)$ heads mounted on MOBY (Volume VI, Chapter 2). This sensor mounting geometry minimizes self-shading of a buoy-mounted sensor for most solar azimuth angles, but it also varies the "instrument's" effective self-shading geometric cross section as a function of solar azimuth angle, as well as solar zenith angle.

Chapter 3: Above-Water Radiometry

The shortcomings of the provisional protocols, and the poorly understood uncertainty budgets of alternative proposed methods, for determining water-leaving radiance from above-water radiometric measurements are outlined above in Section 1.3. The areas requiring further research are discussed in some detail in Chapter 3, together with suggested methods of approaching the problems.

Chapter 4: Normalized Water-Leaving Radiance and the ocean's BRDF

The theory and method for determining exact normalized water-leaving radiance is complete and general as presented in Chapter 4. The approximate implementation using empirical functions of the remote-sensing chlorophyll concentration *Chl* to represent IOP dependence, on the other hand, is limited to homogenous, relatively clear Case 1 water masses with $Chl \leq 3\ \mathrm{mg\ m^{-3}}$. Preliminary analysis of upwelling radiance distribution measurements at the MOBY site suggest that this approximation appears to work reasonably well (~1 % to 2 %) within those limits (K. Voss, Pers. Comm.). Additional solutions are required for application to more turbid Case 1 and Case 2 water masses. Improved representations of the IOP, and in particular the volume scattering phase function, will be necessary to account for BRDF effects on $L_W(\lambda,\theta,\phi,\theta_o)$ in these situations. In Case 2 waters, it may even be necessary to support $L_{WN}^{ex}(\lambda)$ determinations with *in situ* IOP measurements (Volume IV) on a case-by-case basis.

Chapter 5: Atmospheric Radiometric Measurements.

Two areas of ongoing research that are expected to improve the atmospheric protocols are the development of:

1. new methods of analysis to determine aerosol phase functions, and other atmospheric optical properties, from sky radiance distribution measurements, and
2. new methods of cloud screening, and perhaps of sensor attitude determination, in shipboard Fast Response Shadow-band Radiometer (FRSR) data.

REFERENCES

Cox, C. and W. Munk, 1954: Measurement of the roughness of the sea surface from photographs of the sun's glitter. *J. Opt. Soc. Am*. **44**: 11838-11850.

Fargion, G.S. and J.L. Mueller, 2000: Ocean Optics Protocols for Satellite Ocean Color Sensor Validation, Revision 2, *NASA/TM –2001-209955*, NASA Goddard Space Flight Center, Greenbelt, Maryland. 184pp.

Gordon, H.R., and D.K. Clark, 1981: Clear water radiances for atmospheric correction of Coastal Zone Color Scanner imagery. *Appl. Opt*., **20**: 4,175--4,180.

Gordon, H.R., and K. Ding, 1992: Self shading of in-water optical instruments. *Limnol. Oceanogr.,* **37**: 491--500.

Hamilton, M.K., C.O. Davis, W.J. Rhea, S.H. Pilorz, and K.L. Carder, 1993: Estimating chlorophyll content and bathymetry of Lake Tahoe using AVIRIS data. *Remote Sens. Environ.*, **44**: 217--230.

Hooker, S.B. and S. Maritorena, 2000: An evaluation of oceanographic radiometers and deployment methodologies. *J. Atmos. Oceanic Technol*., 17: 811-830.

Hooker, S.B., G. Zibordi, J-F Berthon, D. D'Alimonte, S. Maritorena, S. McLean and J. Sildam, 2001: Results of the Second SeaWiFS Data Analysis Round Robin, March 2000 (DARR-00). *NASA/TM-2001-206892, Vol. 15*, S.B. Hooker and E.R. Firestone [Eds.], NASA Goddard Space Flight Center, Greenbelt, Maryland, 71pp.

Lee, Z.P., K.L. Carder, C.D. Mobley, R.G. Steward and J.S. Patch, 1998: Hyperspectral remote sensing for shallow waters: 1. A semianalytical model. *Appl. Opt*., **37**(27): 6329-6338.

Lee, Z.P., K.L. Carder, C.D. Mobley, R.G. Steward and J.S. Patch, 1999: Hyperspectral remote sensing for shallow waters: 2. Deriving bottom depths and water properties by optimization. *Appl. Opt.*, **38**(18): 3831-3843.

Morel, A. and B. Gentili, 1991: Diffuse reflectance of oceanic waters: its dependence on sun angle as influenced by the molecular scattering contribution. *Applied Optics*. 30(30): 4427-4438.

Morel, A. and B. Gentili, 1993: Diffuse reflectance of oceanic waters. II. Bidirectional aspects. *Appl. Opt*. **32**(33): 6864-6879

Morel, A. and B. Gentilli, 1996: Diffuse reflectance of oceanic waters. III. Implication of bidirectionality for the remote-sensing problem. *Appl. Opt*., **35**(24): 4850-4862.

Morel, A. and S. Maritorena, 2001: Bio-optical properties of oceanic waters: A reappraisal. *J. Geophys. Res.*, **106:** 7163-7180.

Morel, A., K.J. Voss, and B. Gentili, 1995: Bidirectional reflectance of oceanic waters: a comparison of modeled and measured upward radiance fields. *J. Geophys. Res*. **100**: 13,143-13,151.

Mueller, J.L., and R.W. Austin, 1995: Ocean Optics Protocols for SeaWiFS Validation, Revision 1. *NASA Tech. Memo. 104566, Vol. **25,*** S.B. Hooker, E.R. Firestone and J.G. Acker, Eds., NASA Goddard Space Flight Center, Greenbelt, Maryland, 67 pp.

Mueller, J.L., and G.S. Fargion 2002: Ocean Optics Protocols for Satellite Ocean Color Sensor Validation, Revision 3, *NASA/TM –2002-210004*, NASA Goddard Space Flight Center, Greenbelt, Maryland. 308pp.

Siegel, D.A., M.C. O'Brien, J.C. Sorenson, D.A. Konnoff, E.A. Brody, J.L. Mueller, C.O. Davis, W.J. Rhea, and S.B. Hooker, 1995: Results of the SeaWiFS Data Analysis Round Robin, July 1994 (DARR-94). *NASA Tech. Memo. 104566, Vol. **26,*** S.B. Hooker and E.R. Firestone, Eds., NASA Goddard Space Flight Center, Greenbelt, Maryland, 58pp.

Toole, D.A., D.A. Siegel, D.W. Menzies, M.J. Neumann and R.C. Smith, 2000: Remote-sensing reflectance determinations in the coastal ocean environment: impact of instrumental characteristics and environmental variability. *Appl. Opt*. **39**: 456-468.

Zaneveld, J.R.V., E. Boss, and A. Barnard, 2001: Influence of surface waves on measured and modeled irradiance profiles. *Appl. Opt.*, **40:** 1442-1449.

Zibordi, G., and G.M. Ferrari, 1995: Instrument self-shading in underwater optical measurements: experimental data. *Appl. Opt.* **34:** 2750--2754.

Chapter 2

In-Water Radiometric Profile Measurements and Data Analysis Protocols.

James L. Mueller

Center for Hydro-Optics and Remote Sensing, San Diego State University, California

2.1 INTRODUCTION

Determinations of in-water spectral downwelling irradiance $E_{\mathrm{d}}(z,\lambda)$, upwelling irradiance $E_{\mathrm{u}}(z,\lambda)$ and upwelling irradiance $L_{\mathrm{u}}(z,\lambda)$, both near the surface and as vertical profiles, are required for calibration and validation of the water-leaving radiance as retrieved from the SeaWiFS and other satellite ocean color sensors. Near-surface measurements should profile through at least the top three optical depths to reliably extrapolate to $z = 0^{-}$; it is essential to obtain a profile through at least the top optical depth. To better characterize the water column for remote sensing applications, *e.g.*, primary productivity estimation, deeper vertical profiles should be made to 200 m, or seven diffuse attenuation depths whenever possible. Sea bed reflection influences on $L_{\mathrm{u}}(z,\lambda)$ and $E_{\mathrm{u}}(z,\lambda)$ should be avoided for satellite ocean color sensor validation and algorithm development by collecting data only from water deeper than six diffuse attenuation depths for $E_{\mathrm{d}}(z,490)$; remote sensing applications for optically shallow situations where bottom reflectance is present are not within the scope of these protocols.

At the present state of the art, the most reliable *in situ* method of determining water-leaving radiance $L_{\mathrm{W}}(\lambda)$ is to extrapolate an in-water profile measurement of $L_{\mathrm{u}}(z,\lambda)$ to the sea surface to estimate $L_{\mathrm{u}}(0^{-},\lambda)$. Then, $L_{\mathrm{W}}(\lambda) = t\, L_{\mathrm{u}}(0^{-},\lambda)\, n^{-2}$, where t is the upward Fresnel transmittance of the air-sea interface (~0.975) and n is the refractive index of seawater. It is also necessary to measure incident spectral irradiance $E_{\mathrm{S}}(\lambda)$ above the sea surface to determine remote sensing reflectance $R_{\mathrm{RS}}(\lambda) = L_W(\lambda)/E_{\mathrm{S}}(\lambda)$. Recent intercomparisons have demonstrated the uncertainty in $L_{\mathrm{W}}(\lambda)$ and $R_{\mathrm{RS}}(\lambda)$ determined by this approach to be < 5 % under varied cloud and sea state conditions and for Case 1 waters, at least in the sense of internal consistency of the measurements (Hooker and Maritorena 2000). To date, the best demonstrated uncertainties are >10 % in $R_{\mathrm{RS}}(\lambda)$ determined from above-water measurements of water and sky radiances and $E_{\mathrm{S}}(\lambda)$ (see Volume III, Chapter 3), due primarily to difficulty in accurately removing the contribution of skylight reflected from a wave-roughened sea surface (*e.g.* Toole *et al.* 2000).

2.2 MEASUREMENT METHODS

There are three primary sources of uncertainty in the determination of $E_{\mathrm{d}}(z,\lambda)$, $E_{\mathrm{u}}(z,\lambda)$, and $L_{\mathrm{u}}(z,\lambda)$ and their respective attenuation coefficients $K_{\mathrm{d}}(z,\lambda)$, $K_{\mathrm{u}}(z,\lambda)$, and $K_{\mathrm{L}}(z,\lambda)$: the perturbation of the in-water radiant energy field by the ship (Gordon 1985, Smith and Baker 1986, Voss *et al.* 1986, and Helliwell *et al.* 1990), shading of the measured water volume by the $E_{\mathrm{u}}(z,\lambda)$, or $L_{\mathrm{u}}(z,\lambda)$, sensor itself (Gordon and Ding 1992), and atmospherically induced variability in radiant energy incident on the sea surface during in-water measurements (Smith and Baker 1984). The influence of ship shadows on the vertical profiles of $E_{\mathrm{d}}(z,\lambda)$, $E_{\mathrm{u}}(z,\lambda)$, and $L_{\mathrm{u}}(z,\lambda)$ is dependent upon the following variables: solar zenith angle, the spectral attenuation properties of the water column, cloud cover, ship size (length, beam, draft, and freeboard) and color, and the geometry of instrument

deployment. Self-shading is dependent on solar zenith angle, the fractional contributions of direct sunlight and diffuse skylight to total incident irradiance, and the diameter of the instrument relative to the absorption scale length $a^{-1}(\lambda)$ of the water in which the measurement is made. Atmospheric variability is primarily dependent upon sun elevation and variations in cloud cover. The near surface in-water data also show variability caused by wave focusing, which can be minimized at a fixed depth by averaging over several wave periods, but which can pose severe problems in vertical profiles during which the instrument descends at speeds of 0.5—1 m s^{-1} (Zaneveld *et al.* 2001). Raman scattering and fluorescence result in second-order errors near 490 nm (CDOM fluorescence), and at longer wavelengths, contributions from phycoerythrin and fluorescence and water Raman scattering are significant. Based on recent experimental measurements of the Raman scattering cross section and its wavelength dependence (Bartlett *et al.* 1998, and references cited therein), Gordon (1999) recently determined that Raman contributions to remote sensing reflectance are 50 % to 100 % larger than had been previously estimated and are significant at all wavelengths of interest to ocean color remote sensing.

Ship Shadow Avoidance

The complete avoidance of ship shadow, or reflectance, perturbations is a mandatory requirement for all radiometric measurements to be incorporated into the SIMBIOS validation and algorithm database. The influence of ship shadow is best characterized in terms of attenuation length $K_{\mathrm{d}}^{-1}(\lambda)$ m (Gordon 1985). Because $L_{\mathrm{W}}(\lambda)$ is required with an uncertainty of 5 % or better, the protocol requires that vertical profiles be measured outside the effects of ship perturbation to the radiant energy field. To accomplish this, the instrument must be deployed from the stern, with the sun's relative bearing aft of the beam. Yet a better approach is to deploy a free falling, profiling radiometer well away from the ship on an umbilical tether.

Estimates of the minimum distance away from the ship, under conditions of clear sunny skies, are given below. The distances are expressed in attenuation lengths to minimize error. For $E_{\mathrm{d}}(z,\lambda)$ measurements, the general equation for distance away, ξ in meters, is given as

$$\xi = \frac{\sin(48.4°)}{K_{\mathrm{d}}(\lambda)}. \tag{2.1}$$

The distance from the ship is required to be $3K_{\mathrm{u}}^{-1}(\lambda)$ m for $E_{\mathrm{u}}(z,\lambda)$ and $1.5K_{\mathrm{L}}^{-1}(\lambda)$ m for $L_{\mathrm{u}}(z,\lambda)$ measurements. These distances should be increased if the instrument is deployed off the beam of a large vessel. A variety of methods have been used to deploy optical instruments beyond the influence of the ship. During CZCS algorithm development, floating plastic frames were equipped with small winches and instruments to obtain near surface optical profiles at some distance away from the ship. An umbilical cable provided power and data transfer. These platforms, while being somewhat difficult to deploy, worked well at avoiding ship shadow. Alternatively, extended booms can be used to deploy the instrument away from the ship and have the advantages of allowing relatively rapid deployment and simultaneous rosette bottle sampling. As a point of caution, however, very long booms may accentuate unwanted vertical motions due to ship pitch and roll.

Waters *et al.* (1990) used an optical free-fall instrument (OFFI) that allows optical data to be obtained outside the influence of ship perturbation. In addition, the OFFI approach allows optical data to be obtained independently from violent ship motion, which may be transmitted to the instrument via the hydro wire, especially on a long boom. Over the past few years, OFFI-like radiometer systems have become commercially available from several manufacturers and have found widespread use in the ocean color community. In comparisons between several deployment configurations (Hooker and Maritorena 2000), free-fall radiometer systems, in combination with shipboard surface irradiance sensors, yielded water-leaving radiances with the lowest uncertainties. Yet another method for the deployment of optical sensors is via an ROV. Some groups, *e.g.*, Smith (pers. comm.), have deployed a spectrometer on an ROV and obtained data completely free of ship influences.

The above criteria for ship shadow avoidance are admittedly very conservative. Unfortunately, the above cited models and observations provide only approximate guidance on minimum distances at which ship reflectance and shadow effects become insignificant under all circumstances. Therefore, the SIMBIOS ocean optics protocols embrace relatively extreme distance criteria, recognizing that in many specific combinations of lighting conditions, ships and optical properties, ship shadow, and reflection effects may become unimportant much closer to the ship. The essential requirement is that each investigator establishes that any measurements of $E_{\mathrm{d}}(z,\lambda)$, $E_{\mathrm{u}}(z,\lambda)$, and

$L_u(z,\lambda)$ submitted for SIMBIOS validation and algorithm development are free from ship-induced errors. The simplest way to do this is to adhere to the above distance criterion, which is not difficult when using either a tethered free-fall system or instruments mounted on an ROV. In other cases, it is incumbent on the investigator to otherwise demonstrate the absence of ship effects, *e.g.*, through analysis of a series of profiles at increasing distance.

Depth Resolution in Profiles

The instrument sampling rate and the speed at which the instrument is lowered or raised through the water column should yield at least two, and preferably six to eight, samples per meter.

Instrument Dark Readings

The dark current of optical sensors is frequently temperature dependent. As a consequence, accurate radiometric measurements require that careful attention be given to dark current variability. It is recommended that each optical measurement be accompanied by a measurement of the instrument dark current. When there is a large temperature difference between the instrument on the deck and the water temperature, the instrument should be allowed to equilibrate with ambient water temperature at the beginning of each cast.

Deep casts, *e.g.*, 500 m, may permit the determination of the dark current in each optical channel at the bottom of each cast. Many instruments are not designed to be lowered safely to 500 m, however, and this approach is usually not feasible. Furthermore, there is some intrinsic uncertainty over possible contamination by bioluminescence when dark readings are obtained in this way. If the instrument is equipped with a shutter, dark currents can be measured at any depth in the cast. If the dark current is not determined during the cast, it should be determined as soon as possible after the instrument is returned to the deck.

Temperature effects on sensor responsivity can be significant and should not be ignored. Therefore, sensors should be equipped with thermistors on detector mounting surfaces to monitor temperatures for data correction. Otherwise, deck storage should be under thermally protected conditions prior to deployment and on-deck determination of dark voltages.

Surface Incident Irradiance

Atmospheric variability, especially under cloud cover, leads directly to variability of the in-water light field and must be corrected to obtain accurate estimations of optical properties from irradiance or radiance profiles. First order corrections for this variability can be made using above water (on deck) measurements of downwelling spectral irradiance, $E_S(\lambda) = E_d(0^+,\lambda)$. Smith and Baker (1984) and Baker and Smith (1990) theoretically computed the irradiance just below the air-water interface, $E_d(0^-,\lambda)$, from deck measurements to correct in-water profile data.

The deck sensor must be properly gimbaled to avoid large errors in $E_S(\lambda)$ due to ship motion in a seaway. Improper gimballing can actually accentuate sensor motion under some circumstances, however, and this aspect of a shipboard radiometer system must be engineered with some care.

In early versions of the ocean optics protocols (Mueller and Austin 1992, 1995), it was suggested that an improved, more direct determination of $E_d(0^-,\lambda)$ might be obtained by deploying a floating instrument to obtain continuous downwelling irradiance data just below the air-water interface (Waters *et al.* 1990). Over the past several years, instruments implementing this concept have become commercially available and the ocean color community has used them extensively. Unfortunately, experience has demonstrated that downwelling irradiance fluctuations associated with focusing and defocusing of sunlight by surface waves (Zaneveld *et al*. 2001) renders such measurements far noisier than measurements of $E_S(\lambda)$ made above the sea surface. A variant on this approach, wherein the sensor is floated away from the ship but is elevated a meter or so above the water surface, has proved to be a viable alternative, especially in circumstances when it is impossible to install and/or gimbal a deck cell properly.

Instrument Attitude

An instrument's attitude with respect to the vertical is a critical factor in measurements of $E_{\mathrm{d}}(z,\lambda)$ and $E_{\mathrm{u}}(z,\lambda)$, and is only slightly less critical for $L_{\mathrm{u}}(z,\lambda)$. Roll and pitch sensors must, therefore, be installed in the underwater radiometers used for acquiring SIMBIOS validation data. The data from these attitude sensors are to be recorded concurrently with the data from the radiometric channels and are to be used as a data quality indicator. It is not deemed necessary to determine or control attitude determination errors resulting from surface wave-induced accelerations at very shallow depths.

2.3 ANCILLARY MEASUREMENTS AND LOGS

The following ancillary data and information must be recorded in header files and/or logs for each radiometric profile cast:

1. date and time (UTC) of the station and cast;
2. geographic location (latitude and longitude in decimal degrees to the nearest 0.001);
3. the distance between the profiling sensor and the ship, and its direction relative to the ship's heading;
4. the direction of the sun relative to the ship's heading;
5. Secchi depth;
6. cloud cover and sky conditions;
7. wind speed and direction;
8. barometric pressure;
9. dark (zero-offset) data file, to be recorded at the time of the cast and the dark filename logged with the profile entry;
10. times, locations and file identification of associated CTD, *in situ* fluorescence, and inherent optical property profiles, if any;
11. depths and times of associated water samples, if any;
12. names of files with data from comparisons with a portable irradiance and radiance reference standard made in the field and used to track the instrument's stability during a deployment (Chapter 7);
13. instrument identification;
14. calibration date and file identification (constant throughout a cruise, usually); and
15. depth offsets (to nearest cm) between the pressure transducer and all sensor probes, including $L_{\mathrm{u}}(z,\lambda)$ window, $E_{\mathrm{d}}(z,\lambda)$ and $E_{\mathrm{u}}(z,\lambda)$ collectors, and all ancillary probes on a package.

2.4 DATA ANALYSIS METHODS

This section provides descriptions and discussion of the methods and procedures required to process profile measurements of $E_{\mathrm{d}}(z,\lambda)$, $E_{\mathrm{u}}(z,\lambda)$, and $L_{\mathrm{u}}(z,\lambda)$ from raw counts to radiometric units to derive attenuation coefficient profiles $K_{\mathrm{d}}(z,\lambda)$, $K_{\mathrm{u}}(z,\lambda)$, and $K_{\mathrm{L}}(z,\lambda)$, and for extrapolating the data to the sea surface to determine $E_{\mathrm{d}}(0^{-},\lambda)$, $E_{\mathrm{u}}(0^{-},\lambda)$, and $L_{\mathrm{u}}(0^{-},\lambda)$. Water-leaving radiance is then determined as

$$L_{\mathrm{w}}(\lambda) = \frac{1-\rho}{n^2} L_{\mathrm{u}}(0^{-},\lambda), \tag{2.2}$$

where $\rho \cong 0.025$ is the Fresnel reflectance of the air sea interface, and $n \cong 1.34$ is the refractive index of seawater. The term $\frac{1-\rho}{n^2} \cong 0.543$ is the upward radiance transmittance of the sea surface for normal incidence from below, and is not sensitive to wind speed (Austin 1974; see also Volume III, Chapter 4).

Remote sensing reflectance is calculated as

$$R_{\mathrm{RS}}(\lambda) = \frac{L_{\mathrm{W}}(\lambda)}{E_{\mathrm{S}}(\lambda)}, \tag{2.3}$$

where $E_{\mathrm{S}}(\lambda)$ is downwelling incident irradiance measured above the sea surface, and is equivalent to $E_{\mathrm{d}}(0^+,\lambda)$. It is not recommended to estimate $E_{\mathrm{d}}(0^+,\lambda)$ from in-water determinations of $E_{\mathrm{d}}(0^-,\lambda)$, because wave-focusing effects yield uncertainties approaching 10 % under even ideal circumstances (Siegel *et al.* 1995; Zaneveld *et al.* 2001). The lack of directional notation in (2.2) and (2.3) signifies that the quantities represent nadir viewing values of $L_{\mathrm{W}}(\lambda)$ and $R_{\mathrm{RS}}(\lambda)$. Directional (off-nadir at a given azimuth angle from the sun) above-water measurements of surface radiance and remote-sensing reflectance are discussed in Volume III, Chapters 3 and 4.

***Normalized water-leaving radiance*,** as defined by Gordon and Clark (1981) may be calculated from $L_{\mathrm{W}}(\lambda)$ and $E_{\mathrm{S}}(\lambda)$ as

$$L_{\mathrm{WN}}(\lambda) = \frac{L_{\mathrm{W}}(\lambda)}{E_{\mathrm{S}}(\lambda)} \bar{F}_{\mathrm{o}}(\lambda), \tag{2.4}$$

where $\bar{F}_{\mathrm{o}}(\lambda)$ is the mean solar flux immediately above the earth's atmosphere (Neckel and Labs 1984). The intended effect of (2.4) is to scale each measured $L_{\mathrm{W}}(\lambda)$ to a value consistent with surface illumination by the sun at zenith with no atmosphere, and at the mean earth-sun distance (see also the discussion in Volume III, Chapter 4). If $E_{\mathrm{S}}(\lambda)$ measurements of acceptable uncertainty are not available, the ratio $\frac{\bar{F}_{\mathrm{o}}(\lambda)}{E_S(\lambda)}$ may be calculated as in Volume III, Chapter 4 [equation (4.18)] and Volume VI, Chapter 2. The Gordon and Clark (1981) normalization embodied in (2.4) takes account only of the *intensity* of surface illumination, and neglects the dependence of $L_{\mathrm{u}}(0^-,\lambda)$ on solar zenith angle θ_{o} and the bidirectional nature of the ocean's reflectance (Morel and Gentili 1996; Volume III, Chapter 4 and other references cited therein). A further transformation to remove the bidirectional effect and determine a quantity called ***exact normalized water-leaving radiance***, $L_{\mathrm{WN}}^{\mathrm{ex}}(\lambda)$, is necessary to compare $L_{\mathrm{WN}}(\lambda)$ based on nadir-viewing field measurements with each other (for differing θ_{o} and inherent optical properties), or with $L_{\mathrm{WN}}(\lambda)$ derived from radiances measured above water from a satellite, aircraft, or ship (Volume III, Chapter 4).

Dark Corrections

The instrument's dark responses in each channel, which should recorded either during or immediately after each profile, must be subtracted from the raw data prior to further processing.

Instrument Calibration Analysis

Instrument data from pre- and post-deployment calibrations should be compared with: (1) each other; (2) the long-term history of an instrument's calibrations; and (3) the record of comparisons with a portable field irradiance and radiance standard, to be made frequently during a cruise (Volume II, Chapter 5).

Based on this analysis of the instrument's history, a calibration file will be generated and applied to transform the dark-corrected data from raw counts to radiance and irradiance units. This analysis, and the rationale for adopting a particular set of calibration coefficients, both for responsivity and wavelength, should be fully described

in the documentation accompanying the data set, preferably in an ASCII file to be retained on line with each data set.

Depth Offset Adjustments

The distance of each irradiance collector and radiance window above, or below, the instrument's pressure transducer port must be subtracted, or added, to the nominal recorded depth so that $E_{\mathrm{d}}(z,\lambda)$, $E_{\mathrm{u}}(z,\lambda)$, and $L_{\mathrm{u}}(z,\lambda)$ are associated with the depths where they were actually measured. These depth adjustments may be applied either before, or during, attenuation profile analysis, but in either case must be applied before extrapolating values to the sea surface.

Profile Normalization by Surface Irradiance

The dominant uncertainties in measured K(z,λ) profiles result from changes in cloud cover during a cast. Cloud cover variability causes strong variations in incident surface irradiance, $E_{\mathrm{S}}[t(z),\lambda]$ measured at time *t*(*z*), over the duration of a radiometric cast. In present usage, $E_{\mathrm{S}}[t(z),\lambda]$ refers to incident spectral irradiance measured with a deck cell aboard a ship. It is strongly recommended that all incident irradiance measurements be made above the sea surface. Smith and Baker (1984 and 1986) discuss a method for propagating $E_{\mathrm{S}}(\lambda)$ through the sea surface to estimate $E_{\mathrm{d}}(0^{-},\lambda)$, and they also present a model for adjusting $E_{\mathrm{d}}(0^{-},\lambda)$ to compensate for solar zenith angle (see also Volume III, Chapter 4, Sections 4.1 and 4.2). An alternative scheme for estimating $E_{\mathrm{d}}(0^{-},\lambda)$ by measuring $E_{\mathrm{d}}(z,\lambda)$ with a radiometer floated away from the ship and held at a shallow depth z_{r} during a cast (Waters *et al.* 1990) was tentatively recommended in Mueller and Austin (1995). However, subsequent community experience has demonstrated in-water estimates of $E_{\mathrm{d}}(0^{-},\lambda)$ to be far noisier than those based on measurements of $E_{\mathrm{S}}[t(z),\lambda]$ made above the sea surface (Siegel *et al.* 1995; Hooker and Maritorena 2000; Zaneveld *et al.* 2001).

The record of $E_{\mathrm{S}}[t(z),\lambda]$ is recorded simultaneously and together with profiles of $E_{\mathrm{d}}(z,\lambda)$, $E_{\mathrm{u}}(z,\lambda)$, and $L_{\mathrm{u}}(z,\lambda)$. Assuming that transmission of $E_{\mathrm{S}}[t(z),\lambda]$ through the surface does not vary with time, then a simple and effective normalization of the profiles is obtained as

$$\hat{E}_{\mathrm{d}}(z,\lambda)=\frac{E_{\mathrm{d}}(z,\lambda)E_{\mathrm{S}}[t(0^{-}),\lambda]}{E_{\mathrm{S}}[t(z),\lambda]}, \tag{2.5}$$

where $E_{\mathrm{S}}[t(z),\lambda]$ is the deck cell irradiance measured at the time t(z) when the radiometer was at depth z and $E_{\mathrm{S}}[t(z),\lambda]$ is the measurement at time $t(0^{-})$ when the radiometer was at the surface.

Some investigators have used $E_{\mathrm{S}}[t(z),\lambda]$ at a single reference wavelength, *e.g.*, 550 nm, to normalize profiles, and have thus ignored the usually small spectral variations in incident irradiance. For SIMBIOS validation and algorithm development, however, the recommended protocol is to use multispectral $E_{\mathrm{S}}[t(z),\lambda]$ measurements. Under no circumstances should a PAR, or other broadband (*e.g.*, photopic response), sensor ever be used for this purpose.

Because of spatial separation between the surface and underwater radiometers, cloud shadow variations are neither measured identically, nor in phase, by the two instruments. The $E_{\mathrm{S}}[t(z),\lambda]$ profiles should, therefore, be smoothed to remove high frequency fluctuations while retaining variations with periods of 15 seconds or greater.

The smoothed $\frac{E_S\left[t\left(0^-\right),\lambda\right]}{E_S\left[t\left(z\right),\lambda\right]}$ profiles should then be used in (2.5) to adjust the measured irradiance and radiance profiles to correct for variations in incident irradiance during a cast.

Some investigators (*e.g.* Sorensen *et al.* 1995), who are faced with the need to process hundreds of radiometric profiles, have implemented automated, semi-autonomous processing and analysis systems which do not include a profile normalization like that embodied in (2.5). In this approach, radiometric profiles are simply rejected and not analyzed if overall variability in $E_S\left[t\left(z\right),\lambda\right]$ exceeds a minimum acceptance threshold. For all accepted profiles, it is implicitly assumed that $\frac{E_S\left[t\left(0^-\right),\lambda\right]}{E_S\left[t\left(z\right),\lambda\right]} \equiv 1.0$ and is constant throughout the measurement. The only drawback to this method of data screening is that many otherwise usable profiles are not analyzed.

K-Analysis

Normalized profiles of $E_d\left(z,\lambda\right)$, $E_u\left(z,\lambda\right)$, and $L_u\left(z,\lambda\right)$ (with z corrected for pressure transducer depth offset relative to each sensor) should be fit to the equations

$$E_d\left(z,\lambda\right) = E_d\left(0^-,\lambda\right)e^{-\int_o^z K_d\left(z',\lambda\right)dz'}, \tag{2.6}$$

$$E_u\left(z,\lambda\right) = E_u\left(0^-,\lambda\right)e^{-\int_o^z K_u\left(z',\lambda\right)dz'}, \tag{2.7}$$

and

$$L_u\left(z,\lambda\right) = L_u\left(0^-,\lambda\right)e^{-\int_o^z K_L\left(z',\lambda\right)dz'}, \tag{2.8}$$

respectively. The vertical profiles of attenuation coefficients $K_d\left(z,\lambda\right)$, $K_u\left(z,\lambda\right)$, and $K_L\left(z,\lambda\right)$, together with the respective values of $E_d\left(0^-,\lambda\right)$, $E_u\left(0^-,\lambda\right)$, and $L_u\left(z,\lambda\right)$ at the surface, provide the needed specifications for the smoothed irradiance and radiance profiles.

If the natural logarithm of (2.6), (2.7), or (2.8) is taken, an equation of the following form is obtained:

$$-\int_0^z K\left(z'\right)dz' = \ln\left[E\left(z\right)\right] - \ln\left[E\left(0^-\right)\right], \tag{2.9}$$

so that

$$K\left(z\right) = -\left.\frac{d\ln\left[E\left(z\right)\right]}{dz}\right|_z. \tag{2.10}$$

The traditional method of K-analysis, *e.g.*, Smith and Baker (1984 and 1986), is to estimate K(z) as the local slope of $\ln\left[\hat{E}\left(z\right)\right]$ measured within a depth interval spanning a few meters, and centered at depth z_m. It is assumed that $K(z)$ is constant over the depth interval centered at z_m, so that

$$\ln\left[E\left(z\right)\right] \cong \ln\left[\hat{E}\left(z_m\right)\right] - \left(z - z_m\right)K\left(z_m\right). \tag{2.11}$$

The unknowns $\ln\left[\tilde{E}\left(z_m\right)\right]$ and $K(z_m)$ are determined as the intercept and (negative) slope of a least-squares regression fit to measured $\ln\left[\hat{E}\left(z_m\right)\right]$ data within the depth interval $\left(z_m - \Delta z\right) \le z < \left(z_m + \Delta z\right)$. The half-interval Δz is somewhat arbitrary. Smith and Baker (1984 and 1986) suggest a Δz of approximately 4 m, but for noisy profiles, a Δz as large as 10 m may be needed to smooth over incident irradiance fluctuations left as residuals by the deck cell normalization.

When this method is used, the shallowest possible values in the smoothed $\ln\left[\tilde{E}\left(z_{\mathrm{m}}\right)\right]$ and $K(z_{\mathrm{m}})$ profiles are at depth Δz m and the deepest values are Δz m above the deepest measurements in the profile. If obvious ship shadow effects are present in the data, the shallowest valid smoothed data point will be at depth ($z_{\mathrm{s}} + \Delta z$) where z_{s} is the depth to which the data are regarded as contaminated and are excluded from the analysis. It is often convenient, although not necessary, to pre-average radiometric data into, *e.g.*, 1 m, bins prior to performing the least-squares analysis. If this is done, the data should be pre-filtered to remove any noise spikes and then averaged before it is log-transformed.

Each step in the analysis yields increasingly refined information, which requires various amounts of intervention from the analyst. After appropriate editing to remove artifacts, such as the effects of ship shadow, vertical profiles of $K(z,\lambda)$ are computed from the logarithmic decrement with depth of the radiometric profiles. Direct derivative method calculations of $K(z,\lambda)$ profiles using computer techniques (see above) may require the use of a depth interval as large as 20 m, with the result that information about the slope, and hence, about $K(z,\lambda)$ near the top and bottom of the profile, is lost. Averaging over such a large interval also causes the slopes in sharply defined layers, *e.g.*, regions of high gradients, to be poorly represented. Attempts to reduce these effects by using a significantly smaller depth interval often results in unacceptably noisy $K(z,\lambda)$ profiles.

An alternative method of determining K-profiles (Mueller 1995) is to keep (2.9) in integral form, expressed in terms of diffuse attenuation depth (optical depth) $\tau(z,\lambda)$ as

$$\tau(z,\lambda) = -\int_0^z K(z',\lambda)dz' = \ln\left[\frac{E(0^-)}{E(z)}\right]. \tag{2.12}$$

The K-profile is represented analytically by Hermitian cubic polynomials with unknown coefficients, consisting of $K(z_n)$ and its derivative $dK(z_n)/dz$, at each of several discrete depths dividing the profile into finite depth elements. [Hermitian cubic polynomials are defined in any text on finite element modeling, *e.g.*, Pinder and Gray (1977).] The measured set of equations (2.12), corresponding to each measured value $E(z)$ in the profile and depth z in the profile, are assembled into matrix form and the unknown set of coefficients $K(z_n)$ and $dK(z_n)/dz$ are determined using classical least-squares minimization. $E(0^-)$ must be specified externally, and in the current implementation is estimated from the profile itself and adjusted iteratively to yield a minimum least-squares solution to the overall profile. The complete formulation of the method is given in Mueller (1995). Compared to results of the derivative solution, the integral method yields significantly more detailed representation of very sharp layers in bio-optical profiles (when compared to concurrent beam attenuation and chlorophyll fluorescence profiles). The integral solution is more robust in handling data gaps, *e.g.* due to extreme cloud shadows which are not corrected by deck-cell normalization. The integral solution automatically extrapolates the profile to $E(0^-)$ based on a best fit to the entire profile, and not simply to the noisy near-surface layer. On the other hand, the integral method of solution is considerably more difficult to implement than the derivative approach. Moreover, the approach requires an interactive analysis of each profile, and is more time consuming than an automated analysis using the derivative method. For these reasons, the integral solution is not widely used within the ocean color community.

Extrapolation to the Sea Surface

Because of surface waves, it is rarely possible to measure $E_{\mathrm{d}}(z,\lambda)$, $E_{\mathrm{u}}(z,\lambda)$, and $L_{\mathrm{u}}(z,\lambda)$ at depths that closely approximate $z \cong 0^-$. The shallowest reliable readings typically occur at depths ranging from 0.5—2 m. The data from this zone usually exhibit strong fluctuations associated with surface waves, and thus require some form of smoothing or averaging. It is almost always necessary to apply some means of extrapolating the data upward to the sea surface. Whatever method is used should reconcile extrapolated $E_{\mathrm{d}}(0^-,\lambda)$ with deck measurements of $E_{\mathrm{S}}(\lambda)$, with an approximate adjustment for the contribution of reflected $E_{\mathrm{u}}(0^-,\lambda)$ to $E_{\mathrm{d}}(0^-,\lambda)$ [see also Volume I, Chapter 2, Section 2.7 and Volume III, Chapter 4, equation (4.11)].

If K(z) profiles are determined using the derivative method, the shallowest smoothed estimates will occur at depth $z_{\mathrm{o}} = \Delta z$, if there are no ship shadow effects. The usual procedure is to extrapolate values to $z = 0^-$ as

$$E_{\mathrm{d}}\left(0^{-},\lambda\right)=E_{\mathrm{d}}\left(z_{\mathrm{o}},\lambda\right)e^{K_{\mathrm{d}}\left(z_{\mathrm{o}},\lambda\right)z_{\mathrm{o}}}, \tag{2.13}$$

$$E_{\mathrm{u}}\left(0^{-},\lambda\right)=E_{\mathrm{u}}\left(z_{\mathrm{o}},\lambda\right)e^{K_{\mathrm{u}}\left(z_{\mathrm{o}},\lambda\right)z_{\mathrm{o}}}, \tag{2.14}$$

and

$$L_{\mathrm{u}}\left(0^{-},\lambda\right)=L_{\mathrm{u}}\left(z_{\mathrm{o}},\lambda\right)e^{K_{\mathrm{L}}\left(z_{\mathrm{o}},\lambda\right)z_{\mathrm{o}}}. \tag{2.15}$$

If ship shadow is present, z_o may be 20 m or more, and the extrapolation becomes somewhat tenuous.

If K(z) profiles are determined by means of the integral method, then $E_{\mathrm{d}}\left(0^{-},\lambda\right)$, $E_{\mathrm{u}}\left(0^{-},\lambda\right)$, and $L_{\mathrm{u}}\left(0^{-},\lambda\right)$ are automatically determined as part of the fitting procedure. The surface values thus obtained are not necessarily superior to those obtained by extrapolating the derivative method solutions, but they do have the advantage of representing an internally consistent least-squares fit to the entire profile beneath the surface boundary layer.

By either method, extrapolating measured $E_{\mathrm{d}}\left(z,\lambda\right)$, $E_{\mathrm{u}}\left(z,\lambda\right)$, and $L_{\mathrm{u}}\left(z,\lambda\right)$ to $z=0^{-}$ becomes very difficult at $\lambda \geq 650$ nm. At these wavelengths, the rapid decrease in daylight over an extremely shallow first attenuation length may compete with an increase in flux with depth due to inelastic scattering. Indeed, it is not unusual to find negative values of $K_{\mathrm{d}}\left(z,\lambda\right)$ and $K_{\mathrm{L}}\left(z,\lambda\right)$ in strong chlorophyll maxima. Additional research is needed to address measurement and estimation of $E_{\mathrm{d}}\left(0^{-},\lambda\right)$, $E_{\mathrm{u}}\left(0^{-},\lambda\right)$, and $L_{\mathrm{u}}\left(0^{-},\lambda\right)$ at these wavelengths, especially in chlorophyll-rich Case 2 waters.

Instrument Self-Shading

Gordon and Ding (1992) modeled the errors introduced by an instrument's own shadow in direct measurements used to determine $E_{\mathrm{u}}\left(0^{-},\lambda\right)$ and $L_{\mathrm{u}}\left(0^{-},\lambda\right)$. For this source of error to be less than 5 %, without modeled corrections, the instrument radius *r* must satisfy $r \leq \left[30a\left(\lambda\right)\right]^{-1}$ for $E_{\mathrm{u}}\left(0^{-},\lambda\right)$ and $r \leq \left[100a\left(\lambda\right)\right]^{-1}$ for $L_{\mathrm{u}}\left(0^{-},\lambda\right)$. They calculate for $\lambda = 865$ nm in pure water, as an example, that the instrument radius must be approximately 0.3 cm to measure $E_{\mathrm{u}}\left(0^{-},\lambda\right)$ with a maximum of 5 % error; the instrument radius must be significantly smaller for direct measurement error in $L_{\mathrm{u}}\left(0^{-},\lambda\right)$ to be 5 % or less.

Gordon and Ding (1992) also propose a simple model for correcting $E_{\mathrm{u}}\left(0^{-},\lambda\right)$ and $L_{\mathrm{u}}\left(0^{-},\lambda\right)$ for the self-shadowing effect. They write

$$\tilde{L}_{\mathrm{u}}\left(0^{-},\lambda\right)=\frac{\hat{L}_{\mathrm{u}}\left(0^{-},\lambda\right)}{1-\varepsilon\left(\lambda\right)}, \tag{2.16}$$

and

$$\varepsilon\left(\lambda\right)=1-e^{-\kappa' a\left(\lambda\right)r}, \tag{2.17}$$

where $\tilde{L}_{\mathrm{u}}\left(0^{-},\lambda\right)$ is the true value, $\hat{L}_{\mathrm{u}}\left(0^{-},\lambda\right)$ is the measured value, $\kappa'=\dfrac{y}{\tan\theta'_{\mathrm{o}}}$ (θ'_{o} is the refracted solar zenith angle) and *y* is an empirical factor for which they give values determined by fitting their model results $\left(y \approx 2\right)$. A similar correction, with a different table of values for *y* applies to $E_{\mathrm{u}}\left(0^{-},\lambda\right)$.

When the above geometric corrections are applied, Gordon and Ding (1992) estimate that errors less than or equal to 5 % in $L_{\mathrm{u}}\left(0^{-},\lambda\right)$ could be determined from measurements with instruments having maximum diameters of 24 cm for $\lambda \leq 650$ nm, and with instruments of maximum diameter 10 cm for $650\text{ nm} < \lambda \leq 700\text{ nm}$ at solar zenith angles $\theta_{\mathrm{o}} \geq 20°$, and maximum chlorophyll *a* concentrations of 10 mg m^{-3}. To measure $L_{\mathrm{u}}\left(0^{-},\lambda\right)$ correctable to less than 5 % error at $\theta_{\mathrm{o}} = 10°$ (with chlorophyll *a* concentrations ≤ 10 mg m^{-3}), maximum instrument diameters are

12 cm for $\lambda \le 650$ nm and 5 cm for $650 \text{ nm} < \lambda \le 700$ nm. Even with these corrections, however, instrument diameters of 1 cm or less must be used to assure self-shading $L_u(0^-,\lambda)$ errors are 5 % or less at 780 nm and 875 nm.

The Gordon and Ding (1992) model predictions were compared to experimental measurements of $L_u(0^-,\lambda)$ just beneath the sea surface, using a fiber-optic radiometric probe (Zibordi and Ferrari 1995). The experiment was performed in a lake, with solar zenith angles $25° \le \theta_o \le 55°$, on several days with cloud-free skies. Spectrophotometric methods (similar to those in Volume IV, Chapter 4) were used to measure absorption by particles and Gelbstoff. At wavelengths of 500 nm, 600 nm, and 640 nm, a series of discs was employed to vary instrument self-shading geometry in several steps over the range $0.001 < a(\lambda)r \le 0.1$. The Gordon and Ding (1992) model predicted self-shading radiance and irradiance effects that may be applied as corrections, and which agreed with measured values within 5 % and 3 %, respectively. The model corrections were all biased high relative to the measured values. Zibordi and Ferrari (1995) chose to compare their measurements to the Gordon and Ding (1992) *point-sensor* model, and use of their *finite-sensor* model results may have further improved the comparisons.

This initial confirmation of the Gordon and Ding (1992) instrument self-shading model is confined to clear-sky conditions, solar zenith angles greater than 25°, near-surface $L_u(0^-,\lambda)$ and $E_u(0^-,\lambda)$, and $a(\lambda)r \le 0.1$. Additional theoretical and experimental research will be necessary to generalize this correction for cloudy sky conditions and for variations with depth in $L_u(z,\lambda)$ and $E_u(z,\lambda)$ profiles. The above restrictions notwithstanding, the excellent agreement shown so far covers a very important range of conditions for SeaWiFS and SIMBIOS algorithm development and validation.

A provisional protocol is given here for radiometer self-shading corrections to $L_u(0^-,\lambda)$ and $E_u(0^-,\lambda)$ derived from in-water radiometric measurements. The protocol is based on the model of Gordon and Ding (1992) and the limited experimental confirmation by Zibordi and Ferrari (1995). Although additional research is necessary to extend and verify these correction algorithms, the results published to date show clearly that even a provisional correction will significantly improve $L_u(0^-,\lambda)$ and $E_u(0^-,\lambda)$ estimated from underwater measurements.

It is first necessary to measure or estimate the spectral absorption coefficient a(λ), preferably using *in situ* instruments (Volume IV, Chapter 3), or if necessary, using the laboratory methods of Volume IV, Chapter 4. It is also possible to estimate a(λ) using other approximations suggested by Gordon and Ding (1992), based either on measurements of phytoplankton pigment concentrations, or of irradiance attenuation coefficients.

It will also be necessary to measure, or estimate, the direct solar, $E_{sun}(\lambda)$ and skylight, $E_{sky}(\lambda)$ components of incident spectral irradiance, $E_S(\lambda)$, where $E_S(\lambda) = E_{sun}(\lambda) + E_{sky}(\lambda)$. The preferred method is to measure these components following the protocols of Volume III, Chapter 5. Zibordi and Ferrari (1995) also describe a method of estimating the ratio $\frac{E_{sky}(\lambda)}{E_{sun}(\lambda)}$, and Gordon and Ding (1992) suggest yet other alternatives.

Following Zibordi and Ferrari (1995), the coefficients, κ', given in Table 2 of Gordon and Ding (1992), are fit to linear regression models as functions of the solar zenith angle θ_o in the range $30° \le \theta_o \le 70°$. The results given for $L_u(0^-,\lambda)$, with sun only, for a point sensor may be computed as

$$\kappa'_{sun,o} \tan\theta'_o = 2.07 + 5.6\times10^{-3}\theta_o, \tag{2.18}$$

and for a finite sensor occupying the full diameter of the instrument,

$$\kappa'_{sun,l} \tan\theta'_o = 1.59 + 6.3\times10^{-3}\theta_o, \tag{2.19}$$

where θ_o and θ'_o are the solar zenith angles [in degrees] in air and water, respectively. In practice, the diameter of the radiance sensor aperture is usually a small fraction of the instrument diameter. In the results reported by Zibordi and Ferrari (1995), the point sensor model always overestimated ε, and use of the finite sensor model (2.19) will

always yield a lower estimate of ε. Pending new insights from future theoretical and experimental work, it is suggested to estimate

$$\kappa'_{\text{sun}} \tan\theta'_{\text{o}} = (1-g)\kappa'_{\text{sun,o}} \tan\theta_o + g\kappa'_{\text{sun,l}} \tan\theta_o, \tag{2.20}$$

where g is the ratio of sensor[1]-to-instrument diameters. The coefficient, κ'_{sky} for the self-shading effect on $L_{\text{u}}\left(0^-,\lambda\right)$ caused by incident diffuse skylight is similarly estimated as

$$\kappa'_{\text{sky}} = 4.61 - 0.87g, \tag{2.21}$$

where the coefficients are derived from values given in Table 3 of Gordon and Ding (1992). Self-shading errors $\varepsilon_{\text{sun}}(\lambda)$ and $\varepsilon_{\text{sky}}(\lambda)$ for $E_{\text{sun}}\left(\lambda\right)$ and $E_{\text{sky}}\left(\lambda\right)$ components, respectively, are then computed as

$$\varepsilon_{\text{sun}}\left(\lambda\right) = 1 - e^{-\kappa'_{\text{sun}} a(\lambda) r}, \tag{2.22}$$

and

$$\varepsilon_{\text{sky}}\left(\lambda\right) = 1 - e^{-\kappa'_{\text{sky}} a(\lambda) r}, \tag{2.23}$$

where r is the instrument radius in m, and the absorption coefficient a(λ) is in units of m^{-1}.

The self-shading error in $L_{\text{u}}\left(0^-,\lambda\right)$ is then calculated as

$$\varepsilon\left(\lambda\right) = \frac{\varepsilon_{\text{sun}}\left(\lambda\right) + \varepsilon_{\text{sky}}\left(\lambda\right)}{1+h}, \tag{2.24}$$

where

$$h = \frac{E_{\text{sky}}\left(\lambda\right)}{E_{\text{sun}}\left(\lambda\right)}. \tag{2.25}$$

Finally, the corrected radiance $\tilde{L}_{\text{u}}\left(0^-,\lambda\right)$ is estimated with Equation (2.16).

Similarly, for $E_{\text{u}}\left(0^-,\lambda\right)$, the values given in Tables 2 and 3 of Gordon and Ding (1992) determine that for a point irradiance sensor,

$$\kappa'_{\text{sun,o}} = 3.41 - 1.55\times10^{-2}\theta_{\text{o}}. \tag{2.26}$$

For an irradiance collector with a diameter equal to that of the instrument,

$$\kappa'_{\text{sun,l}} = 2.76 - 1.21\times10^{-2}\theta_{\text{o}}, \tag{2.27}$$

so that

$$\kappa'_{\text{sun}} = (1-g)\kappa'_{\text{sun,o}} + g\kappa'_{\text{sun,l}}, \tag{2.28}$$

where g is the ratio of the diameter of the irradiance collector to that of the instrument. For the sky component, κ'_{sky} is defined as

$$\kappa'_{\text{sky}} = 2.70 - 0.48g. \tag{2.29}$$

Values of κ'_{sun} and κ'_{sky} from (2.28) and (2.29) are then substituted in equations (2.21) and (2.22) to obtain $\varepsilon_{\text{sun}}(\lambda)$ and $\varepsilon_{\text{sky}}(\lambda)$ that are then used in (2.23) to solve for ε(λ). Finally, corrected upwelled spectral irradiance $\tilde{E}_{\text{u}}\left(0^-,\lambda\right)$ is estimated as

[1] For a radiance sensor, the appropriate "sensor" diameter is that of the circular area subtended by the sensor's FOV at the base of the instrument, *i.e.* $2x\tan\left(\frac{\theta_{\text{FOV}}}{2}\right)$, where x is the distance between the detector aperture and plane of the instrument's base, and θ_{FOV} is the instrument's FWHM FOV.

$$\tilde{E}_{\mathrm{u}}\left(0^{-},\lambda\right)=\frac{\hat{E}_{\mathrm{u}}\left(0^{-},\lambda\right)}{1-\varepsilon\left(\lambda\right)}, \tag{2.30}$$

where $\hat{E}_{\mathrm{u}}\left(0^{-},\lambda\right)$ is determined from the upwelled spectral irradiance profile. It is recommended that this correction algorithm be applied to all $L_{\mathrm{u}}\left(0^{-},\lambda\right)$ and $E_{\mathrm{u}}\left(0^{-},\lambda\right)$ measurements used for SeaWiFS and SIMBIOS validation and algorithm development. Recognizing the provisional nature of the correction, however, the uncorrected measured values must also be reported. Moreover, the method and data used to estimate $a(\lambda)$, $E_{\mathrm{sun}}\left(\lambda\right)$ and $E_{\mathrm{sky}}\left(\lambda\right)$ must be documented and reported with all data sets corrected using this protocol.

Finite Bandwidth Correction

In wavelength regions where the absorption coefficient of water varies rapidly (*e.g.* near 565 nm), sensors having Full-Width at Half-Maximum (FWHM) bandwidths exceeding 5 nm interact with water attenuation spectrum to shift the effective wavelength of attenuation coefficients computed from the data. A protocol is not currently provided for correcting this effect.

Siegel *et al.* (1986) and Marshall and Smith (1990) discuss the effects of finite spectral FWHM bandwidth, and the normalized spectral response function, on determination of the attenuation coefficient, $K(\lambda)$,for a vertically homogeneous water column. Given a channel's nominal wavelength, $\bar{\lambda}$ and normalized spectral response function, $R_{\mathrm{n}}\left(\lambda\right)$, the apparent attenuation coefficient measured in a homogeneous water column is approximately

$$\hat{K}\left(z,\bar{\lambda}\right)=\frac{\int_{0}^{\infty}K\left(\lambda\right)R_{\mathrm{n}}\left(\lambda\right)e^{-K(\lambda)z}d\lambda}{\int_{0}^{\infty}R_{\mathrm{n}}\left(\lambda\right)e^{-K(\lambda)z}d\lambda}. \tag{2.31}$$

Marshall and Smith (1990) applied a correction for this effect to clear-water profiles of $E_{\mathrm{d}}\left(z,\lambda\right)$ at λ=589 nm. . In general, correction of $\hat{K}\left(z,\bar{\lambda}\right)$ for finite bandwidth effects associated with K for pure water is straightforward. Additional research will be needed to model, from the spectral irradiance data itself, additional bandwidth effects associated with attenuation by phytoplankton and other particles, and to correct $\hat{K}\left(z,\bar{\lambda}\right)$ accordingly.

Raman Corrections

Marshall and Smith (1990), and the references cited therein, show that transpectral Raman scattering contributes significantly to measured irradiance between 500 nm and 700 nm. At a particular wavelength, the Raman contribution is excited by ambient irradiance at a wavenumber shift of 3,400 cm^{-1}. For example, Raman scattering at a wavelength of 500 nm (20,000 cm^{-1}) is excited by light at wavelength 427 nm (23,400 cm^{-1}), and at 700 nm (14,286 cm^{-1}) by light at 565 nm (17,686,cm^{-1}). Marshall and Smith (1990) give a transverse Raman scattering cross section (at 90°) of $8.2\mathrm{x}10^{-30}$ $\mathrm{cm}^{-2}\mathrm{molecule}^{-1}\mathrm{sr}^{-1}$, a value within the range of other published observations. By integration, they derive a total Raman scattering coefficient of:

$$b_{\mathrm{r}}\left(488\right)=2.6\times10^{-4}\ \mathrm{m}^{-1}, \tag{2.32}$$

a result recently confirmed by Bartlett *et al.* (1998), as well as by the *in situ* measurements of Hu and Voss (1997a, 1997b).

The wavelength dependence of the Raman scattering cross section is theoretically about the same as that for Rayleigh scattering

$$b_{\mathrm{r}}\left(\lambda\right)\sim b_{\mathrm{r}}\left(488\right)\left(\frac{\lambda}{488}\right)^{-4}. \tag{2.33}$$

Bartlett *et al.* (1998) recently measured the wavelength dependence of Raman scattering, however, and found that for excitation wavelengths

$$b_r(\lambda) = b_r(488)\left(\frac{\lambda}{488}\right)^{-5.5\pm0.4}, \tag{2.34}$$

for radiance expressed in energy units $\left[\mu W\ cm^{-2} nm^{-1} sr^{-1}\right]$.

A method for applying Raman corrections to measured profiles of irradiance and radiance is suggested and applied to homogeneous clear-water profiles by Marshall and Smith (1990). Additional work is needed to develop a robust Raman scattering correction model for general application in more turbid and vertically stratified water masses. The relative magnitude, and thus importance, of the Raman signal at each wavelength in the upper three attenuation lengths should also be investigated more thoroughly than has been done to date. Gordon (1999) applied the recent results of Bartlett *et al.* (1998), *i.e.* the confirmation of (2.32) and wavelength dependence of (2.34), together with recently improved absorption coefficients for pure water (Sogandares and Fry 1997; Pope and Fry 1997), to model the relative contributions of Raman scattering to water-leaving radiance at wavelengths of interest for ocean color remote sensing. He found that Raman contributions ranged between 20 % and 30 % in clear, oligotrophic waters, and was ~8 % near chlorophyll concentrations of 1 mg m^{-3}. Protocols given in Volume III, Chapter 4 for determining exact normalized water-leaving radiance, $L_{WN}^{ex}(\lambda)$, include the effects of Raman scattering.

REFERENCES

Austin, R.W., 1974. The remote sensing of spectral radiance from below the ocean surface. In: *Optical Aspects of Oceanography*, N.G. Jerlov and E.S. Nielson, Eds., pp 317-344.

Baker, K.S., and R.C. Smith, 1990: Irradiance transmittance through the air/water interface. *Ocean Optics X*, R.W. Spinrad, Ed., *SPIE*, **1**,302, 556-565.

Bartlett, J.S., K.J. Voss, S. Sathyendranath, and A. Vodacek, 1998: Raman scattering by pure water and seawater. *Appl. Opt*., **37:** 3324-3332.

Gordon, H.R., 1985: Ship perturbations of irradiance measurements at sea, 1: Monte Carlo simulations. *Appl. Opt*., **24:** 4,172--4,182.

Gordon, H.R., 1999: Contribution of Raman Scattering to water-leaving radiance: a reexamination. *Appl. Opt*., **38:** 3166-3174.

Gordon, H.R., and K. Ding, 1992: Self shading of in-water optical instruments. *Limnol. Oceanogr.,* **37:** 491-500.

Helliwell, W.S., G.N. Sullivan, B. Macdonald, and K.J. Voss, 1990: Ship shadowing: model and data comparison. *Ocean Optics X*, R.W. Spinrad, Ed., *SPIE*, **1302:** 55-71.

Hooker, S.B. and S. Maritorena, 2000: An evaluation of oceanographic radiometers and deployment methodologies. *J. Atmos. Oceanic Technol*., 17: 811-830.

Hu, C. and K.J. Voss, 1997a: Solar stimulated inelastic light scattering in clear sea water, In: Ackleson , S.G. and R. Frouin, Eds: *Ocean Optics XIII*. Proc. *SPIE*, **2963**, 266-271.

Hu, C. and K.J. Voss, 1997b: *In situ* measurements of Raman scattering in clear ocean water, *Appl. Opt*. **36**,2686-2688.

Marshall, B.R., and R.C. Smith, 1990: Raman scattering and in-water optical properties, *Appl. Opt.,* **29:** 71-84.

Morel, A., and B. Gentili, 1996: Diffuse reflectance of oceanic waters. III. Implication of bidirectionality for the remote-sensing problem. *Applied Optics*, **35**: 4850-4862.

Mueller, J.L., 1995: Integral method for analyzing irradiance and radiance attenuation profiles. Ch. 3 In: Siegel, D.A., *et al.* 1995: Results of the SeaWiFS Data Analysis Round Robin, July 1994 (DARR-94). *NASA Tech. Memo. 104566, Vol.* ***26,*** S.B. Hooker and E.R. Firestone, Eds., NASA Goddard Space Flight Center, Greenbelt, Maryland, pp 44-48.

Mueller, J.L., and R.W. Austin, 1992: Ocean Optics Protocols for SeaWiFS Validation. *NASA Tech. Memo. 104566, Vol. **5**,* S.B. Hooker and E.R. Firestone, Eds., NASA Goddard Space Flight Center, Greenbelt, Maryland, 43 pp.

Mueller, J.L., and R.W. Austin, 1995: Ocean Optics Protocols for SeaWiFS Validation, Revision 1. *NASA Tech. Memo. 104566, Vol. **25**,* S.B. Hooker, E.R. Firestone and J.G. Acker, Eds., NASA Goddard Space Flight Center, Greenbelt, Maryland, 67 pp.

Neckel, H., and D. Labs, 1984: The solar radiation between 3,300 and 12,500 Å . *Solar Phys*., **90**: 205--258.

Pinder, G.F., and W.G. Gray, 1977: *Finite Element Simulation in Surface and Subsurface Hydrology*, Academic Press, 29 pp.

Siegel, D.A., C.R. Booth, and T.D. Dickey, 1986: Effects of sensor characteristics on the inferred vertical structure of the diffuse attentuation coefficient spectrum. *Ocean Optics VIII*, M.A. Blizard, Ed., *SPIE*, **637:** 115--124.

Siegel, D.A., M.C. O'Brien, J.C. Sorenson, D.A. Konnoff, E.A. Brody, J.L. Mueller, C.O. Davis, W.J. Rhea, and S.B. Hooker, 1995: Results of the SeaWiFS Data Analysis Round Robin, July 1994 (DARR-94). *NASA Tech. Memo. 104566, Vol. **26**,* S.B. Hooker and E.R. Firestone, Eds., NASA Goddard Space Flight Center, Greenbelt, Maryland, pp 44-48.

Smith, R.C., and K.S. Baker, 1984: Analysis of ocean optical data, *Ocean Optics VII*, M. Blizard, Ed., *SPIE*, **478:** 119--126.

Smith, R.C., and K.S. Baker, 1986: Analysis of ocean optical data. *Ocean Optics VIII,* P.N. Slater, Ed., *SPIE*, **637:** 95--107.

Sorensen, J.C., M.C. O'Brien, D.A. Konnoff, and D.A. Siegel, 1995: The BBOP data processing system. Ch. 2 In: Siegel, D.A., *et al.* 1995: Results of the SeaWiFS Data Analysis Round Robin, July 1994 (DARR-94). *NASA Tech. Memo. 104566, Vol. **26**,* S.B. Hooker and E.R. Firestone, Eds., NASA Goddard Space Flight Center, Greenbelt, Maryland, pp 37-43.

Toole, D.A., D.A. Siegel, D.W. Menzies, M.J. Neumann and R.C. Smith, 2000: Remote-sensing reflectance determinations in the coastal ocean environment: impact of instrumental characteristics and environmental variability. *Appl. Opt.*, **39:** 456-469.

Voss, K.J., J.W. Nolten, and G.D. Edwards, 1986: Ship shadow effects on apparent optical properties. *Ocean Optics VIII,* M. Blizard, Ed., *SPIE*, **637:** 186--190.

Waters, K.J., R.C. Smith, and M.R. Lewis, 1990: Avoiding ship induced light field perturbation in the determination of oceanic optical properties. *Oceanogr*., **3:** 18--21.

Zaneveld, J.R.V., E. Boss, and A. Barnard, 2001: Influence of surface waves on measured and modeled irradiance profiles. *Appl. Opt.*, **40:** 1442-1449.

Zibordi, G., and G.M. Ferrari, 1995: Instrument self-shading in underwater optical measurements: experimental data. *Appl. Opt.* **34:** 2750--2754.

Chapter 3

Above-Water Radiance and Remote Sensing Reflectance Measurement and Analysis Protocols

James L. Mueller[1], Curtiss Davis[2], Robert Arnone[3], Robert Frouin[4], Kendall Carder[5], Z.P. Lee[5], R.G. Steward[5], Stanford Hooker[6], Curtis D. Mobley[7] and Scott McLean[8]

[1]*Center for Hydro-Optics and Remote Sensing, San Diego State University, California*
[2]*Naval Research Laboratory, Washington, District of Columbia*
[3]*Naval Research Laboratory, Stennis Space Center, Mississippi*
[4]*Scripps Institution of Oceanography, University of California, San Diego, California*
[5]*University of South Florida, St. Petersburg, Florida*
[6]*NASA, Goddard Space Flight Center, Greenbelt, Maryland*
[7]*Sequoia Scientific Inc., Redmond, Washington*
[8]*Satlantic Inc., Halifax, Nova Scotia, Canada*

3.1 INTRODUCTION

As an alternative to the in-water methods of Volume III, Chapter 2, water-leaving radiance can be measured from the deck of a ship. A shipboard radiometer is used to measure radiance $L_{\mathrm{sfc}}\left(\lambda,\theta,\phi\in\Omega_{\mathrm{FOV}};\theta_{\mathrm{o}}\right)$ emanating from the sea surface at zenith angle θ (usually chosen between 30° and 50°) and azimuth angle ϕ (usually chosen between 90° and 180° away the sun's azimuth ϕ_{o}). In the convention used here, azimuth angles ϕ are measured relative to the sun's azimuth, *i.e.* $\phi_{\mathrm{o}} = 0$.

The surface radiance measured with a radiometer having a solid-angle field of view (FOV) of Ω_{FOV} sr may be expressed, following Mobley (1999), as

$$L_{\mathrm{sfc}}\left(\lambda,\theta,\phi\in\Omega_{\mathrm{FOV}};\theta_{\mathrm{o}}\right)=L_{\mathrm{W}}\left(\lambda,\theta,\phi\in\Omega_{\mathrm{FOV}};\theta_{\mathrm{o}}\right)+\rho L_{\mathrm{sky}}\left(\lambda,\theta_{\mathrm{sky}},\phi_{\mathrm{sky}}\in\Omega'_{\mathrm{FOV}};\theta_{\mathrm{o}}\right). \tag{3.1}$$

$L_{\mathrm{W}}\left(\lambda,\theta,\phi\in\Omega_{\mathrm{FOV}};\theta_{\mathrm{o}}\right)$ is water-leaving radiance centered at angles (θ, ϕ) and averaged over Ω_{FOV} [as weighted by the radiometer's directional response function (see Volume II, Chapters 2 and 3)]. $L_{\mathrm{sky}}\left(\lambda,\theta_{\mathrm{sky}},\phi_{\mathrm{sky}}\in\Omega'_{\mathrm{FOV}};\theta_{\mathrm{o}}\right)$ is sky radiance measured with the radiometer looking upward at angles (θ_{sky}, ϕ_{sky}). In practice, θ and θ_{sky} are numerically equal angles in the nadir and zenith directions, respectively, and the sea and sky viewing azimuths $\phi = \phi_{\mathrm{sky}}$. The reflectance factor ρ is operationally defined as the total skylight actually reflected from the wave-roughened sea surface into direction (θ,ϕ) divided by sky radiance measured with the radiometer from direction (θ_{sky},ϕ_{sky}), both quantities being averaged over Ω_{FOV} (Mobley 1999). Remote sensing reflectance is then determined, using water-leaving radiance calculated from (3.1), as

$$R_{\mathrm{RS}}\left(\lambda,\theta,\phi\in\Omega_{\mathrm{FOV}};\theta_{o}\right)=\frac{L_{\mathrm{W}}\left(\lambda,\theta,\phi\in\Omega_{\mathrm{FOV}};\theta_{\mathrm{o}}\right)}{E_{\mathrm{S}}\left(\lambda;\theta_{\mathrm{o}}\right)}, \tag{3.2}$$

where $E_{\mathrm{S}}(\lambda;\theta_{\mathrm{o}})$ is incident spectral irradiance measured above the sea surface. All of the above variables vary with solar zenith angle θ_{o}.

A simplified notation is used in Volume III, Chapter 2 (and elsewhere in the protocols) when discussing water leaving radiance $L_{\mathrm{W}}(\lambda)$ and remote sensing reflectance $R_{\mathrm{RS}}(\lambda)$ derived from in-water profile measurements of $L_{\mathrm{u}}(z,\lambda)$. Because $L_{\mathrm{u}}(z,\lambda)$ is measured in water viewing the nadir direction, $L_{\mathrm{W}}(\lambda)$ represents radiance leaving the

surface in the zenith direction (θ, ϕ) = (0°, 0°). Therefore, $L_W(\lambda)$ in, *e.g.*, Volume III, Chapter 2 corresponds to $L_W\left(\lambda, 0, 0 \in \Omega_{FOV}; \theta_o\right)$, and $R_{RS}(\lambda)$ to $R_{RS}\left(\lambda, 0, 0 \in \Omega_{FOV}; \theta_o\right)$, in the present notation .

3.2 PROPOSED MEASUREMENT CONCEPTS

Proposed protocols for measuring remote sensing reflectance group essentially into three basic categories of measurement concepts, each of which is described briefly in this section. Remote sensing reflectance determination by some, but not all three, of the proposed above-water methods have been compared to each other (Hooker *et al*. 1999, 2000). Comparisons have also been made between each method and $R_{RS}(\lambda)$ determined from in-water $L_u(z,\lambda)$ and above-water $E_s(\lambda;\theta_o)$ measurements (*e.g.* Rhea and Davis, 1997; Mueller *et al*. 1997; Fougnie *et al*. 1999; Hooker *et al*. 1999), finding root-mean-square differences generally larger than 20 % for any sample spanning a reasonably large range of environmental conditions. Some of these investigators have normalized the measurements, using the method of Morel and Gentili (1996) to account for variations in viewing and solar zenith angles and in the ocean Bidirectional Reflectance Distribution Function (BRDF), prior to making the comparisons (*e.g.* Mueller *et al.* 1997; Toole *et al*. 2000), and some have not (*e.g.* Rhea and Davis 1997; Fougnie *et al*. 1999).

Method 1: Calibrated radiance and irradiance measurements.

Radiometers that have been fully characterized and calibrated, following the methods of Volume II, Chapter 3, are used to measure $L_{sfc}\left(\lambda, \theta, \phi \in \Omega_{FOV}; \theta_o\right)$, $L_{sky}\left(\lambda, \theta_{sky}, \phi_{sky} \in \Omega'_{FOV}; \theta_o\right)$ and $E_s(\lambda;\theta_o)$. Assumptions are chosen to estimate surface reflectance ρ, and $L_W\left(\lambda, \theta, \phi \in \Omega_{FOV}; \theta_o\right)$ and $R_{RS}\left(\lambda, \theta, \phi \in \Omega_{FOV}; \theta_o\right)$ are calculated using equations (3.1) and (3.2). Example implementations of this straightforward instrumental approach, and comparisons with remote sensing reflectance determined from in-water measurements, are described in Rhea and Davis (1997), Mueller *et al*. (1997), Hooker *et al*. (1998), Hooker and Lazin (2000), and Toole *et al*. (2000).

Method 2: Uncalibrated radiance and reflectance plaque measurements

In this approach, a radiance sensor that has not necessarily been calibrated is used to measure signals proportional to $L_{sfc}\left(\lambda, \theta, \phi \in \Omega_{FOV}; \theta_o\right)$, $L_{sky}\left(\lambda, \theta_{sky}, \phi_{sky} \in \Omega'_{FOV}; \theta_o\right)$ and radiance reflected from a horizontal plaque, or "gray-card", having a known bi-directional reflectance (often assumed to be near-Lambertian) for the solar and viewing directions. The raw uncalibrated radiance signals are substituted in (3.1) to express $L_W\left(\lambda, \theta, \phi \in \Omega_{FOV}; \theta_o\right)$ as

$$L_W\left(\lambda, \theta, \phi \in \Omega_{FOV}; \theta_o\right) = F_L\left(\lambda\right)\left[S_{sfc}\left(\lambda, \theta, \phi \in \Omega_{FOV}; \theta_o\right) - \rho S_{sky}\left(\lambda, \theta_{sky}, \phi_{sky} \in \Omega'_{FOV}; \theta_o\right)\right], \qquad (3.3)$$

where $F_L(\lambda)$ is the instrument's unknown radiance response calibration factor, and $S_{sfc}\left(\lambda, \theta, \phi \in \Omega_{FOV}; \theta_o\right)$ and $S_{sky}\left(\lambda, \theta_{sky}, \phi_{sky} \in \Omega'_{FOV}; \theta_o\right)$ are the radiometer's measured responses. The radiance reflected from the plaque is scaled to estimate $E_s(\lambda;\theta_o)$ as

$$E_S\left(\lambda; \theta_o\right) = \frac{\pi F_L\left(\lambda\right) S_g\left(\lambda, \theta_g, \phi_g \in \Omega_{FOV}; \theta_o, \phi_o\right)}{R_g\left(\lambda, \theta_g, \phi_g \in \Omega_{FOV}; \theta_o, \phi_o\right)}, \qquad (3.4)$$

where $S_g\left(\lambda, \theta_g, \phi_g \in \Omega_{FOV}; \theta_o, \phi_o\right)$ is the sensor response signal when the plaque (gray-card) is viewed at angles $\left(\theta_g, \phi_g\right)$ with the sun at $\left(\theta_o, \phi_o\right)$, and $R_g\left(\lambda, \theta_g, \phi_g \in \Omega_{FOV}; \theta_o, \phi_o\right)$ is the plaque's bi-directional reflectance function (BRDF) for that sun and viewing geometry [including whatever is assumed regarding the contribution of sky irradiance to $E_s(\lambda;\theta_o)$]. The most straightforward BRDF geometry is for the sensor to view the center of the plaque normal to its surface (*i.e.* $\theta_g = 0$), allowing the BRDF to be determined for illumination angles between normal and 90° at, *e.g.* 5° increments. When expressions (3.3) and (3.4) are substituted into (3.2) to calculate $R_{RS}\left(\lambda, \theta, \phi \in \Omega_{FOV}; \theta_o\right)$, the unknown radiance response calibration factor $F_L(\lambda)$ cancels. As with the other

methods, the reflectance of the sea surface ρ is estimated using one of several possible sets of assumptions and approximations.

For quantitative determinations of $E_S(\lambda;\theta_O)$ and $L_W\left(\lambda,\theta,\phi\in\Omega_{FOV};\theta_o\right)$ by this method, the radiometer must be calibrated to determine the coefficients $F_L(\lambda)$.

This method was adapted for ocean color applications, initially by Carder and Steward (1985), from an approach used widely in the LANDSAT remote sensing community to measure reflectance spectra of terrestrial surfaces. Carder *et al*. (1993) used the method with a vertical polarizer to minimize reflected skylight, and Lee *et al*. (1997b) compared measurements with and without the polarizer (and found little difference – a result subsequently explained by Fougnie *et al*. 1999). Other aspects and applications of this approach are described in Lee *et al*. (1997a). In particular, they spectrally deconvolve the Rayleigh from aerosol skylight reflected from the sea surface using a Fresnel value for the Rayleigh, and a variable reflectance value for wave-modulated aerosol radiance. When sunglint is not an issue, the (θ, ϕ) = (30°, 90°) angle provides less uncertainty due to wave modulation in the Fresnel reflectance using the Lee *et al*. (1997a) method. Rhea and Davis (1997), Toole *et al*. (2000), and Hooker *et al*. (1999) compared reflectances determinations by this method with determinations from in-water measurements.

Method 3: Calibrated surface polarized radiance measurements with modeled irradiance and sky radiance

A radiance sensor is fitted with a polarizing filter set to pass only vertically polarized component of viewed radiance. The polarizer minimizes the skylight reflectance term in (3.1) when the surface is viewed near the Brewster angle. The instrument is calibrated using the methods of Volume II, Chapter 4, and is used to measure only $L_{sfc}\left(\lambda,\theta,\phi\in\Omega_{FOV};\theta_o\right)$. A sun photometer is used to determine aerosol optical thicknesses at each wavelength (Volume III, Chapter 5). A radiative transfer model is then used to calculate $E_S(\lambda;\theta_O)$ and $L_{sky}\left(\lambda,\theta_{sky},\phi_{sky}\in\Omega'_{FOV};\theta_o\right)$ so that (3.1) and (3.2) may be solved for $R_{RS}\left(\lambda,\theta,\phi\in\Omega_{FOV};\theta_o\right)$. The details of this method, which is the protocol recommended for use with the SIMBAD radiometer (see also Volume II, Chapter 4 and Volume III, Chapter 5), are described by Fougnie *et al*. (1999).

Exact Normalized Remote Sensing Reflectance

The remote sensing reflectances determined by any of the above methods are not comparable with each other for different days or viewing angles, with satellite ocean color determinations of $R_{RS}(\lambda)$, or with $R_{RS}(\lambda)$ determined from in-water measurements. For these purposes, measured $R_{RS}\left(\lambda,\theta,\phi\in\Omega_{FOV};\theta_o\right)$ must be converted to *exact normalized remote sensing reflectance*, defined as

$$R_{RS}^{ex}(\lambda)\equiv\frac{L_{WN}^{ex}(\lambda)}{\overline{F}_o(\lambda)}, \tag{3.5}$$

where $\overline{F}_o(\lambda)$ is mean solar irradiance above the atmosphere (Neckel and Labs, 1984), and the *exact normalized water-leaving radiance* $L_{WN}^{ex}(\lambda)$ is defined in Volume III, Chapter 4, together with protocols for determining it from $R_{RS}\left(\lambda,\theta,\phi\in\Omega_{FOV};\theta_o\right)$.

3.3 RADIOMETRIC MEASUREMENT METHODS

Field of View Considerations

In the protocols for determining $L_W(\lambda)$ from in-water measurements of radiance profiles (Volume III, Chapter 2 and Volume VI, Chapters 2 and 3), the radiance sensor's angular FOV is not critical, because the upwelling radiance distribution varies relatively little over zenith angles up to 20°. When measuring $L_{sfc}\left(\lambda,\theta,\phi\in\Omega_{FOV};\theta_o\right)$, however, the size of an instrument's solid angle FOV Ω_{FOV} affects its sensitivity to variability in the skylight reflection term of (3.1) (Lee *et al*. 1997a; Fougnie *et al*. 1999; Mobley 1999). This situation arises because the slope of the wind roughened sea surface varies spatially and temporally on scales small compared to the typical area subtended by

Ω_{FOV} and sensor integration time, respectively. The surface slope distribution varies strongly as a function of, and may be estimated from, local wind speed (Cox and Munk 1954). For a small area of sea surface at a fixed location, wind gustiness may cause variations in the slope distribution (visible as "cat's paws") on time scales from seconds to minutes. The surface slope distribution is also systematically varied on time scales of order 10 sec by gravity waves, primarily through interactions with capillary waves through periodic modulations of surface tension, and secondarily by very small direct variations in surface slope (gravity waves break before slopes reach 6°). [In SIMBAD measurements of polarized surface radiance, for example, the oscillations associated with the primary swell appear clearly in the data. The minimum values are selected in the data processing. (R. Frouin, Pers. Comm.)]

The average surface slope variability, in combination with angular variability in $L_{\text{sky}}\left(\lambda,\theta_{\text{sky}},\phi_{\text{sky}}\in\Omega'_{\text{FOV}};\theta_{\text{o}}\right)$, introduces strong variability in the skylight reflectance term of (3.1), which increases remarkably with a large Ω_{FOV} (Mobley 1999; Fougnie *et al*. 1999; Toole *et al*. 2000). With a very small Ω_{FOV}, on the other hand, measurements made from close above the surface view an extremely small area that is subject to large temporal variations in slope, and thus also in the directions in which the sky is viewed through surface reflection. The ideal, which can only be effectively realized from satellite orbital elevations above the earth's surface, is a very small Ω_{FOV} (to minimize viewing angle variation across the FOV) combined with a subtended surface area (pixel) large enough to average surface slope variations associated with wind gusts, capillary waves and gravity waves.

Large FOV measurements also integrate over a significant range of variability in the ocean's BRDF, and it may prove difficult to determine exact normalized remote sensing reflectance $R_{\text{RS}}^{ex}(\lambda)$ [Equation (3.5)] from these data (Volume III, Chapter 4, and references cited therein).

Full-angle FOV's used, or assumed in model computations, by various investigators have ranged from approximately 2° (*e.g.* Fougnie *et al.* 1999) up to 18° (*e.g.* Gould *et al*. 2000).

Radiance Measurements

The surface and sky radiance measurements should be made from a location that minimizes both shading and reflections from superstructure. A good position for measuring the water-leaving radiance may often be found near the bow of the ship. Especially while steaming, ocean color radiance measurements should usually be made from the bow, because from this location it is practical to view a spot where the water is undisturbed by the ship's wake or associated foam. It must also be easy, in the selected position, to point in a direction away from the sun to reduce specular reflection of sunlight.

To measure $L_{\text{sfc}}\left(\lambda,\theta,\phi\in\Omega_{\text{FOV}};\theta_{\text{o}}\right)$ the radiometer should be pointed toward the sea surface at viewing angles, measured at the pixel, $(\theta, \phi) = (40\text{-}45^o, 135^o)$, if possible (Mobley 1999; Fougnie *et al*. 1999), and in all circumstances the viewing azimuth must be in the range $90^o < \phi < 180^o$ relative to the sun's azimuth. For polarized measurements a viewing angle of $\theta = 45^o$ is strongly recommended (Fougnie *et al*. 1999). A viewing angle that is 180° away from the sun's azimuth should be avoided. The measurements at this angle may be contaminated by the *glory* phenomenon, and ship shadow might also be a problem in this configuration. Measurements should also not be made when the sun is close overhead ($\theta_O < 20^o$), for reasons discussed in Section 3.4 (Mobley *et al*. 1999). In addition, whitecaps, foam and floating material should be avoided during measurements, but at wind speeds exceeding 10 m s^{-1} extensive whitecap coverage may unavoidably contaminate the data record to some extent.

Because of temporal variability in surface reflectance, due to wind gusts and waves, it is important to record a number of spectra within a period of several seconds, or minutes if necessary. With filter radiometers (Mueller 1997; Fougnie *et al*. 1999; Hooker *et al*. 1999, 2000), it is feasible to sample individual spectra at rates of several Hz, and the electronic gain changes account for the different magnitudes of the water and sky signals.

If miniature, fiber-optic spectroradiometers are used, on the other hand, the detector integration time is varied to provide the necessary dynamic range. Sky radiances may be integrated over a few hundred msec, while the ocean surface radiance may be integrated over 1 sec to 2 sec. A separate dark reading must be obtained each time the integration time is changed. A typical measurement sequence with this type of spectroradiometer is to measure plaque-reflected, sea and sky and radiances (each preceded by a dark offset reading), in that order, and repeat the sequence 5 or more times.

Data records of longer duration may be advisable to improve averaging over modulation of capillary waves by wind variability and gravity waves, but there has been little research on that aspect of the problem. Before calculating final mean and standard deviation spectra, positive outliers due to briefly viewed foam patches, whitecaps and strong glint should be removed by inspection of the data record.

When using *Method 3*, described above, only $L_{\mathrm{sfc}}\left(\lambda,\theta,\phi\in\Omega_{\mathrm{FOV}};\theta_{\mathrm{o}}\right)$ need be measured, together with a sun photometer measurement, and $L_{\mathrm{sky}}\left(\lambda,\theta_{\mathrm{sky}},\phi_{\mathrm{sky}}\in\Omega'_{\mathrm{FOV}};\theta_{\mathrm{o}}\right)$ and $E_{\mathrm{S}}(\lambda;\theta_{\mathrm{o}})$ are modeled. This can only be done accurately when clouds do not obscure the solar disk and fractional cloud cover is less than 20 %. These are the necessary conditions for the measurement.

To measure $L_{\mathrm{sky}}\left(\lambda,\theta_{\mathrm{sky}},\phi_{\mathrm{sky}}\in\Omega'_{\mathrm{FOV}};\theta_{\mathrm{o}}\right)$ (*Methods 1 and 2*), the radiometer is pointed upward to view the sky at angles (θ_{sky}, ϕ_{sky}) = (θ, ϕ), *e.g.* (40°, 135°). When pointing the radiometer, θ_{sky} is measured from the zenith, and θ from the nadir, directions as seen from the ship. In radiative transfer calculations, the origin is taken to be located at the pixel and both angles are zenith angles (following the usual convention used in, *e.g.*, ocean color atmospheric correction algorithms). When measurements are made in partly cloudy sky conditions, viewing angles should be selected to cover a clear segment of the sky, if possible. Corrections for reflected sky radiance are problematic unless the cloud fraction is very small in the hemisphere centered on the selected viewing azimuth (Mobley 1999).

Ideally, it can be argued that sky radiance should be measured simultaneously with $L_{\mathrm{sfc}}\left(\lambda,\theta,\phi\in\Omega_{\mathrm{FOV}};\theta_{\mathrm{o}}\right)$ and $E_{\mathrm{S}}(\lambda;\theta_{\mathrm{o}})$, using separate radiometers (*e.g.* Hooker *et al*. 1999). For reasons of economy, however, most investigators will use the same radiometer for both radiance measurements, which therefore, must be measured sequentially (*e.g.* Carder and Steward 1985; Lee *et al*. 1997; Mueller 1997). If separate radiometers are used, they must be calibrated and fully characterized (Volume II, Chapters 3 and 4), following the approach described above as *Method 1* (although one could use two calibrated radiance sensors, and still use a reflectance plaque to estimate $E_{\mathrm{S}}(\lambda;\theta_{\mathrm{o}})$ as in *Method 2*).

Incident Irradiance Measurements

Measurements of $E_{\mathrm{S}}(\lambda;\theta_{\mathrm{o}})$ with a calibrated irradiance sensor are an essential component of *Method 1* (above). The radiometer should be mounted in a location that is free of both shadows and reflections of light from any part of the ship's superstructure (see also Volume III, Chapter 2, Section 2.2). This can usually be accomplished by mounting the radiometer high on a mast, albeit in some combinations of location and ship's heading, intermittent shadowing by antennas, stays and other parts of the ship's rigging may contaminate the $E_{\mathrm{S}}(\lambda;\theta_{\mathrm{o}})$ measurements. The data must also be edited to remove measurements when the irradiance collector's orientation is more than 5° away from horizontal. When a hand-held irradiance sensor is used to measure $E_{\mathrm{S}}(\lambda;\theta_{\mathrm{o}})$ at the same location where $L_{\mathrm{sfc}}\left(\lambda,\theta,\phi\in\Omega_{\mathrm{FOV}};\theta_{\mathrm{o}}\right)$ and $L_{\mathrm{sky}}\left(\lambda,\theta_{\mathrm{sky}},\phi_{\mathrm{sky}}\in\Omega'_{\mathrm{FOV}};\theta_{\mathrm{o}}\right)$ are measured, it may be more difficult to find an ideal location on some ships.

Time series of $E_{\mathrm{S}}(\lambda;\theta_{\mathrm{o}})$ should be recorded synchronously with measurements of both $L_{\mathrm{sfc}}\left(\lambda,\theta,\phi\in\Omega_{\mathrm{FOV}};\theta_{\mathrm{o}}\right)$ and $L_{\mathrm{sky}}\left(\lambda,\theta_{\mathrm{sky}},\phi_{\mathrm{sky}}\in\Omega'_{\mathrm{FOV}};\theta_{\mathrm{o}}\right)$. If the average incident irradiances associated with the surface and sky radiance measurements agree within a few percent, their ratio should be used to scale one, or the other, radiance to adjust for the apparent change in atmospheric radiometric conditions during the time interval between the two measurements. If the average $E_{\mathrm{S}}(\lambda;\theta_{\mathrm{o}})$ values differ significantly, the entire measurement sequence is suspect and the data should be flagged as suspect, and probably discarded. In this quality control context, time series measurements of $E_{\mathrm{S}}(\lambda;\theta_{\mathrm{o}})$ with a deck cell may also be useful when either *Method 2* or *3* is used to determine $R_{\mathrm{RS}}\left(\lambda,\theta,\phi\in\Omega_{\mathrm{FOV}};\theta_{\mathrm{o}}\right)$.

Reflectance Plaque Measurements

When following *Method 2* (above), a Spectralon™ (or alternative material) reflectance plaque having a known BRDF is used to normalize the uncalibrated radiance measurements for $E_s(\lambda;\theta_o)$. In this approach, an accurately characterized BRDF for the plaque is as critical as are the accuracies of radiometric calibrations in *Methods 1 and 3*. Traditionally, gray reflectance plaques with approximately 10 % nominal reflectance have been used for this measurement (Carder and Steward 1985; Rhea and Davis 1997; Hooker *et al*. 1999), but white Spectralon plaques with 99 % reflectance offer better homogeneity in BRDF (over the plaques surface area) and have been used by some investigators (*e.g.* Hooker *et al*. 1999; Toole *et al*. 2000).

The plaque must be held horizontally, and exposed to the sun and sky in a position free from both shading by, and reflections from, any part of the ship's superstructure, observer, or radiometer, and also afford an unobstructed view of the sea surface at an acceptable (θ, ϕ) relative to the sun[2]. The radiance sensor is aligned to view the plaque at angles consistent with the solar direction and the plaque's BRDF characterization. The simplest approach is to determine the BRDF as a function of varying source zenith angles for the sensor view normal to the plaque center, and use that viewing geometry in the field. Finally, the radiance reflected from the plaque is recorded.

Sun Photometer Measurements

It is strongly recommended that sun photometer measurements be made to determine aerosol optical thickness, following the protocols of Volume III, Chapter 5, coincident with every set of above-water remote-sensing reflectance measurements. Note that this measurement is an essential element of *Method 3* (above), where it is needed to correctly model $L_{\mathrm{sky}}\left(\lambda,\theta_{\mathrm{sky}},\phi_{\mathrm{sky}}\in\Omega'_{\mathrm{FOV}};\theta_{\mathrm{o}}\right)$ and $E_s(\lambda;\theta_o)$ (Fougnie *et al*. 1999).

Ancillary Measurements and Records

The following ancillary data and information must be recorded in header files and/or logs for each radiometric measurement:

1. date and time (UTC) of the station and cast;
2. geographic location (latitude and longitude in decimal degrees to the nearest 0.001);
3. the viewing zenith and azimuth angles of surface and sky radiance, and the solar azimuth relative to the ship's heading;
4. the direction of the sun relative to the ship's heading;
5. cloud cover and sky conditions;
6. wind speed and direction;
7. sea state, as significant wave height, whitecap fraction, and the direction, height and period of the dominant swell. period);
8. barometric pressure;
9. Secchi depth;
10. dark (zero-offset) data file, to be recorded, and the dark filename logged, at the time of the measurements;

™ "Spectralon" is a registered trademark of Labsphere, Inc. As stated elsewhere in this document, commercially available equipment items are referred to only as illustrative examples. Such references do not recommend the use of these specific equipment items, nor do they imply that they are necessarily the best equipment for the particular purpose described in the text.

[2] It may be difficult, on some ships, to find a location that fully meets these requirements. In such situations, the alternative above-water methods should be considered.

11. times, locations and file identification of associated CTD, *in situ* fluorescence, in-water radiometry and inherent optical property profiles, if any;
12. geographic locations, times and depths of associated water samples, if any;
13. names of files with data from comparisons with a portable radiometric reference standard measured in the field to track the instrument's stability during a deployment (Volume II, Chapter 5);
14. instrument identification; and
15. calibration date and file identification (constant throughout a cruise, usually).

Protocols describing measurement and analysis methods for the standard ancillary variables (Volume I, Chapter 3, Table 3.1) are presented in Volume I, Chapter 4.

Wind speed and direction, sea state, and sky conditions are essential information for accurate corrections for reflected sky radiance (see below). Photographs of sky and sea surface conditions are highly desirable. Viewing and solar geometry are fundamental to this type of measurement.

It is desirable to also measure in-water radiometric and IOP profiles at stations where above-water measurements of remote-sensing reflectance are made.

3.4 SKY RADIANCE REFLECTANCE OF THE SEA SURFACE

For a flat sea surface and a uniform sky radiance distribution, ρ reduces to the Fresnel reflectance of the sea surface averaged over Ω_{FOV} (see also Volume I, Chapter 2, Section 2.5). In this limit, $\rho \approx 0.02$ for $\theta \leq 30°$ and increases slowly to $\rho \approx 0.03$ at $\theta \cong 40°$ (Austin 1974). The sea surface is usually wave-roughened and clear sky radiance distributions are not uniform, however, with the result that ρ can be much significantly larger than these simple values and is furthermore very difficult to determine for most wind and sea state conditions (Mobley, 1999; Fougnie *et al.* 1999; Lee *et al.* 1997; Mueller *et al*. 1997; Toole *et al.* 2000).

Clear Skies

In general, the sky radiance reflectance of the sea surface is an apparent optical property that has a functional dependence on many variables, $\rho = \rho(\theta_{sky}, \phi_{sky}, \theta, \phi, \Omega_{FOV}$, wind speed, sea state, sky radiance distribution), the complexities of which have been rigorously explored using radiative transfer computations by Mobley (1999) for unpolarized radiance. Assuming $(\theta, \phi) = (40^o, 135^o)$ and a clear-sky radiance distribution for a solar zenith angle $\theta_o = 30^o$, Mobley's results show that ρ increases from 0.026 with wind speed U = 0 m s^{-1} to approximately 0.043 when U = 15 m s^{-1}. As solar zenith angles increase, the upper limit of ρ at U = 15 m s^{-1} decreases monotonically to a value $\rho \approx 0.036$ at $\theta_o = 80^o$. For viewing angles $(\theta, \phi) = (30^o, 90^o)$, the clear-sky ρ at U = 15 m s^{-1} is ~0.08 when $\theta_o = 30^o$ and is comparable to $(\theta, \phi) = (40^o, 135^o)$ for $\theta_o > 40^o$. For solar zenith angles $\theta_o > 30^o$, Mobley found that the clear-sky ρ for $(\theta, \phi) = (40^o, 135^o)$ was independent of wavelength at all wind speeds. For viewing angles $(\theta, \phi) = (30^o, 90^o)$, however, he found that clear-sky ρ at U = 15 m s^{-1} varied by factor of 2 over wavelength due to the spectral differences between reflected skylight and sun glint. For both sets of viewing angles, the reflectance factor ρ increases much more rapidly with wind speed for $\theta_o < 30^o$, due to increased sun glint, and this type of measurement would not seem to be practical at solar zenith angles $\theta_o < 20^o$. It is perhaps noteworthy that, at least with present atmospheric correction algorithms, sun glint also renders satellite ocean color measurements unusable when the sun is less than 20° from zenith.

Fougnie *et al*. (1999) made similar model calculations, and experimentally verified them, for vertical and horizontally polarized components of reflected skylight. Their model calculations showed that for a rough water surface, the zenith angle where vertically polarized reflectance is a minimum shifts from the Brewster angle, approximately $\theta = 52^o$, to approximately $\theta = 45^o$. They also found that the minimum reflected skylight effect was obtained at viewing angles $(\theta, \phi) = (45^o, 135^o)$. For the more widely used viewing angles $(\theta, \phi) = (30^o, 90^o)$ (Carder and Steward 1985; Lee *et al*. 1997; Mueller *et al*. 1997), vertically and horizontally polarized reflectances are both

larger and nearly equal, which explains why no significant differences were found between total and vertically polarized measurements at these angles by Lee *et al.* (1997), or Mueller *et al*. (1997).

Scattered and Broken Clouds

Radiance scattered from clouds is typically greater than, and spectrally different from, clear-sky radiance. Therefore, the presence of randomly distributed clouds within 90° of the viewing azimuth ϕ may significantly increase the magnitude of reflected skylight and alter its wavelength dependence, a phenomenon noted by many investigators (*e.g.* Mobley 1999; Toole *et al*. 2000; Fougnie *et al*. 1999). Moreover, the temporal variability and uncertainty of both attributes of reflected skylight are increased in these conditions. Obviously, effects related to mixed cloudy and cloud-free segments of the sky become progressively more pronounced as wind speed increases, and the effectiveness of correction algorithms becomes problematic in these circumstances (Mobley 1999).

Overcast Skies

When skies are totally overcast, the sky radiance distribution becomes more uniform and its wavelength dependence becomes gray (Mobley 1999; Toole *et al*. 2000). There is some evidence that $R_{\mathrm{RS}}\left(\lambda,\theta,\phi\in\Omega_{\mathrm{FOV}};\theta_{\mathrm{o}}\right)$ determined from above-water measurements under overcast skies may have significantly lower uncertainty than can be realized in either clear skies or partially cloudy skies (Toole 2000). Measurements under cloudy skies are of little interest in the context of SIMBIOS and SeaWiFS validation studies. On the other hand, measurements under overcast conditions provide insight into phytoplankton dynamics under conditions that cannot be observed from space.

Residual Reflectance Corrections

If the ocean is assumed to be totally absorbing ("black") at 750 nm (and longer wavelengths), then we should find $R_{\mathrm{RS}}\left(750,\theta,\phi\in\Omega_{\mathrm{FOV}};\theta_{\mathrm{o}}\right)=0$ if the reflected skylight term is properly estimated in equation (3.1). Following the "quick and easy" algorithm of Carder and Steward (1985), if it is further assumed that any error in skylight reflection term is white (not wavelength dependent), one may apply a calculated value of $R'_{\mathrm{RS}}\left(750,\theta,\phi\in\Omega_{\mathrm{FOV}};\theta_{\mathrm{o}}\right)\neq 0$ as a simple offset correction at other wavelengths, *i.e.*

$$R_{\mathrm{RS}}\left(\lambda,\theta,\phi\in\Omega_{\mathrm{FOV}};\theta_{\mathrm{o}}\right)=R'_{\mathrm{RS}}\left(\lambda,\theta,\phi\in\Omega_{\mathrm{FOV}};\theta_{\mathrm{o}}\right)-R'_{\mathrm{RS}}\left(750,\theta,\phi\in\Omega_{\mathrm{FOV}};\theta_{\mathrm{o}}\right).$$

This adjustment was previously recommended as part of the provisional protocol for determining above-water remote sensing reflectance (Mueller and Austin 1995). Other suggested wavelengths that have been suggested for determining such a "black-ocean" residual offset include 670, 765, 865 and 1012 nm (Hooker *et al*. 1999).

In turbid coastal waters, where the above-water technique would be most useful, it is clearly not appropriate to assume that $R_{\mathrm{RS}}\left(750,\theta,\phi\in\Omega_{\mathrm{FOV}};\theta_{\mathrm{o}}\right)=0$ (Sydor and Arnone 1997; Sydor *et al*. 1998; Lee *et al*. 1997; Gould *et al*. 2000). Moreover, skylight reflection variability, and uncertainty in its estimation, is largely associated with sun glint and radiance from clouds, neither of which produces a strictly white offset (Lee *et al*. 1997; Mobley 1999).

Lee *et al*. (1997) proposed an alternative algorithm that partitions the skylight reflectance term of (3.1) into Rayleigh (λ^{-4} dependence) and aerosol (λ^{-n} dependence, n to be determined on a case-by-case basis) scattering terms, using a non-linear optimization analysis to minimize residuals from expected spectral variations in remote-sensing reflectance at a selected set of wavelengths.

Gould *et al*. (2000) proposed an algorithm to partition the surface radiance at 720 nm into remote-sensing reflectance and sky reflectance components estimated from the difference between apparent reflectances measured at 715 and 735 nm. Following Lee *et al*. (1997), they assumed a coefficient for exponential wavelength dependence and extrapolated the skylight reflectance to lower wavelengths. When *in situ* IOP are also measured at a station, they derived an improved wavelength dependence model for the sky reflectance correction based on remote-sensing reflectance at 40 nm calculated from *a*(400) and *b*(400).

Sydor *et al.* (1998) proposed combining polarized and unpolarized measurements to derive an estimate of the wavelength dependence of reflected skylight. These wavelength-dependency approaches show initial promise, and

with further development and experimental validation, some variant on these methods may yet lead to a robust algorithm for correcting above-water determinations of remote-sensing reflectance.

So far, evaluations of the uncertainty associated with the simple white-offset adjustment have not supported its general use, on either experimental (Lee *et al*. 1997; Hooker *et al*. 1999; Toole *et al*. 2000) or theoretical (Mobley 1999) grounds. Its use is not recommended in the present version of the protocols, even though the results of Toole *et al*. (2000) suggest it may be appropriate under totally overcast skies.

3.5 DISCUSSION AND RECOMMENDATIONS

The protocols recommended, provisionally, in Mueller and Austin (1995) for above-water measurements of $R_{\mathrm{RS}}\left(\lambda,\theta,\phi\in\Omega_{\mathrm{FOV}};\theta_{\mathrm{o}}\right)$ were seriously flawed. The viewing zenith angles (20°) recommended there were too small to avoid serious sun glint contamination. The recommendation that one might measure sky radiance using a first surface mirror would, if followed, introduce significant repolarization of the measured radiance and yield a serious radiometric artifact. And finally, two key equations of that protocol contained serious typographical errors. The Mueller and Austin (1995) protocols related to above-water measurements of water-leaving radiance and remote-sensing reflectance should not be followed under any circumstances.

The above-water methods for determining normalized remote-sensing reflectance (NRSR)[3], as described above, and their associated uncertainty budgets, have been discussed at length in several meetings and workshops over the last few years, as well as in the literature cited here. In particular, a SIMBIOS sponsored NRSR Workshop was held at Old Dominion University (Norfolk, VA) in December 1997. At that workshop, the participants agreed that the uncertainty budgets associated with the above-water methods proposed for determining NRSR are poorly known, and that a unified data set was needed as a basis for correcting that deficiency. It was also the workshop consensus that additional research and analyses should be pursued to:

1. Determine uncertainties in and between $E_{\mathrm{S}}(\lambda;\theta_{\mathrm{o}})$ determined by a) direct measurement with a calibrated radiometer (*Method 1*), b) estimation based on measurement of radiance reflected from a gray target have a known BRDF (*Method 2*), and radiative transfer models for clear sky conditions (*Method 3*), with and without independent measurements of aerosol and ozone optical thicknesses;
2. Determine uncertainties between the different *Methods 1, 2 and 3* for measuring $R_{\mathrm{RS}}\left(\lambda,\theta,\phi\in\Omega_{\mathrm{FOV}};\theta_{\mathrm{o}}\right)$;
3. Determine uncertainties between NRSR values determined from above- and in-water radiance measurements; and
4. Evaluate uncertainties between NRSR measured, either above- or in-water, NRSR modeled from measured inherent optical properties (IOP), and NRSR modeled based on IOP estimated from phytoplankton pigments (*e.g.* chlorophyll a) and other optically important constituents of the water column.

The workshop participants recommended the following priorities, guidelines and constraints for this research:

1. Preceding any intercomparisons of measured $R_{\mathrm{RS}}\left(\lambda,\theta,\phi\in\Omega_{\mathrm{FOV}};\theta_{\mathrm{o}}\right)$, all measurements must be *normalized* to account for the influence of the solar zenith angle and the ocean's BRDF, following the methods of Morel and Gentili (1996). This applies both to in-water and above-water methods.
2. Initial intercomparisons should be limited to wavelengths $\lambda < 600$ nm, relatively clear waters where $K_{\mathrm{d}}(490) < 0.1\ \mathrm{m}^{-1}$, cloud cover < 20 %, wind speeds $U < 10\ \mathrm{m\ s}^{-1}$, and solar zenith angles in the range $30^{\mathrm{o}} < \phi_{\mathrm{o}} < 60^{\mathrm{o}}$. In these limited circumstances, an uncertainty of approximately 5 % may be assumed for NRSR determined from in-water profile measurements of upwelled radiance, an estimate based on results of profile analyses (Siegel *et al*. 1995) and radiometric calibration uncertainties (Mueller *et al*. 1996; Johnson *et al*. 1996).

[3] The concept of "normalized remote-sensing reflectance" (NRSR) is extended here and in Volume III, Chapter 4 to "exact normalized remote-sensing reflectance" as defined in Equation (3.6), with reference to Volume III, Chapter 4 (J. Mueller, 2001, 2002).

Finally, the workshop participants agreed that a viewing zenith angle of $\theta = 40^{o}$, rather than the then more widely used $\theta = 30^{o}$, should be routinely used for above-water measurements of $R_{\mathrm{RS}}\left(\lambda,\theta,\phi \in \Omega_{\mathrm{FOV}};\theta_{\mathrm{o}}\right)$ without a polarizer.

Hooker *et al*. (1999) and Hooker and Lazin (2000) report experimental intercomparisons, and results of preliminary analyses, which closely follow the above guidelines. The measurement intercomparisons reported by Toole *et al* (2000) and Fougnie *et al*. (1999) were made in turbid, to very turbid, coastal water masses, which contributes to the large uncertainties (10 %-15 % for in-water and 20 %-40 % for above-water remote sensing reflectances) they reported. Neither of the latter comparisons was made using normalized reflectances, and the polarized reflectances measured by Fougnie *et al*. (1999) are not directly comparable to reflectances determined from unpolarized in-water radiance measurements.

There is currently insufficient information on which to conclusively recommend any preference between *Methods 1, 2 or 3* for making above-water measurements of $R_{\mathrm{RS}}\left(\lambda,\theta,\phi \in \Omega_{\mathrm{FOV}};\theta_{\mathrm{o}}\right)$.

For *Method 3*, or any polarized version of either of the other 2 methods, research is needed to establish and validate a robust relationship between vertically polarized $R_{RSv}\left(\lambda,0,0 \in \Omega_{FOV};\theta_{o}\right)$ determined from the above-water measurements and total $R_{\mathrm{RS}}^{\mathrm{ex}}\left(\lambda\right)$ determined from total radiance measurements. Since the water body polarizes incident sunlight, polarized measurements of water-leaving radiance must be corrected to estimate total radiance. For 150°-160°, the effect is small (typically 10 %), and can be corrected to within a few percent (Fougnie *et al*., 1999). Indeed, a method must be developed to determine a polarized equivalent to $R_{\mathrm{RS}}^{\mathrm{ex}}\left(\lambda\right)$.

Again, normalization consists of adjustments from the measured viewing and solar geometry to radiance emitted in the zenith direction with the sun at zenith and adjusted to remove atmospheric effects (Morel and Gentili 1996; Volume III, Chapter 4). Methods for calculating $R_{\mathrm{RS}}^{\mathrm{ex}}\left(\lambda\right)$ from measurements of total $R_{\mathrm{RS}}\left(\lambda,\theta,\phi \in \Omega_{\mathrm{FOV}};\theta_{\mathrm{o}}\right)$ are given in Volume III, Chapter 4. The present version of the Ocean Optics Protocols does not provide methods for determining $R_{\mathrm{RS}}^{\mathrm{ex}}\left(\lambda\right)$ from polarized radiance measurements.

It is further recommended, tentatively, that total surface and sky radiances should be measured at $(\theta, \phi) = (\theta_{\mathrm{sky}}, \phi_{\mathrm{sky}}) = (40^{o}, 135^{o})$[4] (Fougnie *et al*. 1999; Mobley 1999). Unpolarized surface reflectance for skylight (*i.e.*, polarized plus unpolarized components) ρ should be estimated as a function of wind-speed following the method of Mobley (1999: Fig. 9), and for completely overcast skies use $\rho \approx 0.028$.

REFERENCES

Austin, R.W., 1974: Inherent spectral radiance signatures of the ocean surface. In: S.Q. Duntley, R.W. Austin, W.H. Wilson, C.F. Edgerton, and S.W. Moran, *Ocean Color Analysis*, SIO Ref. 74-10, Scripps Institution of Oceanography, La Jolla, CA.

Carder, K.L. and R.G. Steward, 1985: A remote-sensing reflectance model of a red tide dinoflagellate off West Florida. *Limnol. Oceanogr.* **30**: 286-298.

Carder, K.L., P. Reinersman, R.F. Chen, F. Muller-Karger, C.O. Davis and M. Hamilton, 1993: AVIRIS calibration and application in coastal oceanic environments. *Remote Sens. Environ.* **44**: 205-216.

Cox, C. and W. Munk, 1954: Measurement of the roughness of the sea surface from photographs of the sun's glitter. *J. Opt. Soc. Am*. **44**: 11838-11850.

Fougnie, B., R. Frouin, P. Lecomte and Pierre-Yves Deschamps, 1999: Reduction of skylight reflection effects in the above-water measurement of diffuse marine reflectance. *Appl. Opt*. **38**: 3844-3856.

Gould, R.A., R.A. Arnone and M. Sydor, 2000: Improved techniques for determining remote sensing reflectance in coastal waters, *Appl. Opt.* (In press).

[4] This proposed choice of viewing geometry is not universally accepted within the community (see additional comments in Volume III, Chapter 1, Section 1.3). (J. Mueller, 2002).

Hooker, S.B. and G.Lazin, 2000: *The SeaBOARR-99 Field Campaign*. NASA Tech. Memo. 206892, Vol. **8**, S.B. Hooker and E.R. Firestone, eds., NASA Goddard Space Flight Center, Greenbelt, MD. 46pp.

Hooker, S.B., G. Zibordi, G.Lazin, and S. McLean, 1999: *The SeaBOARR-98 Field Campaign*. NASA Tech. Memo. 206892, Vol. **3**, S.B. Hooker and E.R. Firestone, eds., NASA Goddard Space Flight Center, Greenbelt, MD. 40pp.

Johnson, B.C., S.S. Bruce, E.A. Early, J.M. Houston, T.R. O'Brian, A. Thompson, S.B. Hooker and J.L. Mueller, 1996: The Fourth SeaWiFS Intercalibration Round-Robin Experiment (SIRREX-4), May 1995. *NASA Tech. Memo. 104566, Vol. **37**,* S.B. Hooker, E.R. Firestone and J.G. Acker, Eds., NASA Goddard Space Flight Center, Greenbelt, Maryland, 65 pp.

Lee, Z.P., K.L. Carder, T.G. Peacock, C.O. Davis and J.L. Mueller, 1997a: Remote-sensing reflectance and inherent optical properties of oceanic waters derived from above-water measurements. In: *Ocean Optics XIII*, S.G. Ackleson, ed., Proc. SPIE **2693**: 160-166.

Lee, Z.P., K.L. Carder, T.G. Peacock, and R.G. Steward, 1997b: Remote sensing reflectance measured with and without a vertical polarizer. In: *Ocean Optics XIII*, S.G. Ackleson, ed., Proc. SPIE **2693**: 483-488.

Mobley, C.D., 1999: Estimation of the remote-sensing reflectance from above-surface measurements. *Appl. Opt*. **38**: 7442-7455.

Morel, A., and B. Gentili, 1996: Diffuse reflectance of oceanic waters. III. Implication of bidirectionality for the remote-sensing problem. *Appl. Opt*. **35**: 4850-4862.

Mueller, J.L., B.C. Johnson, C.L. Cromer, S.B. Hooker, J.T. McLean and S.F. Biggar, 1996: The Third SeaWiFS Intercalibration Round-Robin Experiment (SIRREX-3), 19-30 September 1994: *NASA Tech. Memo. 104566, Vol. **34**,* S.B. Hooker, E.R. Firestone and J.G. Acker, Eds., NASA Goddard Space Flight Center, Greenbelt, Maryland, 78 pp.

Mueller, J.L., and R.W. Austin, 1995: Ocean Optics Protocols for SeaWiFS Validation, Revision 1. *NASA Tech. Memo. 104566, Vol. **25**,* S.B. Hooker, E.R. Firestone and J.G. Acker, Eds., NASA Goddard Space Flight Center, Greenbelt, Maryland, 67 pp.

Mueller, J.L., J.R.V. Zaneveld, S. Pegau, E. Valdez, H. Maske, S. Alvararez-Borrego and R. Lara-Lara, 1997: Remote sensing reflectance: preliminary comparisons between in-water and above-water measurements, and estimates modeled from measured inherent optical properties, In: *Ocean Optics XIII*, S.G. Ackleson, ed., Proc. SPIE **2693**: 502-507.

Rhea, W.J. and C.O. Davis, 1997: A comparison of the SeaWiFS chlorophyll and CZCS pigment algorithms using optical data from the 1992 JGOFS Equatorial Pacific Time Series. *Deep Sea Res. II* **44**: 1907-1925.

Siegel, D.A., M.C. O'Brien, J.C. Sorenson, D.A. Konnoff, E.A. Brody, J.L. Mueller, C.O. Davis, W.J. Rhea, and S.B. Hooker, 1995: Results of the SeaWiFS Data Analysis Round Robin, July 1994 (DARR-94): *NASA Tech. Memo. 104566, Vol. 26,* S.B. Hooker and E.R. Firestone, Eds., NASA Goddard Space Flight Center, Greenbelt, Maryland, pp 44-48.

Sydor, M. and R.A. Arnone, 1997: Effect of suspended and dissolved organic matter on remote-sensing of coastal and riverine waters. *Appl. Opt*. **36**: 6905-6912.

Sydor, M., R.A. Arnone, R.W. Gould, Jr., G.E. Terrie, S.D. Ladner and C.G. Wood, 1998: Remote-sensing technique for determination of the volume absorption coefficient of turbid water. *Appl. Opt*. **37**: 4944-4950.

Toole, D.A., D.A. Siegel, D.W. Menzies, M.J. Neumann and R.C. Smith, 2000: Remote-sensing reflectance determinations in the coastal ocean environment: impact of instrumental characteristics and environmental variability. *Appl. Opt*. **39**: 456-468.

Chapter 4

Normalized Water-Leaving Radiance and Remote Sensing Reflectance: Bidirectional Reflectance and Other Factors

Andre Morel[1] and James L. Mueller[2]

[1]*Laboratoire d'Oceanographie, Universite Pierre et Marie Curie, Villefranche-sur-Mer, France*
[2]*Center for Hydro-Optics and Remote Sensing, San Diego State University, California*

4.1 NOTATIONS AND FUNDAMENTAL DEFINITIONS

Most of the variables involved in the remote sensing of the ocean color are based on, or derived from, the basic radiometric quantity often called ***water-leaving radiance***; this quantity, commonly denoted $L_W(\lambda)$, is the radiance which emerges from the ocean, determined just above the water-air interface at a level conventionally denoted 0^+. The $L_W(0^+,\lambda)$ radiance field (its angular dependency will be explicitly given below) originates from the in-water upward radiance field, $L_u(0^-,\lambda)$, determined just beneath the interface at a level denoted 0^-. Since $L_W(\lambda)$ is defined only at the upper side of the interface, the explicit notation 0^+ will be omitted. Two other radiance fields are also involved, namely the downward radiance fields, just above the surface, $L_d(0^+,\lambda)$, and just beneath the surface, $L_d(0^-,\lambda)$. The reflection and refraction processes govern the transfer through the interface of the corresponding fields, namely the transformation of $L_u(0^-,\lambda)$ into $L_W(\lambda)$, and that of $L_d(0^+,\lambda)$ into $L_d^t(0^-,\lambda)$, the transmitted component of the total downward radiance distribution[5] $L_d(0^-,\lambda)$.

The angular dependencies are introduced by using two couples of angles, (θ, ϕ) and (θ', ϕ) (Figure 4.1); ϕ is the azimuth angle [0, 2π], θ is the zenith angle for above-water radiances [0, π/2], and θ' the nadir angle for the in-water (upward) directions [0, π/2]. If Ξ_d represents the upper hemisphere (2π sr), containing all downward directions), Ξ_u represents the lower hemisphere (containing the upward directions), and $d\omega = \sin\theta d\theta d\phi$ is the differential element of solid angle, the following integrals of the radiance fields

$$E_d(0^+,\lambda) \equiv \int_{\Xi_d} L_d(0^+,\lambda,\theta,\phi)\cos\theta d\omega, \tag{4.1}$$

$$E_d(0^-,\lambda) \equiv \int_{\Xi_d} L_d(0^-,\lambda,\theta',\phi)\cos\theta' d\omega', \tag{4.2}$$

$$E_u(0^-,\lambda) \equiv \int_{\Xi_d} L_u(0^-,\lambda,\theta',\phi)\cos\theta' d\omega, \text{ and} \tag{4.3}$$

$$E_u(0^+,\lambda) \equiv \int_{\Xi_d} L_u(0^+,\lambda,\theta,\phi)\cos\theta d\omega, \ \mu\text{W cm}^{-2}\text{nm}^{-1}, \tag{4.4}$$

and

$$E_u(0^+,\lambda) \equiv \int_{\Xi_d} L_u(0^+,\lambda,\theta,\phi)\cos\theta d\omega, \ \mu\text{W cm}^{-2}\text{nm}^{-1}, \tag{4.5}$$

[5] The radiance distributions emanating downward from the underside of the air-sea interface, and upward from its upper side, are each the sum of radiances transmitted through and reflected from the interface. In other words, $L_d(0^-,\lambda) = L_d^t(0^-,\lambda) + \rho L_u(0^-,\lambda)$ and $L_u(0^+,\lambda) = L_W(\lambda) + \rho L_d(0^+,\lambda)$, where ρ is the Fresnel reflectance of the interface. The reflected components of these radiance distributions will not be examined here as vector fields.

are the ***downwelling irradiances*** above or below the surface, $E_d(0^+, \lambda)$ and $E_d(0^-, \lambda)$, and the ***upwelling irradiances*** below and above the surface, $E_u(0^-, \lambda)$ and $E_u(0^+, \lambda)$, respectively. The irradiance ratio, or ***irradiance reflectance***, is defined immediately below the surface as

$$R\left(0^-,\lambda\right) \equiv \frac{E_u\left(0^-,\lambda\right)}{E_d\left(0^-,\lambda\right)}. \tag{4.5}$$

Note that the corresponding quantity above the surface, $R\left(0^+,\lambda\right)$, is not in common use.

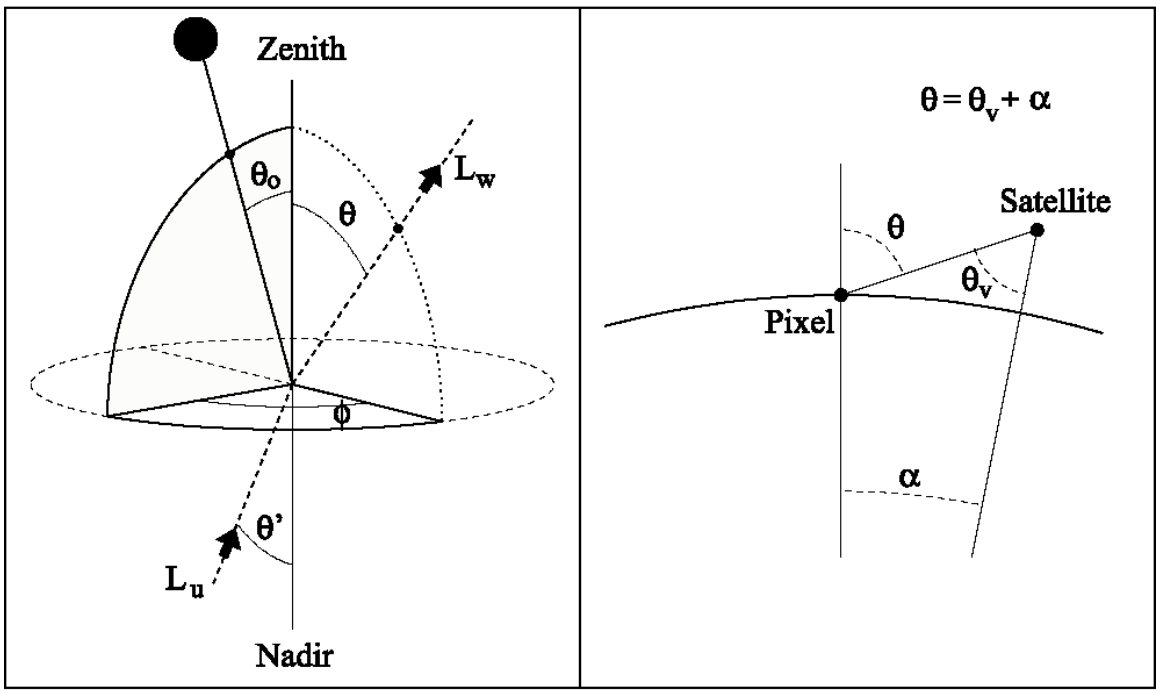

Figure 4.1: Schematic views of the geometry and symbols used in this chapter. The polar angles that specify the radiances correspond to the direction of photon travel and are measured from the local zenith for water-leaving radiance (θ') and zenith sun angle (θ_o), or from nadir when dealing with the in-water upwelling radiance (θ'). The azimuth angle ϕ is 0 and π for the sun and the antisolar directions, respectively. The viewing direction, denoted θ_v, is the direction the satellite is pointed to aim at the pixel, and is always smaller than θ.

From Equation (4.3), another quantity, ***Q***, can be defined as

$$Q\left(0^-,\lambda,\theta',\phi\right) \equiv \frac{E_u\left(0^-,\lambda\right)}{L_u\left(0^-,\lambda,\theta',\phi\right)}, \text{ sr}, \tag{4.6}$$

It can be noticed that if the $L_u\left(0^-,\lambda,\theta',\phi\right)$ field was isotropic, or in other words, if $L_u\left(0^-,\lambda\right)$ was constant whatever the angles θ'and ϕ, *Q* would take the particular value π. The argument 0^- will hereafter be abandoned, as the *Q* quantity is always defined for the in-water radiant field at the interface.

All the above relationships, (4.1) to (4.6), describe the radiance vector fields and are purely of geometrical nature. Physical processes will be briefly examined, first at the interface (Section 4.2), and then inside the water body (Section 4.3).

In addition to the above general definitions, several derived quantities are specifically used in ocean color science, in particular the two following ones:

The ***remote sensing reflectance*** is defined as

$$R_{\mathrm{RS}}(\lambda,\theta,\phi)=\frac{L_{\mathrm{w}}(\lambda,\theta,\phi)}{E_{\mathrm{d}}(0^{+},\lambda)},\ \mathrm{sr}^{-1}. \tag{4.7}$$

In general (*i.e.*, if not otherwise stated), the water-leaving radiance considered in Equation (4.7) is the vertically upward radiance originating from nadir, and traveling toward zenith ($\theta = 0$); its accurate writing is thus $L_{\mathrm{w}}(\lambda,0,0)$, when this quantity has to be distinguished from other slant radiances (actually ϕ is undetermined, not 0).

The other quantity is the ***normalized water-leaving radiance***, $L_{\mathrm{WN}}(\lambda,\theta,\phi)$ {sometimes denoted nL_{W}, or [L_{W}]n, in references cited below}, originally introduced by Gordon and Clark (1981). The underlying rationale was to produce, from measured $L_{\mathrm{W}}(\lambda,\theta,\phi)$ values, normalized quantities that are comparable; with this aim, these quantities must be independent from the measurement conditions, which are determined by the actual solar zenith angle and atmospheric transmittance. These environmental influences can be removed by forming the following quantity

$$L_{\mathrm{WN}}(\lambda,\theta,\phi)=\frac{L_{\mathrm{W}}(\lambda,\theta,\phi)}{E_{\mathrm{d}}(0^{+},\lambda)}\bar{F}_{\mathrm{o}}(\lambda)=R_{RS}(\lambda,\theta,\phi)\bar{F}_{\mathrm{o}}(\lambda),\ \mu\mathrm{W\ cm^{-2}nm^{-1}sr^{-1}}, \tag{4.8}$$

where the measured radiance is divided by the actual irradiance at the sea level and then multiplied by the solar irradiance at the top of the atmosphere, $\bar{F}_{\mathrm{o}}(\lambda)$, at the mean sun-earth distance (d_o). The same quantity can be interpreted in another way: the normalized leaving radiance is the radiance which would be measured, if the sun were at zenith, in absence of atmosphere, and when the earth is at its mean distance from the sun. In spite of this interpretation, the normalized water-leaving radiance is still a quantity depending on θ and ϕ, as far as the initial measurement of the quantity $L_{\mathrm{W}}(\lambda,\theta,\phi)$ has been performed under these specific angular conditions.

4.2 PHYSICAL PHENOMENA AT THE INTERFACE

Because the refractive indices n of the two media differ, ($n \cong 1$ for air and $n \cong 1.34$ for sea water), the processes of reflection and refraction occur at the interface and modify the radiance fields transmitted from one medium to the other. If the interface is perfectly level, Fresnel's law applies for water-incident or air-incident rays; if the interface is wavy, the same law applies for each facet, and the numerical computations are less simple. The incident and refracted directions, θ and θ' respectively (Figure 1), obey the Snell's law, with $\theta'=\sin^{-1}\left(\frac{\sin\theta}{n}\right)$, where n is the refractive index of water. Another consequence of this law is the so-called n^2 law for radiance, which expresses the conservation of flux along a path through media with various indices (apart from the Fresnel transmittance effect, if physical boundaries between media exist).

Coming back to the propagation of the $L_{\mathrm{d}}(0^{+},\lambda,\theta,\phi)$ field through the interface, the correspondence between the above- and in-water transmitted radiances is expressed as

$$L_{\mathrm{d}}^{\mathrm{t}}(0^{-},\lambda,\theta',\phi)=L_{\mathrm{d}}(0^{+},\lambda,\theta,\phi)\left[1-\rho(\theta,\theta')\right]n^{2},\ \mu\mathrm{W\ cm^{-2}nm^{-1}sr^{-1}}, \tag{4.9}$$

where $\rho(\theta, \theta')$ is the Fresnel reflectance for the associated directions θ and θ', and thus the bracket represents the transmittance. For the upward fields, the reciprocal relationship is written

$$L_{\mathrm{W}}(\lambda,\theta,\phi)=L_{\mathrm{u}}(0^{-},\lambda,\theta',\phi)\frac{\left[1-\rho(\theta',\theta)\right]}{n^{2}},\ \mu\mathrm{W\ cm^{-2}nm^{-1}sr^{-1}}. \tag{4.10}$$

Note that $\rho(\theta,\theta') = \rho(\theta',\theta)$, so that the reflectances are independent from the direction of propagation. Note also that $\rho(\theta',\theta) \equiv 1$ when θ' exceeds the critical angle, $\theta'_c \cong 48°$ for $n = 1.34$.

The upwelling irradiance $E_u^t(0^+,\lambda)$ transmitted through the air-sea interface is obtained by integrating Equation (4.10) for a quasi-isotropic upwelling radiance distribution within the cone limited by θ'_c, yielding the approximate expression $E_u^t(0^+,\lambda) \cong 0.52 E_u(0^-,\lambda)$, which means that about half of the in-water upward flux incident upon a horizontal surface is able to emerge. In corollary, about half of this flux is returned back, and thence is added to the downward flux. This last remark explains why integrating Equation (4.9) does not provide straightforwardly the in-water downward irradiance, which can be approximately expressed through

$$E_d(0^-,\lambda) \cong E_d(0^+,\lambda)\frac{1-\overline{\rho}}{1-\overline{r}R(0^-,\lambda)}. \tag{4.11}$$

The existence of the reflected downward flux is accounted for by the denominator. $\left[1-\overline{r}R(0^-,\lambda)\right]$, which combines the irradiance reflectance with $\overline{r}$ the mean (water-air) Fresnel reflectance for the whole diffuse upward flux (about 0.48). Similarly, the term $\overline{\rho}$ stands for the (air-water) Fresnel reflectance at the interface that applies to the whole downward irradiance from the sun and the sky. This mean reflectance $\overline{\rho}$ typically amounts to 4 % to 6 %, but may deviate from these values according to the sky state and the sea state. The approximate character of Equation (4.11) originates from these two mean reflectances, $\overline{r}$ and $\overline{\rho}$.

The first determinant of the $L_d(0^+,\lambda,\theta,\phi)$ distribution, in a cloudless atmosphere, is the sun position, described by the solar zenith angle θ_o. The diffuse sky radiance also contributes to the formation of $L_d(0^+,\lambda,\theta,\phi)$, and the proportions of the direct solar flux and the diffuse sky radiation actually vary, not only with θ_o and wavelength λ, but also with the varying content in aerosol. This aerosol load is conveniently described by its optical thickness, τ_a at a selected reference wavelength, often 550 nm. Finally, a more accurate writing (still incomplete, as, for instance, the aerosol nature is also involved) for this downward field is $L_d(0^+,\lambda,\theta,\phi,\theta_o,\tau_a)$.

Below the interface, the same dependences (with respect to λ, θ_o, and τ_a) are maintained, but in addition, the transmittance through the interface may be modified because of the presence of capillary and gravity waves. To the extent that these waves, and especially their slopes, can be related to the wind speed, *W*, this new argument must be considered; finally, to account for all these factors, the in-water transmitted downward radiance field must be written $L_d^t(0^-,\lambda,\theta',\phi,\theta_o,\tau_a,W)$.

4.3 THE IN-WATER RADIANT FIELD: PHYSICAL CONSIDERATIONS

The upward radiance field $L_u(z,\lambda,\theta',\phi)$ at a depth z (including z = 0^-) is an *apparent optical property*, (AOP, *sensu* Preisendorfer 1960), and as such depends both on the *inherent optical properties* (IOP) of the water, and on the way this water body is illuminated.

In absence of reflecting bottom, the illumination conditions are those prevailing just beneath the surface. Therefore, for a given water mass, *i.e.* for a given set of IOP, the $L_u(0^-,\lambda,\theta',\phi)$ field is strongly dependent on the downward radiance field $L_d^t(0^-,\lambda,\theta',\phi,\theta_o,\tau_a,W)$, at least for the upper layers[6]. Moreover, for given boundary conditions, expressed by the $L_d^t(0^-,\lambda,\theta',\phi,\theta_o,\tau_a,W)$ vector field, the resulting $L_u(0^-,\lambda,\theta',\phi)$ field will depend on the IOP, not only for its magnitude, but also for its geometrical structure. The structure of the $L_u(0^-,\lambda,\theta',\phi)$ vector

[6] In the deep asymptotic regime the dependence on the $L_d^t(0^-,\lambda,\theta',\phi,\theta_o,\tau_a,W)$ vector field vanishes, and the $L_u(z,\lambda,\theta',\phi)$ field progressively takes the character of an IOP.

field in the principal plane of the sun ($\phi = 0$ or π) is illustrated schematically in Figure 4.2, where any radial distance from the origin to the upwelling radiance contour indicates the magnitude of radiance in that direction.

The magnitude of the upward flux is intuitively related to the antagonistic processes of backscattering, which allows downwelling photons to travel backward, and of absorption, which annihilates photons and so cancels their chance of being backscattered. The corresponding IOP quantifying these two opposite processes are the backscattering coefficient[7], $b_b(z,\lambda)$, and the absorption coefficient, $a(z,\lambda)$, or if for simplicity, we consider a vertically homogeneous medium, $b_b(\lambda)$ and $a(\lambda)$. Therefore, the irradiance reflectance $R(0^-,\lambda)$, as defined in Equation (4.5), must in some way, be related to the ratio of the above coefficients, $\frac{b_b(\lambda)}{a(\lambda)}$, or $\frac{b_b(\lambda)}{a(\lambda)+b_b(\lambda)}$. Note that even though irradiance reflectance is a finite quantity constrained to $R(0^-,\lambda) \le 1$, the first ratio is *a priori* unbounded, whereas the second ratio lies within the interval [0,1] when $b_b(\lambda)$ becomes much larger than $a(\lambda)$. By assuming that $b_b(\lambda)$ is small compared to $a(\lambda)$, the irradiance reflectance can be expressed as

$$R(0^-,\lambda) = f(\lambda)\frac{b_b(\lambda)}{a(\lambda)}, \tag{4.12a}$$

and more conveniently, particularly when b_b is not small compared to a, through

$$R(0^-,\lambda) = f'(\lambda)\frac{b_b(\lambda)}{a(\lambda)+b_b(\lambda)} \tag{4.12b}$$

with a straightforward relationship between the two factors

$$f'(\lambda) = f(\lambda)\left[1+\frac{b_b(\lambda)}{a(\lambda)}\right]. \tag{4.12c}$$

Like $R(0^-,\lambda)$, f' tends toward unity for extremely high $\frac{b_b(\lambda)}{a(\lambda)}$ values, whereas f tends toward 0. These factors, f or f', actually rule the magnitude of the irradiance reflectance and relate this global reflectance to the IOP.

The influence of the IOP on the geometrical structure of the upward light field, and therefore on the $Q(\lambda,\theta',\phi)$ factor, is slightly more complex, but can be, at least qualitatively, predicted. The shape of the volume scattering function (VSF) of seawater is obviously involved. The VSF, $\beta(\lambda,\Psi)$, of any water body is the sum of the VSF due to water molecules, $\beta_w(\lambda,\Psi)$, and the VSF due to the various particles in suspension, $\beta_p(\lambda,\Psi)$. The former is symmetrical and not far from being spherical, whereas the latter is strongly elongated in the forward direction, and exhibits a weak minimum around $\psi = 140°$. Therefore, the shape of the resulting VSF is determined by the relative proportions of the two components, conveniently expressed by the parameter

$$\eta = \frac{b_w(\lambda)}{b(\lambda)}, \tag{4.13}$$

[7] Recall that any scattering coefficient, $b_x(\lambda)$ is related to the corresponding volume scattering function (a basic IOP), denoted $\beta_x(\lambda,\psi)$, through

$$b_x(\lambda) = 2\pi\int_0^{\pi}\beta_x(\lambda,\Psi)\sin\Psi d\Psi,$$

where ψ is the scattering angle. The backscattering coefficient $b_{bx}(\lambda)$, is obtained when the above integral extends only over the interval $\pi/2$ to π.

namely the ratio of molecular scattering, $b_w(\lambda)$, to the total scattering coefficient $b(\lambda) = b_w(\lambda) + b_p(\lambda)$, where $b_p(\lambda)$ represents the scattering coefficient due only to the suspended particles. A ratio similar to η, but involving only the backscattering coefficients, is also useful; it is expressed as

$$\eta_b = \frac{b_{bw}(\lambda)}{b_b(\lambda)}, \tag{4.14}$$

where the backscattering coefficient $b_b(\lambda) = b_{bw}(\lambda) + b_{bp}(\lambda)$ is the sum of the backscattering coefficients for molecules and particles, respectively.

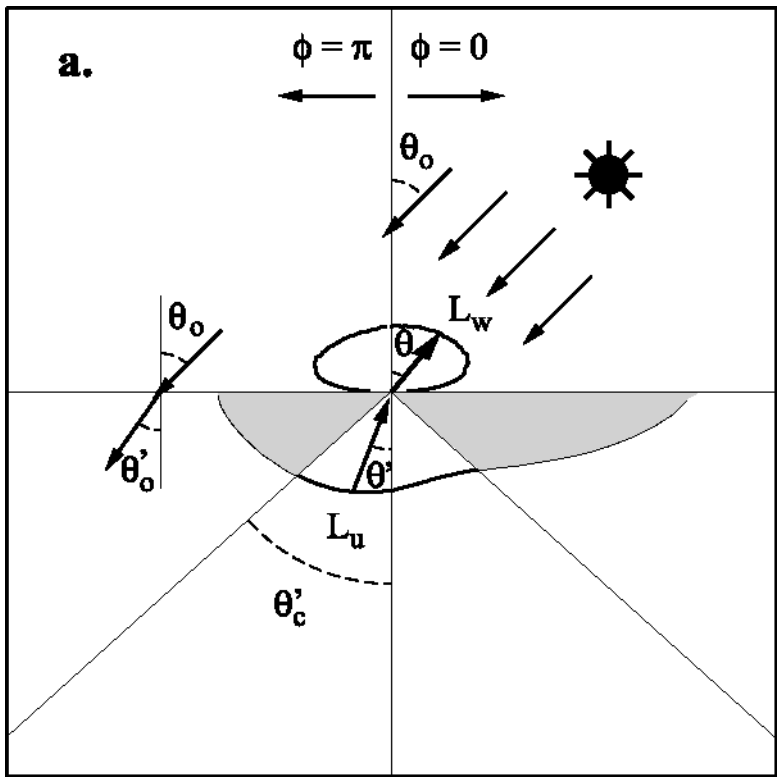

Figure 4.2: Conventional representation of the upward radiance field, $L_u(0^-, \lambda, \theta', \phi)$ in the vertical plane containing the sun, *i.e.* the *solar principal plane*. The polar diagram represents in-water radiances as vectors, the length of which corresponds to magnitude, ending at the center. The shaded area, limited by the critical angle θ_c', contains those radiances that do not emerge, but are totally and internally reflected. The corresponding water-leaving radiance field $L_W(\lambda, \theta, \phi)$ is also represented (by definition at z = 0^+).

The diffuse upward radiant field is built up by photons that have been scattered at least once, and may have experienced several, and even many scattering events before being redirected toward the atmosphere. It is conceivable that if single scattering prevails, the upward radiant field is governed by, and thus is similar in shape to, the backward lobe of the VSF. Conversely, in a multiple scattering regime, the highly diffuse light field tends to become isotropic. The more or less diffuse character of the upward radiant field actually depends on the average number, $\tilde{n}$, of scattering events the photons have undergone before reaching the interface (z = 0^-). This number is simply related to the IOP through (Morel and Gentili, 1991)

$$\tilde{n}(\lambda) = \left[1 - \varpi(\lambda)\right]^{-1}, \tag{4.15}$$

where $\varpi(\lambda) \equiv \dfrac{b(\lambda)}{a(\lambda)+b(\lambda)}$ is the ***single scattering albedo***. It is straightforward to show that (4.15) may alternatively be written $\tilde{n}(\lambda) = 1 + \dfrac{b(\lambda)}{a(\lambda)}$, or $\tilde{n}(\lambda) = \dfrac{a(\lambda)+b(\lambda)}{a(\lambda)}$.

Therefore, in a strongly scattering medium ϖ is close to 1, $\tilde{n}$ is extremely high, multiple scattering of high orders is the common rule, and finally the radiance distribution tends to be isotropic. Conversely, in a strongly absorbing medium, ϖ is small, $\tilde{n}$ is not much above 1, single scattering dominates over higher orders, and the radiance pattern tends to mimic that of the VSF (single scattering). In such a case, if molecular scattering dominates (η large, and η_b tending toward 1), the shape of the VSF is more or less symmetrical and the radiance field is accordingly rather round-shaped, but if particle scattering dominates (η small, and η_b tending toward 0), the shape of the VSF is extremely elongated in the forward direction and the radiance field is more structured. Figure 4.3 illustrates hypothetical examples of the upward radiant field and its bidirectional character, for optically pure water (no particles), or for marine particles alone (without water); the average number of scattering events is either 2, or 61, and the sun is at zenith, or 60° away from zenith. The conventions in the polar plots of Figure 4.3 are the same as in Figure 4.2.

Fluorescence and Raman Scattering

In all that has been said before, the only physical processes considered were absorption and scattering. In other words the medium was considered as purely passive. Other phenomena occur, when the medium contains *sources*, which in seawater are mainly fluorescence emission and Raman scattering.

Fluorescence emission creates light at certain wavelengths, typical of the substance responsible for the emission. For instance, Chlorophyll *a* (borne by algal cells) fluoresces around 683 nm with a bandwidth of about 25 nm, whereas the fluorescence emitted by colored dissolved organic matter (CDOM) is more complex and spectrally broader. Fluorescence may be excited by photons at any wavelength shorter than that of the emission, although the excitation efficiency may vary with wavelength (due largely to the absorption spectrum of the material in question). These emissions are obviously dependent on the concentration of the fluorescing substances.

The Raman (inelastic) scattering is characterized by a constant frequency shift between the excitation and emitted light, and the shift is only determined by the molecule structure of the medium (here water). This emission occurs throughout the visible spectrum, at wavelengths larger than those of the exciting light. Because it is a physical property of the water molecule, it is always present, even if its influence is hardly detected in the upper layers, where the elastic scattering process dominates the upward radiant field.

From the viewpoint of the directional properties of the upward field, these emissions, isotropic for fluorescence and quasi-isotropic for Raman scattering, add a component that is angularly constant and thus tends to smooth out the structures generated by elastic scattering (particularly by particle scattering). Note that the coefficients describing these emissions (the reverse of absorption) belong to the category of IOP (see also Volume II, Chapter 2, Section 2.4).

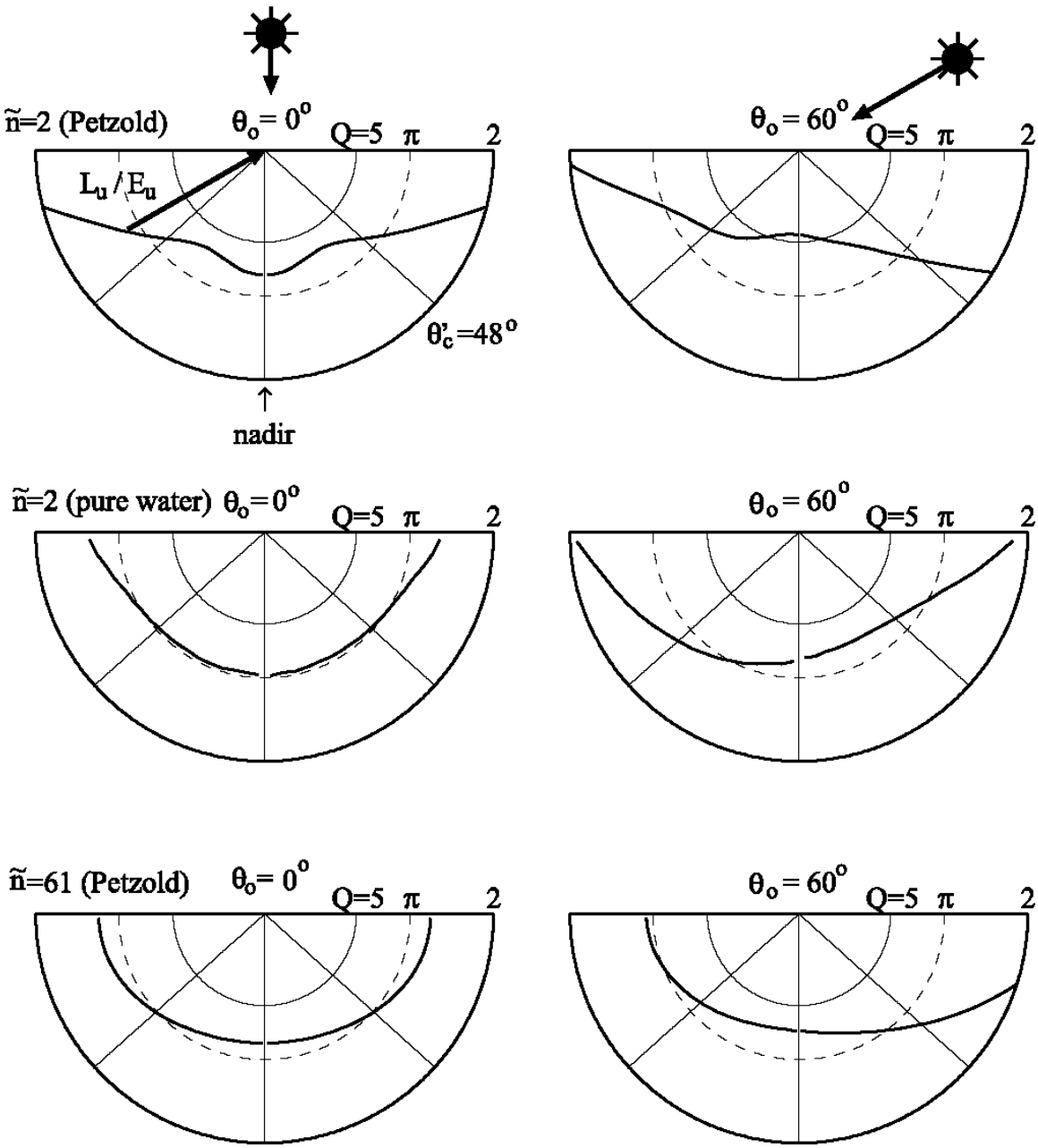

Figure 4.3: The above diagrams make use of the same form of representation and display as in Figure 4.2, but for the ratio $\left[L_u\left(0^-,\lambda,\theta',\phi\right)\div E_u\left(0^-,\lambda\right)\right]$, *i.e.* of $\left[Q\left(\lambda,\theta',\phi\right)\right]^{-1}$ [Equation (4.6)], not the radiance vector itself. When the sun is at zenith, ϕ is undetermined; when it is at θ_o = 60°, the half-plane containing the sun (ϕ = 0) is on the right side of the diagram. The first row is for a water mass where ñ = 2 (double scattering, on average), and the VSF is that of Petzold (1972). For the second row, ñ is again 2, and the particle VSF is replaced by the VSF for molecules. The third row represents the situation of an extremely turbid water mass, with ñ = 61 [*i.e.* $b\left(\lambda\right)=60a\left(\lambda\right)$] and the Petzold VSF.

4.4 PRACTICAL CONSIDERATIONS: THE f, Q AND ℜ FACTORS

Basic relationships

Only the processes and radiative properties of the near-surface layer are considered in what follows. In Equation (4.12a), or (4.12b), above, the *f*, or *f'*, factors are dimensionless quantities. It is worth emphasizing that they are not simply *coefficients*, but *functions*. Indeed, they are varying for two reasons. Inasmuch as the upward field is not isotropic, it is understandable that its angular structure will be sensitive to the directionality of the incident illumination. In simplified terms, for a given water body and given $a(\lambda)$ and $b(\lambda)$ values, *f* will be essentially dependent on the solar angle (and to a lesser extent on the sea state, and therefore, on *W*, the wind speed). In turn, for a given solar angle, the response of the medium, and thus the resulting *f* value will depend on the IOP, and on the VSF in particular. In total, *f* {or *f'*} is a function of two independent categories of variables, environmental and IOP, and thus must be expressed as $f\left[\lambda,(\theta_o,\tau_a,W),a(\lambda),\beta(\lambda,\Psi)\right]$ {or $f'\left[\lambda,(\theta_o,\tau_a,W),a(\lambda),\beta(\lambda,\Psi)\right]$}.

In its initial definition [Equation (4.6)], the geometrical quantity $Q(\lambda,\theta',\phi)$ was not related to the physical causes of its variations. These physical processes and variables giving rise to the geometric shape of the upward radiant field, and thus to the *Q* function, were shown in Section 4.3 to be determined by $L_d^t\left(0^-,\lambda,\theta',\phi,\theta_o,\tau_a,W\right)$, the VSF $\beta(\lambda,\Psi)$, and the average number of scattering events $\tilde{n}\left(\frac{b(\lambda)}{a(\lambda)}\right)$. To indicate the dependence of the *Q* function on these environmental variables and IOP, it is properly expressed as $Q\left[(\lambda,\theta',\phi),(\theta_o,\tau_a,W),a(\lambda),\beta(\lambda,\Psi)\right]$.

Radiative transfer computations, or measurements, give access to $f\left[\lambda,(\theta_o,\tau_a,W),a(\lambda),\beta(\lambda,\Psi)\right]$ and $Q\left[(\lambda,\theta',\phi),(\theta_o,\tau_a,W),a(\lambda),\beta(\lambda,\Psi)\right]$ functions, ultimately via their basic definitions, Equations (4.12) and (4.6) respectively. The generic formulations stand for a passive medium, deprived of internal sources[8]. They do not presume the relations that may exist between the IOP and the dissolved or particulate substances present in the water. In other words, the dependencies that they express are equally valid for Case 1 and Case 2 waters. For simplicity of presentation, the remainder of this chapter will consider only vertically homogeneous, Case 1 waters, in which a simplified representation of the *f* and *Q* functions is possible. Nevertheless, one need only revert to the above representations of *f* and *Q* functions, and add dependence on depth to the IOP, to restore full generality to the equations that follow

When dealing exclusively with Case 1 waters, the above formulations can be simplified. To the extent that in such waters, and at a given wavelength, it is (by definition) assumed that the IOP are universally related to the chlorophyll concentration (*Chl*) (Morel and Prieur 1977; Smith and Baker 1978), the functional dependencies in the previous expressions can be written as $f\left[\lambda,(\theta_o,\tau_a,W),Chl\right]$ $\left\{\text{or } f'\left[\lambda,(\theta_o,\tau_a,W),Chl\right]\right\}$ and $Q\left[(\lambda,\theta',\phi),(\theta_o,\tau_a,W),Chl\right]$. It must be underlined that the simplified expression, as well as any predictive computations, are possible if, not only $a(\lambda)$ and $b_p(\lambda)$ have been related to *Chl*, but also $\beta(\lambda,\Psi)$. This means that the VSF for particles $\beta_p(\lambda,\Psi)$ must be known. The most common approach is to make $b_p(\lambda)$ varying with *Chl*, and to keep constant the shape of the VSF, *e.g.* by assuming that the scattering phase function of particles, $\tilde{\beta}_p(\lambda,\Psi)\equiv\frac{\beta_p(\lambda,\Psi)}{b_p(\lambda)}$, is constant in shape. Other assumptions about this phase function are also possible (see below).

[8] Here, the sources are Raman or fluorescence emissions. The *f* and *Q* functions may, of course, be corrected to account for these sources in radiative transfer computations.

Expressing slant water-leaving radiances

All needed quantities are now set up, and their expressions include all the dependencies with respect to geometry (viewing and solar angles), as well as with respect to the IOP (actually via λ and *Chl*). It is, therefore, possible to express any slant water-leaving radiance as a function of all variables. The steps are as follows (in a simplified writing):

- $L_{\mathrm{W}}(\lambda,\theta,\phi)$ is derived from $L_{\mathrm{u}}(0^-,\lambda,\theta',\phi)$ via Equation (4.10).
- $L_{\mathrm{u}}(0^-,\lambda,\theta',\phi)$ is related to $E_{\mathrm{u}}(0^-,\lambda)$ and $Q[(\lambda,\theta',\phi),(\theta_{\mathrm{o}},\tau_{\mathrm{a}},W),Chl]$ by Equation (4.6).
- $E_{\mathrm{u}}(0^-,\lambda)$ is related to $E_{\mathrm{d}}(0^-,\lambda)$ and $R(0^-,\lambda)$ by Equation (4.5).
- $E_{\mathrm{d}}(0^-,\lambda)$ is expressed as a function of $E_{\mathrm{d}}(0^+,\lambda)$ via Equation (4.11).
- $R(0^-,\lambda)$ is related to the IOP and $f[\lambda,(\theta_{\mathrm{o}},\tau_a,W),Chl]$ by Equation (4.12a) {or $f'[\lambda,(\theta_{\mathrm{o}},\tau_a,W),Chl]$ and Equation (4.12b}.

These steps lead to the final result

$$L_{\mathrm{W}}(\lambda,\theta,\phi,\theta_{\mathrm{o}},\tau_{\mathrm{a}},Chl)=E_{\mathrm{d}}(0^+,\lambda,\theta_{\mathrm{o}},\tau_{\mathrm{a}})\Re(\theta',W)\frac{f(\lambda,\theta_{\mathrm{o}},\tau_{\mathrm{a}},Chl)}{Q(\lambda,\theta',\phi,\theta_{\mathrm{o}},\tau_{\mathrm{a}},Chl)}\frac{b_{\mathrm{b}}(\lambda,Chl)}{a(\lambda,Chl)}, \qquad (4.16)$$

where the factor $\Re(\theta',W)$ merges all the effects of reflection and refraction, entering from Equations (4.10) and (4.11), and is written

$$\Re(\theta',W)=\left[\frac{1-\overline{\rho}(\theta_{\mathrm{o}})}{1-\overline{r}R(0^-,\lambda,\theta_{\mathrm{o}},Chl)}\frac{1-\rho(\theta',\theta;W)}{n^2}\right]. \qquad (4.17)$$

Note that in principle $\Re(\theta',W)$ depends on *Chl* and λ through $R(0^-,\lambda,\theta_{\mathrm{o}},Chl)$, but not significantly, because the product $\overline{r}R(0^-,\lambda,\theta_{\mathrm{o}},Chl)$ is small ($R(0^-,\lambda,\theta_{\mathrm{o}},Chl)\le 0.1$ and $\overline{r}\cong 0.48$). Because of its direct dependence on the Fresnel reflectance $\rho(\theta',\theta;W)$, however, when $\theta\ge 30°$ $\Re(\theta',W)$ varies strongly with θ and wind speed *W*, which parameterizes sea state, (Figure 4.4). In contrast, for $\theta \lesssim 25°$, $\Re(\theta',W)$ is practically insensitive to wind speed and may be assumed to be a constant $\Re_{\mathrm{o}}=0.529$. Finally, the wind speed *W* dependence of the ratio $\frac{f(\lambda,\theta_{\mathrm{o}},\tau_{\mathrm{a}},W,Chl)}{Q(\lambda,\theta',\phi,\theta_{\mathrm{o}},\tau_{\mathrm{a}},W,Chl)}$ is very weak (Morel and Gentili 1996), and therefore, it is not explicitly indicated in Equation (4.16), or below in Equations (4.19) through (4.22).

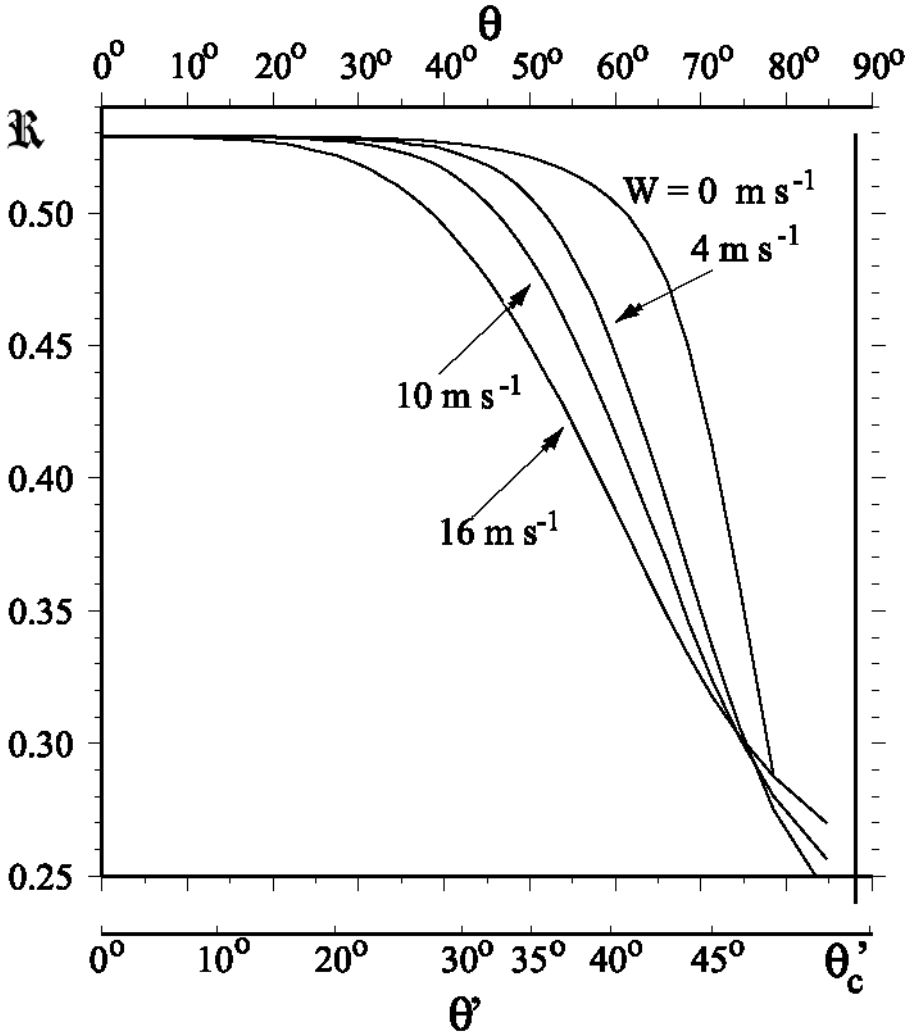

Figure 4.4: Evolution of the reflection-refraction term $\Re(\theta', W)$ [Equation (4.17)] as a function of θ and θ', for various wind speeds (W), and assuming a surface free of whitecaps. These results have been obtained through Monte-Carlo simulations, which combine the Gaussian distribution of capillary wave slopes (Cox and Munk 1954) and Fresnel's formula for reflectance at the sea surface.

4.5 IMPLICATIONS OF BIDIRECTIONALITY IN REMOTE SENSING

Two implications of bidirectionality for ocean color remote sensing are successively examined below. The first one is specifically related to ocean color radiance measurements made from a ***satellite-borne radiometer***. The second aspect is related to ***field*** measurements of radiances made at the sea level, usually in support of algorithm development, validation, and calibration of sensors aboard satellites in earth orbit.

The bidirectionality impacts the two quantities used in ocean color science, remote sensing reflectance $R_{RS}(\lambda,\theta,\phi)$ and normalized water-leaving radiance $L_{WN}(\lambda,\theta,\phi)$ as defined in Equations (4.7) and (4.8), respectively. To the extent that the emerging radiance field structure involves both the viewing geometry and the illumination geometry, neither of these quantities, which are both based on $L_W(\lambda,\theta,\phi,\theta_o,\tau_a,W,Chl)$, is fully normalized [cf. Equation (4.16)].

Satellite remotely sensed radiances

A remote sensor aims at the ocean under various angles, θ_v related to θ and θ' as illustrated in Figure 4.1, and generally captures slant radiances originating from the ocean (except for the sub-satellite pixel, where $\theta_v = \theta = \theta' = 0$). In general, the vertical plane containing the sun at zenith angle θ_o is separated by an azimuth angle ϕ from the vertical plane containing the sensor. The spectral water-leaving radiance that is determined by removing the atmospheric effects from the radiance measured by the satellite sensor may be written $L_W^S\left[\lambda,(\theta,\phi)\in\Omega_{FOV},\theta_o,\tau_a,W,Chl\right]$, where the superscript S stands for "Satellite" and Ω_{FOV} represents the solid angle of the sensor centered on the direction (θ,ϕ). For a given instrument Ω_{FOV} is constant, and this argument will no longer be repeated. It is also assumed that the above marine signal has been properly extracted from the total signal recorded by the satellite borne sensor, which implies that the atmospheric correction has been "perfectly" effected. Therefore the corrected water-leaving radiance measured by the sensor, is represented by Equation (4.16), and if it is divided by $E_d(0^+,\lambda)$, it provides the remote sensing reflectance $R_{RS}^S(\lambda,\theta,\phi)$ as defined by Equation (4.7). When $R_{RS}^S(\lambda,\theta,\phi)$ is multiplied by $\overline{F}_o(\lambda)$, it provides the normalized water-leaving radiance $L_{WN}^S(\lambda,\theta,\phi)$ conforming to the Gordon and Clark (1981) definition of Equation (4.8), which may also be expressed in the form

$$L_{WN}^S(\lambda,\theta,\phi)=\frac{L_W^S\left[\lambda,\theta,\phi,\theta_o,\tau_a,W,Chl\right]}{t(\lambda,\theta_o)\cos\theta_o\left(\frac{d_o}{d}\right)^2}, \tag{4.18}$$

since $E_d(0^+,\lambda)$ can be calculated as $E_d(0^+,\lambda)=\overline{F}_o(\lambda)t(\lambda,\theta_o)\cos\theta_o\left(\frac{d_o}{d}\right)^2$, where d_0 and d are the mean and actual sun-earth distances, respectively, and $t(\lambda,\theta_o)$ is the diffuse transmittance of the atmosphere when the solar zenith angle is θ_o. Although not shown explicitly, $t(\lambda,\theta_o)$ also depends on the optical depths of aerosols and ozone, and on variations in the Rayleigh optical depth with surface atmospheric pressure.

Although the full dependence of $L_{WN}^S(\lambda,\theta,\phi)$ on geometric, environmental and IOP factors is not indicated explicitly in its traditional notation, the quantity retains a strong bidirectional nature that can be clearly seen by substituting Equation (4.16) for the numerator on the right-hand-side of Equation (4.18). Because of these remaining dependencies, satellite normalized water-leaving radiances $L_{WN}^S(\lambda,\theta,\phi)$ are not directly comparable, from one pixel of the scene to another one, from one day to another day for the same pixel, or from one ocean color sensor to another one. The mapping, or merging of such quantities, when for instance *level 3* products are derived, is neither meaningful nor licit. A way to circumvent these drawbacks consists of assuming that the sun was at zenith and that the pixel has been seen vertically, and thus to determine an ***exact normalized water-leaving radiance*** $L_{WN}^{ex}(\lambda)$ that is no longer dependent on bidirectional factors. To transform $L_{WN}^S(\lambda,\theta,\phi)$ to $L_{WN}^{ex}(\lambda)$, Equation (4.8) is used to first express the ratio

$$\frac{L_{WN}^{ex}(\lambda)}{L_{WN}^S(\lambda,\theta,\phi)}=\frac{E_d(0^+,\lambda,\theta_o)L_W\left[\lambda,0,0,0,\tau_a,W,Chl\right]}{E_d(0^+,\lambda,0)L_W^S\left[\lambda,\theta,\phi,\theta_o,\tau_a,W,Chl\right]}, \tag{4.19}$$

where $E_d(0^+,\lambda,0)$ and $L_W\left[\lambda,0,0,0,\tau_a,W,Chl\right]$ are respectively the unknown incident irradiance and water-leaving radiance that would have been measured for $\theta=\theta'=\theta_o=0$ and ϕ, although indeterminate, is denoted also as ϕ = 0. When Equation (4.16) is used to expand $L_W\left[\lambda,0,0,0,\tau_a,W,Chl\right]$ and $L_W\left[\lambda,\theta,\phi,\theta_o,\tau_a,W,Chl\right]$ in (4.19), the solution obtains as

$$L_{WN}^{ex}(\lambda)=L_{WN}^S(\lambda,\theta,\phi)\frac{\Re_o}{\Re(\theta',W)}\frac{f_o(\lambda,\tau_a,Chl)}{Q_o(\lambda,\tau_a,Chl)}\left(\frac{f(\lambda,\theta_o,\tau_a,Chl)}{Q(\lambda,\theta',\phi,\theta_o,\tau_a,Chl)}\right)^{-1}, \tag{4.20}$$

where $f_o(\lambda, \tau_a, Chl)$ is the particular value taken by the function f when $\theta_o = 0$, and $Q_o(\lambda, \tau_a, Chl)$ is the particular value of the function Q when $\theta_o = 0$ and $\theta = \theta' = 0$. As in Equation (4.16), the wind speed dependence is retained only in $\Re(\theta', W)$ (Figure 4.4), as it is neglibly weak for the $\frac{f}{Q}$ ratios (see Fig. 9 in Morel and Gentili 1996).

Field measurements

The water-leaving radiances are determined either from above-water measurements (typically at $\theta \approx 40°$, $\theta' \approx 29°$ and $\phi \geq 90°$; see Volume III, Chapter 3), or from in-water measurements extrapolated to z = 0^- and transmitted through the interface ($\theta = \theta' = 0$; see Volume III, Chapter 2 and Volume VI, Chapters 2 and 3). Since usually, $E_d(0^+, \lambda, \theta_o)$ is also determined during such measurements, the transformations into remote sensing reflectance and normalized water-leaving radiance are straightforward. The bidirectionality problems are identical to the previous one. These field water-leaving radiances, after the normalization leading to $L_{WN}^{abw}(\lambda, \theta, \phi)$ for above-water measurements, or $L_{WN}^{inw}(\lambda)$ for in-water measurements, are still not comparable with each other, nor with the corresponding satellite quantity $L_{WN}^{S}(\lambda, \theta, \phi)$. They also must be transformed into $L_{WN}^{ex}(\lambda)$ to allow comparisons to be made.

When the measurements are effected via the ***above-water method***, the geometry is exactly the same as that for a satellite sensor, so that the transformation of $L_{WN}^{abw}(\lambda, \theta, \phi)$ into $L_{WN}^{ex}(\lambda)$ is performed using Equation (4.20), with fixed (θ', ϕ) values determined by the measurement protocol (Volume III, Chapter 3).

When the measurements are effected via the ***in-water method***, the sole difference comes from the nadir viewing strategy $(\theta = \theta' = 0)$, which simplifies the transformation from $L_{WN}^{inw}(\lambda)$ to $L_{WN}^{ex}(\lambda)$. In this situation, $\Re(\theta', W)$ reduces to $\Re_o$, and $Q(\lambda, \theta', \phi, \theta_o, \tau_a, Chl)$ reduces to the restricted form $Q_n(\lambda, \theta_o, \tau_a, Chl)$ relevant for nadir viewing. With these substitutions, Equation (4.20) reduces to

$$L_{WN}^{ex}(\lambda) = L_{WN}^{inw}(\lambda) \frac{f_o(\lambda, \tau_a, Chl)}{Q_o(\lambda, \tau_a, Chl)} \left(\frac{f(\lambda, \theta_o, \tau_a, Chl)}{Q_n(\lambda, \theta_o, \tau_a, Chl)} \right)^{-1}. \tag{4.21}$$

The different angular dependencies in normalized water-leaving radiances derived from *in situ* measurements above-water, or in-water, may be emphasized by dividing (4.20) by (4.21) to obtain

$$L_{WN}^{inw}(\lambda) = L_{WN}^{abw}(\lambda, \theta, \phi) \frac{\Re_o}{\Re(\theta', W)} \frac{Q(\lambda, \theta', \phi, \theta_o, \tau_a, Chl)}{Q_n(\lambda, \theta_o, \tau_a, Chl)}. \tag{4.22}$$

These radiances derived from field experiments must be transformed into exact normalized water-leaving radiances if they are to be compared to those derived from space measurements [already transformed according to Equation (4.20)].

Other useful relationships

The irradiance reflectance, Equation (4.5), has been extensively determined at sea, and also has been modeled. As only irradiances are involved in its definition, its only angular dependencies are related to the illumination geometry, via the factor $f(\lambda, \theta_o, \tau_a, Chl)$ in equation (4.12a). The irradiance reflectance and the exact normalized water-leaving radiance are related through Equations (4.12a) and (4.16) as

$$L_{WN}^{ex}(\lambda) = \frac{R(0^-, \lambda, \theta_o) \overline{F}_o(\lambda) \Re_o}{Q_n(\lambda, \theta_o, \tau_a, Chl)}. \tag{4.23}$$

4.6 GENERATION AND BEHAVIOR OF THE $\Re$, f, AND Q QUANTITIES

The reflection-refraction term $\Re$

In correspondence with n = 1.34, a typical value for seawater (salinity of 35 PSU, temperature 15°C, and λ = 550 nm), the n^{-2} term amounts to 0.557. Actually, at a given temperature T, $n(\lambda,T)$ decreases by about 1 % throughout the visible spectrum, and at a given wavelength, decreases by 0.1 % for a temperature varying from 0 to 30°C. Therefore, extreme values for the n^{-2} term would range from 0.547 (at 400 nm, and at 0°C) to 0.561 (at 700 nm, and 30°C) (Austin and Halikas 1976). It can safely be considered as constant, for practical applications.

The transmittance factor $(1-\overline{\rho})$ which applies to the downward irradiance (sun + sky) is approximately 0.957. It decreases to 0.925 for low solar elevation and increasing atmospheric turbidity, while it increases and may reach 0.97 for extremely clear blue skies, small solar zenith angle, and red wavelengths. The internal reflectance $\left[1-\overline{r}R\left(0^-,\lambda,\theta_o\right)\right]$, where $\overline{r}\cong 0.49$, may vary between 1 and 0.951 for an irradiance reflectance $0<R\left(0^-,\lambda,\theta_o\right)\leq 0.1$. In total, these variations are rather weak.

The most important term governing the variations in $\Re(\theta',W)$ is the downward reflection $\rho(\theta',\theta;W)$, which prevents part of the upward radiance from emerging. The resulting transmittance is nearly constant and essentially independent from the sea state with a value $\left[1-\rho(\theta',\theta;W)\right]\cong 0.979$ for $\theta<25°$. At the other extreme, as θ' approaches the critical angle, the upward transmittance decreases abruptly toward 0, and the slope of this decrease for slant emerging radiances depends heavily on the capillary wave slopes, as governed by wind speed W (Figure 4.4). This rapid decrease in the $\Re(\theta',W)$ values for $\theta>30°$ (or $\theta'>22°$) is, at least in part, at the origin of difficulties in assessing marine radiance at the edge of the swath for a satellite ocean color sensor. Note also that most applications [Equations (4.20) and (4.21)] actually involve the ratio $\frac{\Re_o}{\Re(\theta',W)}$ for two specified directions (0 and θ'). Therefore, the variations of such ratios are more sensitive to the changes in the transmittance term (and to the θ' angle and wind speed), rather than to the selection of constant and approximate values for $\overline{r}$ and $\overline{\rho}$, variations in which tend to cancel out.

Prediction of the f and Q factors

These quantities have been scarcely determined at sea. Therefore, their prediction presently relies essentially on computations, by which the radiative transfer equation (RTE) is accurately solved for various IOP and prescribed boundary conditions corresponding to the incident radiative regime to be simulated. Such computations must address simultaneously the two media, atmosphere and ocean, inasmuch as the boundary conditions depend i) on the sun position, the optical thickness and nature of aerosols, and ii) on the sea state, derived from the wind speed through the Cox and Munk (1954) surface slopes statistics. They also can include the inelastic processes. As far as the numerical aspects are concerned, there is no difference between Case 1 and Case 2 waters. The major difference, however, originates from the unequal abilities in modeling the needed IOP for the two kinds of waters.

For Case 2 waters, the optically significant substances (phytoplankton, colored dissolved organic matter, and all kinds of non-algal particles) are varying in wide proportions, and independently from each other. The non-algal component may contain various organic and mineral particles, likely with differing VSF. Therefore computations have to be made case-by-case, with the relevant IOP as input parameters, to the extent they are known. In the particular case of extremely turbid waters, with high reflectance and a well-established multiple scattering regime, Q tends to approach π, albeit very slowly, whatever the VSF (Loisel and Morel 2001).

In Case 1 waters, beside the water molecules themselves, the optically significant components are phytoplankton and their associated materials living or inanimate, particulate or dissolved, collectively called the *biogenic material*. The quantification of this biogenic material has been operationally made through the concentration [mg m^{-3}] of a major pigment, chlorophyll *a* (*Chl*). By definition therefore, the IOP of these waters

depend on, and have historically been related to, *Chl* concentration. In this way, the IOP of Case 1 waters can, in principle, be universally expressed for all wavelengths as functions of *Chl*. This obviously is a useful empirical approximation, but only an approximation.

In a first series of papers (Morel and Gentili 1991,1993,1996), empirical relationships were introduced, by which $a(\lambda)$ and $b(\lambda)$ were expressed as functions of *Chl*. The additional hypothesis was to consider that the particle phase function for the biogenic material was well represented by the Petzold (1972) mean phase function, as used in Mobley *et al.* (1993) and tabulated in Mobley (1994). It was emphatically acknowledged that the adoption of a unique phase function for oceanic particulates is undoubtedly a weakness, especially because the backscattering probability, $\tilde{b}_{bp}(\lambda) \equiv \frac{b_{bp}(\lambda)}{b_b(\lambda)}$, resulting from the Petzold mean phase function is too high ($\tilde{b}_{bp}(\lambda) \cong 0.019$). This assumption is, moreover, incompatible with the empirical parameterization of $\tilde{b}_{bp}(\lambda)$ as a function of *Chl* (Morel and Maritorena, 2001). This drawback prevented the *Q* values from being reliable at $Chl > 1$ mg m^{-3}.

In an attempt to remove this drawback, a *Chl*-dependent particle phase function has been adopted (Morel and Gentili, in prep.), in such a way that $\tilde{b}_{bp}(\lambda)$ is allowed to decrease with increasing *Chl*, and thus it becomes fully compatible with the empirical relationship. The parameterizations of $a(\lambda)$ and $b(\lambda)$ with respect to *Chl* have also been slightly adjusted according to new results presented in Loisel and Morel (1998) and Morel and Maritorena (2001). With respect to the previously published results, as displayed and discussed in Morel and Gentili (1996), the above changes have a minor impact on the results for *f* and *Q* when the chlorophyll concentration is low enough ($Chl < 1$ mg m^{-3}). Above this threshold, the newly adopted (and *Chl*-dependent) phase function, which is less steep in backward directions than the Petzold (1972) mean phase function, leads to smoother *Q*-patterns. At very low concentration ($Chl < 1$ mg m^{-3}), important changes in *f* result if Raman emission is included in its determination. The data shown below as examples in Figures 4.5 through 4.10 have been derived using this new parameterization.

Variations of the f-factor

Early studies have shown that $f \approx \frac{1}{3}$ when the sun is near zenith. Later it was realized (Kirk 1984; Gordon 1989) that it varies appreciably with solar altitude, and also that this sun position dependence is influenced by the relative importance of the molecular and particle scattering in the total scattering process (Morel and Gentili 1991). The global range of variation in the *f* function is from about 0.30 to 0.60 (and *f* may take even greater values for high *Chl* at λ = 560 nm). As a general rule, for any given *Chl* concentration and wavelength, *f* takes its minimal values f_o when the sun is at zenith, and increases systematically with increasing solar zenith angle (Figures 4.5a, 4.5b, and 4.6).

The magnitude of the *f* function and its variations are determined by the IOP. The dimensionless parameters η_b and ϖ derived from the IOP give convenient clues to gain some understanding of the physical processes underlying this dependence. When ϖ is below approximately 0.8, the *f* is essentially governed by η_b; it is progressively less sensitive to the sun position when η_b increases, because molecular scattering predominates (the nearly isotropic shape of the molecular VSF explains this diminishing sensitivity to the sun's position). When ϖ exceeds 0.9, both parameters (η_b and ϖ) play a part in fixing *f* (Morel and Gentili, 1991). When ϖ approaches 1 (high $\tilde{n}$ values), a highly diffuse regime prevails and *f*' tends monotonically toward 1. In contrast, *f* tends toward 0 and it is not a monotonic function of $\tilde{n}$, the average number of scattering events (Loisel and Morel, 2001). Such a quasi-isotropic regime becomes insensitive to the solar illumination geometry, and consequently the *f* variations with θ_o tend to lessen. This may happen in very turbid case 2 waters, but never happens in case 1 waters, as shown in Fig. 4.5.

The behavior of the function *f* for various *Chl* and wavelengths can be interpreted by keeping in mind the corresponding values taken by η_b and ϖ. In Case 1 waters, $\varpi(\lambda) < 0.9$ for all wavelengths as long as $Chl < 3$ mg m^{-3}; $\varpi(\lambda)$ may slightly exceed 0.9 in the green part of the spectrum (555 nm to 565 nm) only when

$Chl > 3$ mg m^{-3}. Referring to the examples displayed in Figure 4.5, when $Chl = 0.03$ mg m^{-3} and $\lambda = 412.5$ nm, $\varpi(412.5)$ is slightly below 0.8, $\eta_b(412.5) = 0.85$ is maximum, and $f(412.5)$ remains rather flat (indicating molecular scattering). With increasing *Chl*, $\eta_b(412.5)$ decreases strongly (down to 0.1 when $Chl = 10$ mg m^{-3}), while $\varpi(412.5)$ remains practically unchanged, the $f(412.5)$ values are larger and more dependent on the sun position. At 560 nm, and for increasing *Chl*, the situation is more complex, since $\eta_b(560)$ decreases (as for 412.5), but $\varpi(560)$ is no longer steady and now varies from 0.3 to 0.9. Therefore, $f(560)$ becomes more widely changing and exhibits higher values than at 412.5 nm. The preceding examples are derived under the hypothesis of elastic scattering only.

Because the Raman emission adds a flux to the elastically backscattered flux, this process directly increases *f* for all wavelengths, regardless of the sun position. This effect is maximal when the elastic scattering is minimal, namely for waters with low *Chl* and low particle content. Consider the situation when $Chl = 0.03$ mg m^{-3} (Figure 4.6). In the red, where elastic scattering due to water and particles (at low concentration) is weak, $f(660)$ increases by 15 %. On the other hand, in the blue portion of the spectrum, where the $\lambda^{-4.3}$ dependent elastic scattering by water is strong, $f(442.5)$ increases by only 5 %. The Raman emission has no significant effect on the *f* function when the elastic scattering, becomes important, as is the case at high chlorophyll concentration (*e.g.*, $Chl > 1$ mg m^{-3}).

In summary (see Figures 4.5 and 4.6):

- Whatever the wavelength, $f(\lambda, \theta_o, \tau_a, Chl)$ is minimal when $\theta_o = 0$, and always increases with increasing θ_o.
- For a given θ_o and fixed wavelength, $f(\lambda, \theta_o, \tau_a, Chl)$ always increases with increasing *Chl*.
- The sun-dependent variations in $f(\lambda, \theta_o, \tau_a, Chl)$ are increasingly wider for increasing *Chl*.
- The Raman effect systematically increases $f(\lambda, \theta_o, \tau_a, Chl)$, relative to corresponding values when this effect is ignored.
- At low *Chl*, the Raman effect impacts significantly $f(\lambda, \theta_o, \tau_a, Chl)$, but the effect practically vanishes for $Chl > 1$ mg m^{-3}.

Variations of the bidirectional function $Q(\lambda, \theta', \phi, \theta_o, \tau_a, Chl)$

By virtue of its definition [Equation (4.6)], the magnitude of $Q(\lambda, \theta', \phi, \theta_o, \tau_a, Chl)$ in any direction (θ', ϕ) is inversely proportional to that of $L_u(0^-, \lambda, \theta', \phi, \theta_o, \tau_a, Chl)$, the angular distribution of which is illustrated in Figures 4.2 and 4.3. The solar principal plane $(\phi = 0 \text{ and } \pi)$ is a plane of symmetry for the upward light field; the maximum and minimum values of $Q(\lambda, \theta', \phi, \theta_o, \tau_a, Chl)$ are found in this plane, and are respectively coincident with the minimum and maximum values of $L_u(0^-, \lambda, \theta', \phi, \theta_o, \tau_a, Chl)$ (Figure 4.3). The minimal values of $Q(\lambda, \theta', \phi, \theta_o, \tau_a, Chl)$ occur for almost horizontal directions $\left(\theta' \text{ approaching } \frac{\pi}{2}\right)$ that are not involved in remote sensing. The maximal values of $Q(\lambda, \theta', \phi, \theta_o, \tau_a, Chl)$ occur in directions $(\theta', \phi = 0 \text{ or } \pi)$ that depend on the sun zenith angle θ_o and on the IOP, expressed here as functions of *Chl* (Figure 4.3).

The effect of increasing aerosol loading, indexed by τ_a is to increase the diffuse component of the downward radiant illumination field. This effect tends to smooth the $Q(\lambda, \theta', \phi, \theta_o, \tau_a, Chl)$ distribution, but only slightly, and

the influence of τ_a may be neglected for the present discussion. Nevertheless, there still remain 5 variables that strongly influence $Q(\lambda, \theta', \phi, \theta_o, Chl)$. The description of such a 5-dimensional lookup table is rather difficult, and is necessarily simplified.

Considered first is the case when both the viewing and solar zenith angles are held fixed at $\theta' = 0$ and $\theta_o = 0$, respectively, *i.e.* the quantity $Q_o(\lambda, Chl)$ [τ_a neglected] introduced above in Equation (4.20). Assuming only elastic scattering, simulated variations of $Q_o(\lambda, Chl)$ with wavelength $(410 \le \lambda \le 660 \text{ nm})$ and chlorophyll concentration $(0.03 \le Chl \le 10 \text{ mg m}^{-3})$ are illustrated as solid lines in Figure 4.7a; $Q_o(\lambda, Chl)$ increases monotonically with increasing *Chl*, and is only weakly dependent on wavelength λ.

The second step consists of examining the evolution with the sun angle θ_o of the quantity $Q_n(\lambda, \theta_o, Chl)$, introduced in Equation (4.21) for nadir viewing cases $(\theta' = 0)$ when generally $\theta_o \ne 0$. Again considering only elastic scattering, the solid curves in Figure 4.7b show the variability in $Q_n(\lambda, \theta_o, Chl)$ with variations in θ_o $(0° \le \theta_o \le 75°)$ for 4 chlorophyll concentrations and 4 wavelengths. Variations of $Q_n(\lambda, \theta_o, Chl)$ with chlorophyll $(0.03 \le Chl \le 10 \text{ mg m}^{-3})$, with Raman emission included (see below), are shown in Figure 4.8 for 6 wavelengths and 4 solar zenith angles θ_o. The $Q_n(\lambda, \theta_o, Chl)$ function exhibits the following properties (Figures 4.7b and 4.8):

- It is always minimal when $\theta_o = 0$, and steadily increases when θ_o increases, for all wavelengths and all chlorophyll concentrations.
- The span of its variation with θ_o is relatively wider at high *Chl* than at low *Chl*.
- Its highest values are found in the red part of the spectrum when $\theta_o = 75°$ and $Chl \ge 3 \text{ mg m}^{-3}$, *e.g.* $Q_n(660 \text{ nm}, 75°, 3 \text{ mg m}^{-3}) > 6$ in Figure 4.7b.

As was previously discussed in Section 4.3, the quasi-isotropic angular distribution of Raman scattering tends to smooth out the angular structure which particle scattering imposes on the upward radiance field. However, Raman emission has only a modest influence on the $Q(\lambda, \theta', \phi, \theta_o, Chl)$ function, as illustrated for $Q_o(\lambda, Chl)$ and $Q_n(\lambda, \theta_o, Chl)$ by dashed lines in Figure 4.7, for two simple reasons. At low *Chl* concentrations, Raman emission is a significant contribution to the upward radiant field, but its angular distribution and that of the underlying, predominately molecular elastic scattering are similarly quasi-isotropic. At high Chl, on the other hand, the elastic scattering by particles is much larger in magnitude than the Raman emission. In this situation, the tendency of Raman scattering to smooth the more structured pattern of the radiance field is simply too weak to be significant. In all cases illustrated in Figure 4.7, the influence of Raman emission, although weak, is most apparent at longer wavelengths. As λ increases in the spectral region $\lambda > 565 \text{ nm}$, the molecular scattering contribution to $\beta(\lambda, \Psi)$ progressively decreases, while $a_w(\lambda)$ progressively increases. These tendencies with increasing λ progressively reduce the $\frac{b_b(\lambda)}{a(\lambda)}$ ratio and upward radiant field due to elastic scattering and increase the angular structure of the radiance distribution (especially at large θ_o). Under these conditions, the Raman emission becomes a concomitantly larger fraction of the upwelled radiant field, and its tendency to smooth the angular pattern of the field is enhanced as well.

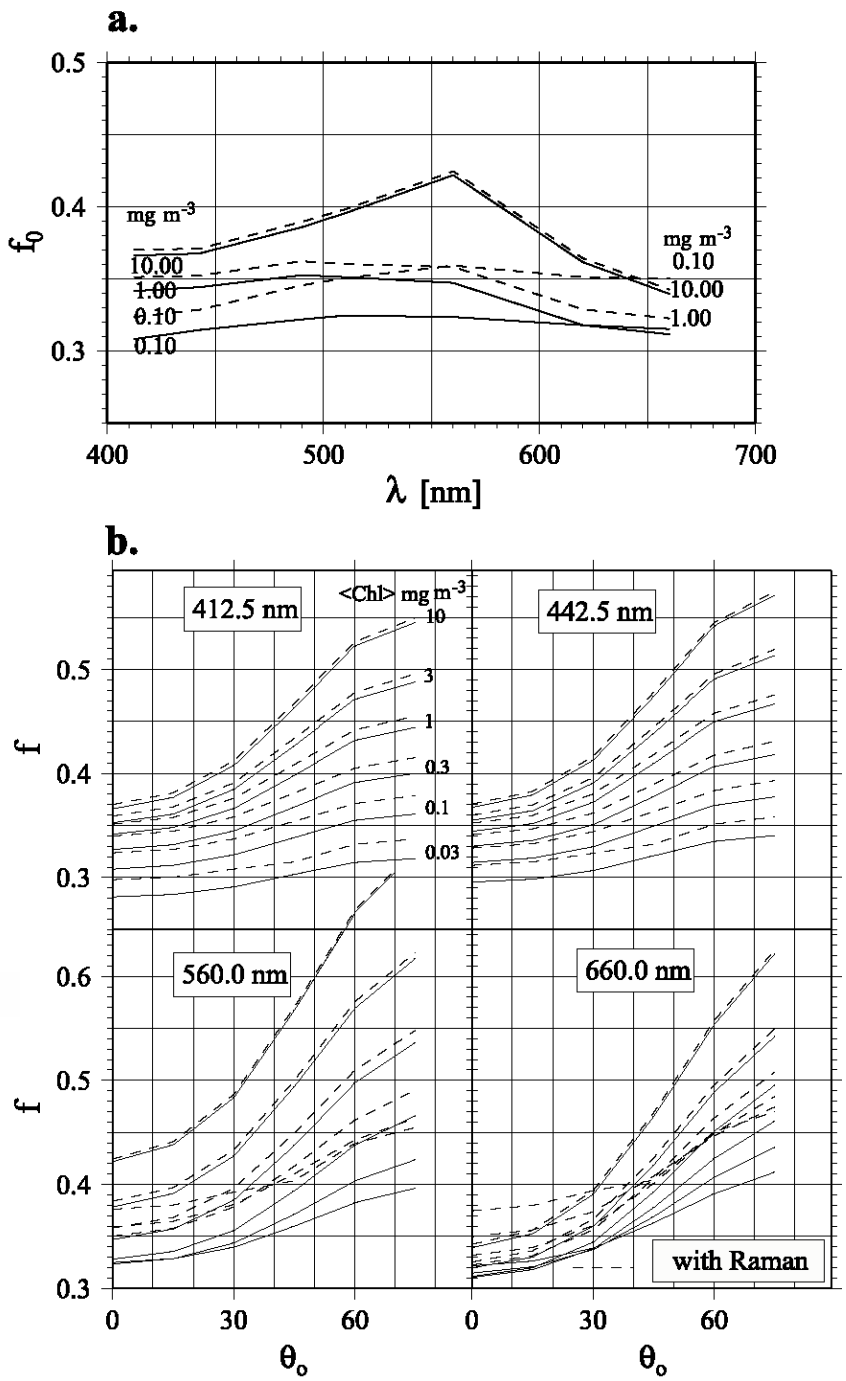

Figure 4.5: a): Spectral distribution of f_0, the particular value of the function f when the sun-zenith angle is 0, for different Chl values, as indicated. The solid curves are for elastic scattering only, and the dashed curves include the effect of the Raman emission. b): Evolution of the function f (Equation 4.12a) with the zenith solar angle (up to 75°), for various wavelengths as indicated. From bottom to top in each panel, the curves are for Case 1 waters with Chl = 0.03, 0.1, 0.3, 1, 3, and 10 mg m^{-3}, respectively. Solid and dashed curves respectively correspond to determinations without, or with, Raman scattering.

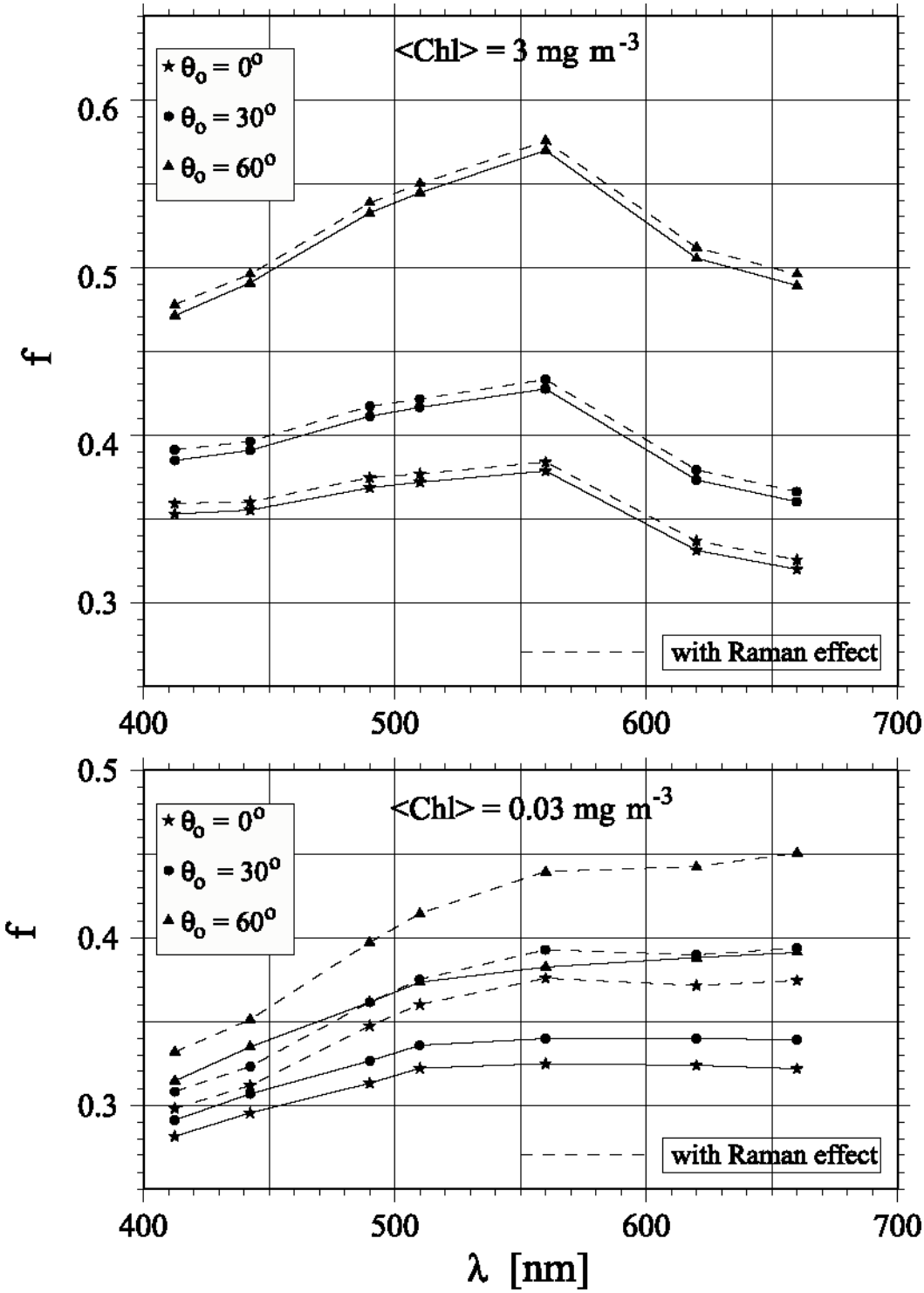

Figure 4.6: Spectral distribution of the function f, with and without the Raman contribution, for 2 chlorophyll concentrations and 3 solar zenith angles, θ_o, as indicated.

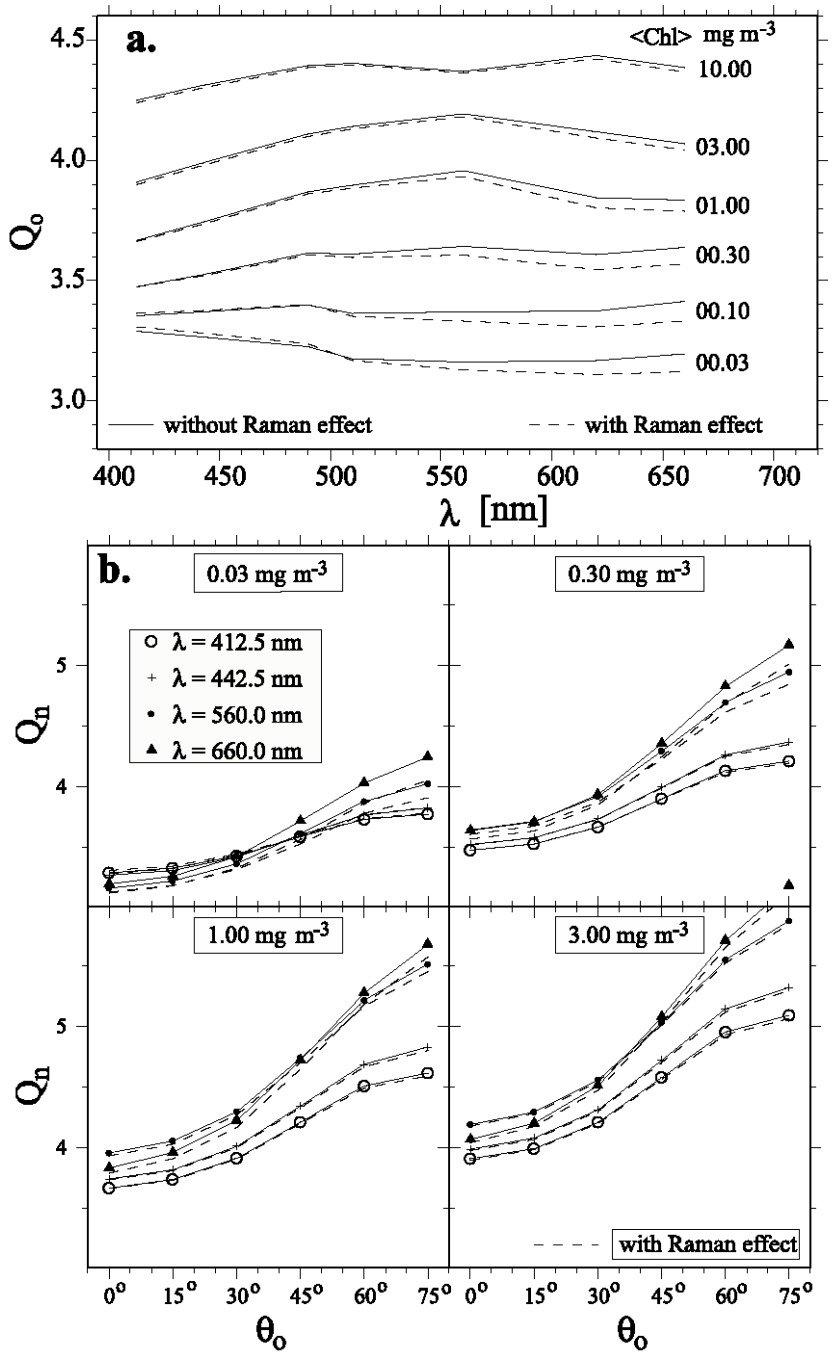

Figure 4.7: a): Spectral values of Q_0, the particular value of Q when θ' and $\theta_o = 0$, for increasing Chl, with and without the Raman contribution. b): Evolution of Q_n (Eqs. 4.6 and 4.26) with solar zenith angle, θ_o, for 4 wavelengths, and 4 chlorophyll concentrations, as indicated.

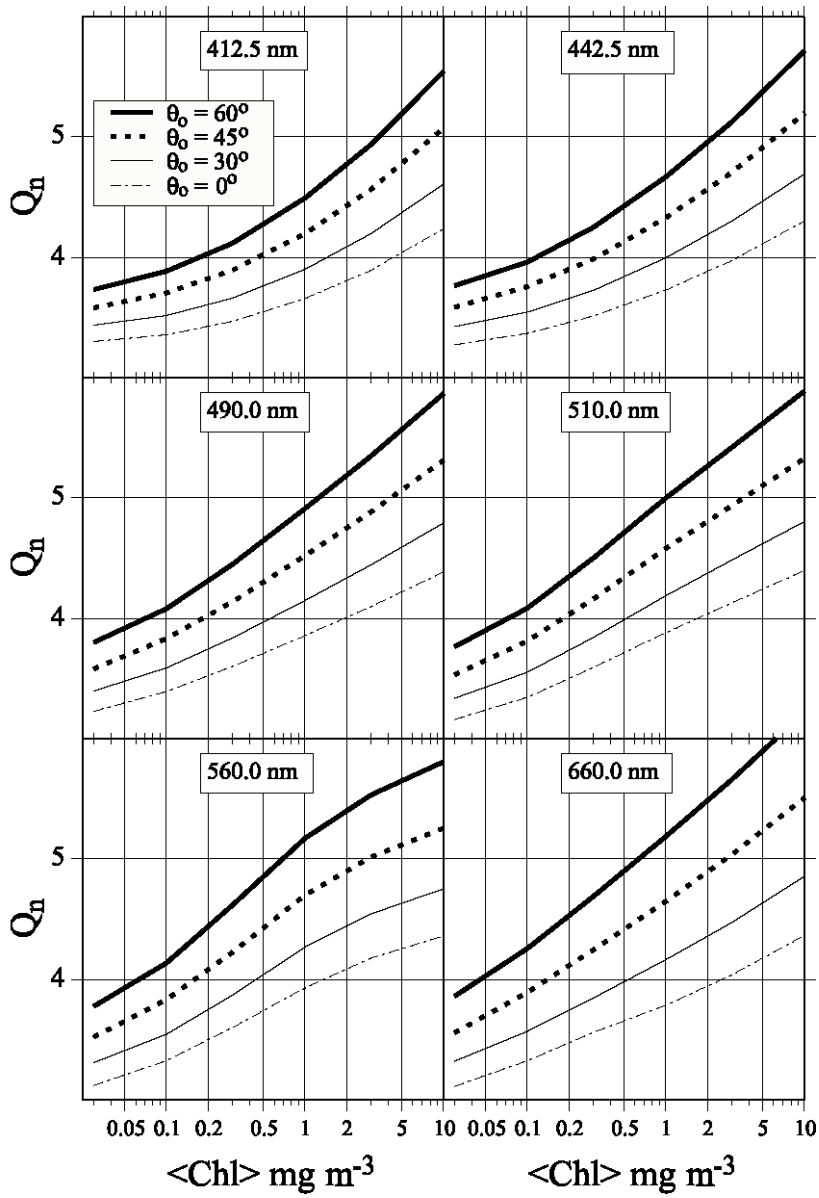

Figure 4.8: Evolution of the Q_n function with increasing chlorophyll concentration, for 6 wavelengths, and 4 solar zenith angles, as indicated. These Q_n values account for the Raman influence.

Polar diagrams are the most convenient way to visualize the behavior of the $Q(\lambda,\theta',\phi,\theta_o,Chl)$ function with θ' (see *e.g.*, Fig 5 in Morel and Gentili 1993). Examples of the angular pattern of the quantity $\frac{L_u(0^-,\lambda,\theta',\phi,\theta_o,Chl)}{E_u(0^-,\lambda)}$ $(i.e.\ Q^{-1})$ in the principal plane containing the sun are shown in Figure 4.9 for a fixed solar zenith angle $\theta_o = 30°$. The contours for $Q = 5$, π, and 2 are indicated, as are also the radial lines corresponding to the critical angle $\theta_c \cong 48°$. These examples practically encompass all possible cases, and thus it is worth noting that inside the Snell cone $\theta' < \theta'_c$, $\pi \le Q(\lambda,\theta',\phi,30°,Chl) \le 5$ for all λ and *Chl*. The largest difference in angular patterns is between a) the case when $\lambda = 442.5$ nm, $Chl = 0.03$ mg m^{-3}, $\eta_b = 0.88$, and molecular scattering

dominates backscattering, and b) the case when $\lambda = 660$ nm, $Chl = 10$ mg m^{-3}, $\eta_b = 0.04$, and particle scattering dominates backscattering.

Variations of the $\frac{f}{Q}$ *ratio*

Examination of Figures 4.5b and 4.7b shows that both the f and Q_n functions experience concomitant increases when the sun zenith angle increases. Therefore, their ratio is less dependent on θ_o. The variations of the particular quantity $\frac{f_o(\lambda, \tau_a, Chl)}{Q_o(\lambda, \tau_a, Chl)}$ are examined at first in Figure 4.10a, where examples are shown as functions of the wavelength for varying chlorophyll concentrations. The influence of the Raman scattering (dashed lines in Figure 4.10a)) is considerable when $Chl < 1$ mg m^{-3}, due to strong enhancement of $f_o(\lambda, \tau_a, Chl)$. The overall variation of this quantity is in the range $0.075 \le \frac{f_o}{Q_o} \le 0.12$, and the extreme limiting values both occur in the red part of the spectrum. In the blue spectral region $(\lambda < 450 \text{ nm})$, the variations are within the narrower interval $0.085 \le \frac{f_o}{Q_o} \le 0.097$.

Regarding the general quantity $\frac{f(\lambda, \theta_o, \tau_a, Chl)}{Q(\lambda, \theta', \phi, \theta_o, \tau_a, Chl)}$, the strongest variations are expected to occur within the sun's principal plane $(\phi = 0 \text{ and } \pi)$; and minimal angular variations are in the perpendicular plane $\left(\phi = \frac{\pi}{2} \text{ and } \frac{3\pi}{2}\right)$. Typical variations of this ratio are shown in Figure 4.10b for the principal plane and perpendicular half-plane; they essentially remain within the range $0.08 \le \frac{f}{Q} \le 0.15$, centered about the mean value 0.11 found by Gordon *et al*. (1988). When approaching the critical angle, higher $\frac{f}{Q}$ values are possible, particularly for large sun-zenith angle, and high chlorophyll concentration.

The spectral dependency of the $\frac{f}{Q}$ ratio is marked for low Chl $(e.g.$ when $Chl = 0.03$ mg m$^{-3})$, essentially because the influence of the Raman scattering is important for the green and red radiation, and therefore, it enhances f. When $Chl \approx 0.3$ mg m^{-3}, the spectral dependency of $\frac{f}{Q}$ has practically vanished; it reappears at $Chl \approx 3$ mg m^{-3}, and now the lowest $\frac{f}{Q}$ values occur at 660 nm. Strongly featured $\frac{f}{Q}$ angular patterns at all wavelengths are typical of high Chl concentrations. It must be noticed that the asymmetrical $\frac{f}{Q}$ pattern occurring when the solar angle departs from 0, is reversed from low to high chlorophyll concentrations.

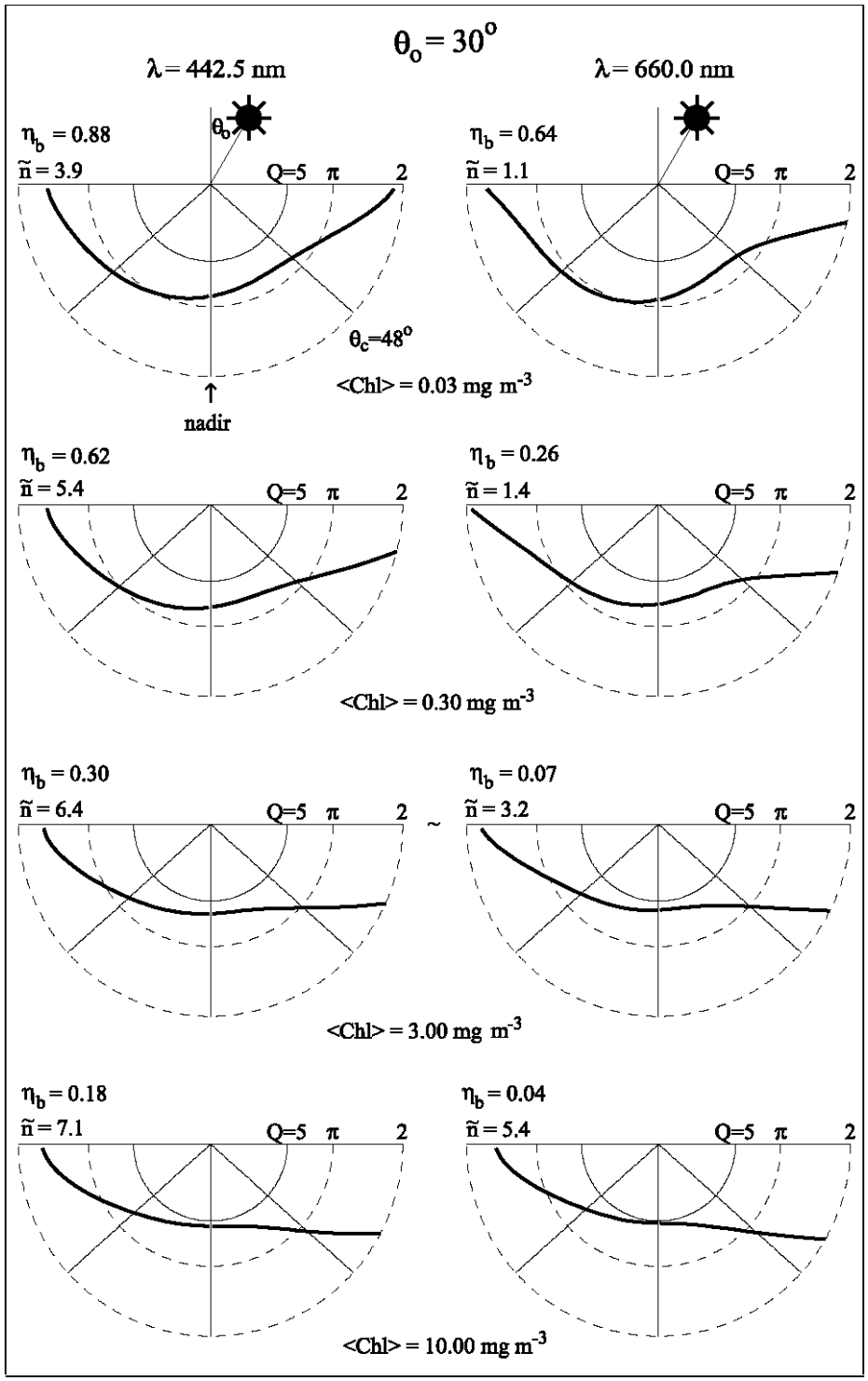

Figure 4.9: Selected examples of the upward radiance field within the sun's principal plane (plotted as in Fig. 4.3), for 2 wavelengths, and 4 chlorophyll concentrations, as indicated. Also provided are the backscattering ratios η_b and average numbers of photon scattering events $\tilde{n}$ [see Equations (4.14) and (4.15)] corresponding to each case. The sun position is the same for all graphs (θ_o = 30°). These radiance fields include Raman emission.

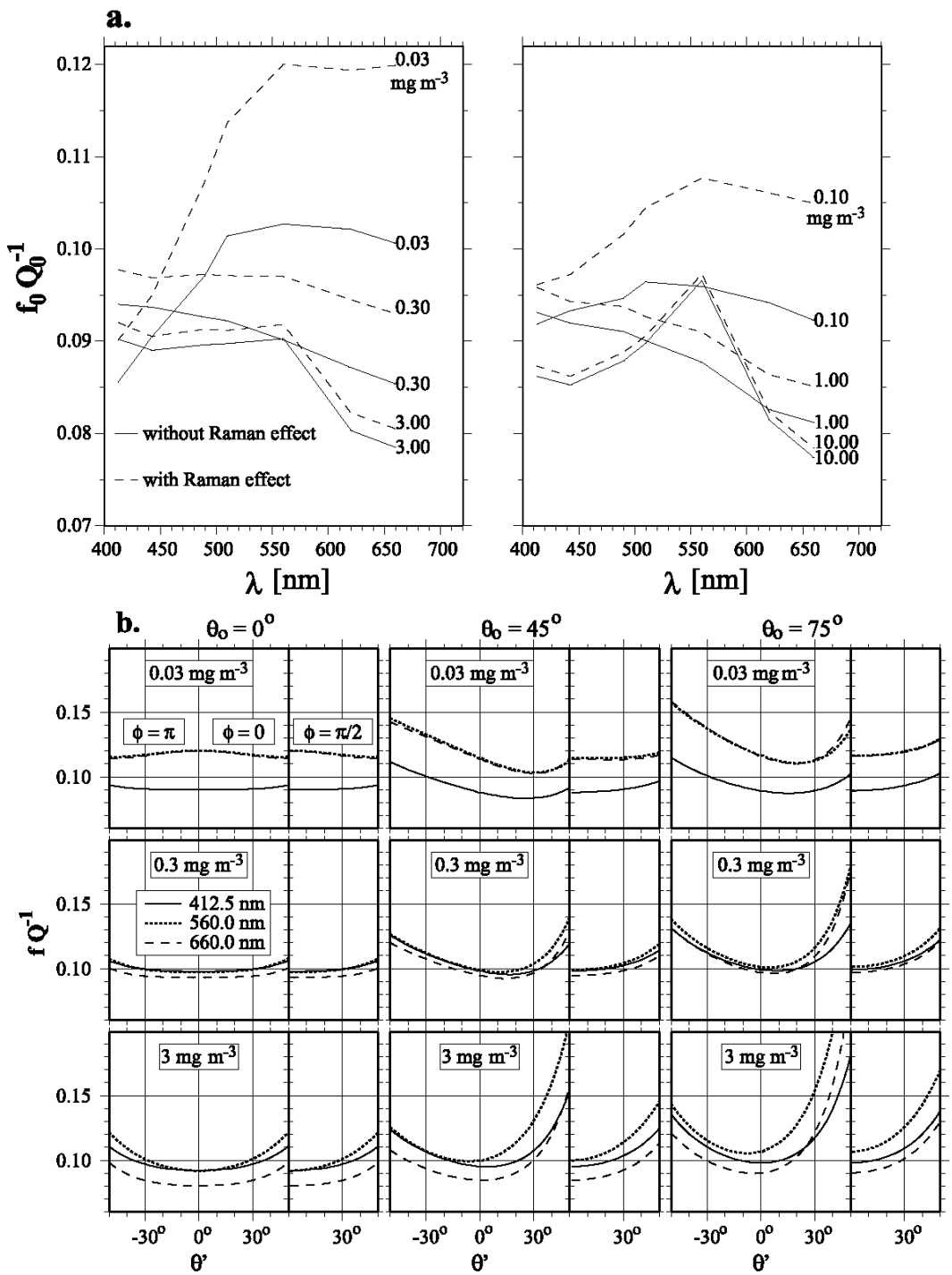

Figure 4.10: a): Spectral values of the ratio $f_o Q_o^{-1}$, with and without the Raman effect, for various chlorophyll concentrations. b): The $f Q^{-1}$ ratio as a function of θ' for 3 chlorophyll concentration, 3 solar zenith angles and 3 wavelengths (as indicated). The curves are plotted within the principal plane $[\phi = 0 \text{ and } \pi]$ and the vertical half-plane perpendicular to the principal plane $[\phi = \pi/2]$.

4.7. CORRECTION PROCEDURES FOR BIDIRECTIONALITY

The correction consists of operating Equations (4.8) and (4.20) or (4.21), in order to derive the exact normalized water-leaving radiance from water-leaving radiances, as determined from satellite measurements, or from in-water or above-water measurements in the field. These transformations require the quantities $\frac{f}{Q}$, Q (or f), and $\Re$. Conveniently, these values can be determined by interpolation within precomputed lookup tables, which are built by solving the RTE under specified boundary conditions, using the appropriate IOP describing the water bodies of interest. For the last point, various parameterizations are possible, so that everybody may have his own preference and can produce his own lookup tables. Very likely several of these will be built in the near future.

The lookup tables succinctly described below are ready for use, and may be obtained over the Internet (see below). These tables offer investigators an option for parameterizing the IOP of Case 1 waters as functions of the chlorophyll concentration, as described in Morel and Maritorena (2001), and summarized below. Such tables must be seen as a first attempt to provide a tool for making the birectionality correction.

The spectral absorption values, as a function of *Chl*, derive from the statistical analysis of the diffuse attenuation coefficient for downward irradiance (K_d) through an iterative procedure (Equations 8, 8', and 8'', in Morel and Maritorena, 2001).

The particle scattering coefficient at 550 nm depends on Chl according to (Loisel and Morel 1998)

$$b_{\mathrm{p}}\left(550, Chl\right) = 0.416\left[Chl\right]^{0.766}, \tag{4.24}$$

and the wavelength dependence is represented through

$$b_{\mathrm{p}}\left(\lambda, Chl\right) = b_{\mathrm{p}}\left(550, Chl\right)\left[\frac{\lambda}{550}\right]^{v}, \tag{4.25}$$

where the varying exponent v is expressed as

$$\begin{aligned} v &= \frac{\log_{10}\left(Chl\right) - 0.3}{2}, \text{ when } 0.02 < Chl < 2 \text{ mg m}^{-3}, \text{ and} \\ v &= 0, \text{ when } Chl \geq 2 \text{ mg m}^{-3}. \end{aligned} \tag{4.26}$$

The volume scattering phase function for particles, $\tilde{\beta}_{\mathrm{p}}\left(\Psi\right)$, is assumed to be independent of wavelength and is varied with chlorophyll concentration to satisfy the constraint that the particle backscattering efficiency fulfills the condition

$$\tilde{b}_{\mathrm{bp}} = 0.007 - 0.0025\log_{10}\left(Chl\right). \tag{4.27}$$

The Raman scattering coefficient at 488 nm is 2.6×10^{-4} m^{-1}, with a λ^{-5} spectral dependence (Bartlett *et al.* 1998). Multispectral RTE computations in the purely elastic mode are needed to determine the excitation flux in the wavelength band corresponding to emission at the wavelength of interest (*e.g.* see Mobley 1994).

Chl must be known to enter the lookup tables. Although the best estimate of *Chl* is derived from the exact normalized water-leaving radiance, the structure of the remote sensing *Chl* algorithms allows this difficulty to be overcome in successive steps. In case 1 waters, the usual ocean color *Chl* algorithms are based on a so-called "blue-green" ratio of water-leaving radiances, *e.g.* $\frac{L_{\mathrm{WN}}^{\mathrm{ex}}\left(443\right)}{L_{\mathrm{WN}}^{\mathrm{ex}}\left(555\right)}$. In a rough first approximation, the bidirectional corrections for a given *Chl* do not differ greatly between these two wavelengths. Therefore, the ratio of uncorrected radiances $\frac{L_{\mathrm{WN}}\left(443\right)}{L_{\mathrm{WN}}\left(555\right)}$, and *Chl* retrievals determined from it, are much less affected by bidirectional effects than are the radiances themselves. This Chl can be used as an initial entry for the lookup tables to determine a first estimate of the exact water-leaving radiances. At iterative procedure may be then followed alternately improve the *Chl* and $L_{\mathrm{WN}}^{\mathrm{ex}}\left(\lambda\right)$ estimates in successive steps (Morel and Gentili 1996).

The main characteristics of these tables are listed and summarized below:

1- Only vertically homogeneous case 1 waters have been considered.

2- The quantities $\Re(\theta', W)$ are tabulated in a separate file at a θ' increment of 1° for a perfectly level interface, and for wind speeds W = 0, 4, 10, and 16 m s^{-1} (cf. Figure 4.4). Residual capillary waves still exist when W = 0, according to the Cox and Munk (1954) formula, so that $\Re(\theta', W)$ differs slightly from values computed with a perfectly flat interface.

3- The quantities $f(\lambda, \theta_o, Chl)$ and $\dfrac{f(\lambda, \theta_o, Chl)}{Q(\lambda, \theta', \phi, \theta_o, Chl)}$ are tabulated as functions of five parameters, organized as follows:

   a. Wavelength, λ (7 values: 412.5, 442.5, 490, 510, 560, 620, 660 nm).

   b. Zenith-sun angle, θ_o (6 values: 0°, 15°, 30°, 45°, 60°, and 75°).

   c. Chlorophyll concentration, *Chl* (6 values: 0.03, 0.1, 0.3, 1.0, 3.0, and 10 mg m^{-3}).

   The results for the above combinations of λ, θ_o and *Chl* are stored in 252 separate files; and each file contains 13 columns and 17 lines for:

   d. Azimuth difference, ϕ (13 values from 0° to 180°, spaced at an increment of 15°), where the convention for the sign of ϕ is as in Figure 4.2.

   e. Nadir angle, θ' (17 values in degrees: 1.078[9], 3.411, 6.289, 9.278, 12.300, 15.330, 18.370, 21.410, 24.450, 27.500, 30.540, 33.590, 36.640, 39.690, 42.730, 45.780, and 48.830).

   Note that wind speed and the aerosol optical thickness dependent variations in f and $\dfrac{f}{Q}$ are neglected, following the assumptions discussed above in Sections 4.4 and 4.6. The f and $\dfrac{f}{Q}$ tables described here were computed assuming $W \equiv 0$, and a maritime aerosol with optical thickness $\tau_a(550) \equiv 0.2$, at the reference wavelength $\lambda = 550$ nm.

4- There are two sets of tables in the format described in 3 above, one set for computations with the Raman effect included, and one without this effect. The tables including the Raman emission must be preferred for most applications. The tables produced in the purely elastic mode are provided for the convenience of those who wish to study the sensitivity of the bidirectional properties to the IOP model, without interference by the Raman contribution.

5- When $60° \geq \theta_o \geq 0°$, the variations of f and Q_n with θ_o (see Figures 4.5b and 4.7b) are well represented, with a relative uncertainty less than 2 %, by linear functions of the form

$$X = X_o + S_X(1 - \cos\theta_o),$$

where X_o is f_o or Q_o and the associated slopes are S_f or S_{Qn}. A similar linear approximation is also possible for the ratio $\dfrac{f}{Q_n}$, which remains valid for θ_o up to 75°; this relationship is less accurate, however, and divergences between the exact and approximate values may reach 3.4 %. In this case, X is $\dfrac{f}{Q_n}$ and S_X is $S_{f/Qn}$. The associated X_o and S_X values are tabulated as functions of wavelength and chlorophyll concentration (as 6 sub-tables) in the file *lin-approx*.

[9] This value must be used for any angle $\theta' < 1.078°$, in particular for $\theta' = 0$.

Copies of the above files may be obtained over the Internet, using anonymous ftp, from oceane.obs-vlfr.fr. Once connected, the user should login as "anonymous" and provide his complete E-mail address as the password. The procedure is as follows:

- ftp oceane.obs-vlfr.fr
- LOGIN: anonymous (and provide password)
- cd pub/gentili
- bin
- get README_FIRST
- get DISTRIB_FQ_with_Raman.tar.gz
- get DISTRIB_FQ_without_Raman.tar.gz
- get rgoth.dat
- get lin-approx.tar
- bye

The file README_FIRST may be of some help in accessing and using the tables.

REFERENCES

Austin, R.W. and G. Halikas, 1976: The index of refraction of seawater. *SIO Ref. 76-1*, Vis. Lab., Scripps Inst. of Oceanography, La Jolla, California, 64pp.

Bartlett, J.S., K.J. Voss, S. Sathyendranath, and A. Vodacek, 1998: Raman scattering by pure water and seawater. *Appl. Opt.*, **37:** 3324-3332.

Cox, C. and W. Munk, 1954: Measurement of the roughness of the sea surface from photographs of the sun's glitter. *J. Opt. Soc. Am.*, **44:** 11838-11850.

Gordon, H.R., 1989: Dependence of the diffuse reflectance of natural waters on the sun angle. *Limol. Oceanogr.*, **34:** 1484-1489.

Gordon, H.R. and D.K. Clark, 1981: Clear water radiances for atmospheric correction of Coastal Zone Color Scanner imagery. *Appl. Opt.*, **20:** 4174-4180.

Gordon, H.R., O.B. Brown, R.H. Evans, J.W. Brown, R.C. Smith, K.S. Baker, and D.K. Clark, 1988. A semi-analytic radiance model of ocean color. *J. Geophy. Res.*, **93:** 10,909-10,924.

Kirk, J.T.O, 1984: Dependence of relationship between inherent and apparent optical properties of water on solar altitude. *Limnol. Oceanogr.*, **29:** 350-356.

Loisel, H., and A. Morel, 1998: Light scattering chlorophyll concentration in case 1 waters: A reexamination. *Limnol. Oceangr.*, **43:** 847-858.

Loisel, H. and A. Morel, 2001: Non-isotropy of the upward radiance field in typical coastal (Case 2) waters. *Int. J. Remote Sensing*, **22:** 275-295.

Mobley, C.D., 1994: *Light and Water; Radiative Transfer in Natural Waters*. Academic Press, San Diego, California. 592pp.

Mobley, C.D., B. Gentili, H.R. Gordon, Z. Jin, G.W. Kattawar, A. Morel, P. Reinersman, K. Stamnes and R.H. Stavn, 1993: Comparison of numerical models for computing underwater light fields. *Appl. Opt.*, **32:** 7484-7504

Morel, A. and B. Gentili, 1991: Diffuse reflectance of oceanic waters: its dependence on sun angle as influenced by the molecular scattering contribution. *Appl. Opt.*, **30:** 4427-4438.

Morel, A. and B. Gentili, 1993: Diffuse reflectance of oceanic waters. II. Bidirectional aspects. *Appl. Opt.*, **32:** 6864-6879.

Morel, A. and B. Gentili, 1996: Diffuse reflectance of oceanic waters. III. Implication of bidirectionality for the remote sensing problem. *Appl. Opt.*, **35:** 4850-4862.

Morel, A. and S. Maritorena, 2001: Bio-optical properties of oceanic waters: A reappraisal. *J. Geophys. Res.*, **106:** 7163-7180.

Morel, A. and L. Prieur, 1977. Analysis of variations in ocean color. *Limnol. Oceanogr.,* **22**(4): 709-722.

Petzold, T.J., 1972: Volume scattering functions for selected ocean waters. SIO Ref. No. 72-78, Scripps Inst. of Oceanography, La Jolla, California, 79pp.

Preisendorfer, R.W. 1960: Recommendation on the standardization of concepts, terminology and notation of hydrologic optics. Scripps Inst. Of Oceanogr., SIO Report, 96pp.

Smith, R.C and K.S. Baker, 1978: The bio-optical state of ocean waters and remote sensing. *Limnol. Oceanogr.,* **23:** 247-259.

Chapter 5

Sun and Sky Radiance Measurements and Data Analysis Protocols

Robert Frouin[1], Brent Holben[2], Mark Miller[3], Christophe Pietras[4], Kirk D. Knobelspiesse[5], Giulietta S. Fargion[4], John Porter[6] and Ken Voss[7]

[1]*Scripps Institution of Oceanography, University of California, San Diego, California*
[2]*Biospheric Sciences Branch, NASA Goddard Space Flight Center, Greenbelt, Maryland*
[3]*Department of Applied Science, Brookhaven National Laboratory, Upton, New York*
[4]*SAIC General Sciences Corporation, Beltsville, Maryland*
[5]*Science Systems and Applications, Inc., Greenbelt Maryland*
[6]*School of Ocean & Earth Science & Technology, University of Hawaii, Hawaii*
[7]*Physics Department, University of Miami, Florida*

5.0 INTRODUCTION

This chapter is concerned with two types of radiometric measurements that are required to verify atmospheric correction algorithms and to calibrate vicariously satellite ocean color sensors. The first type is a photometric measurement of the direct solar beam to determine the optical thickness of the atmosphere. The intensity of the solar beam can be measured directly, or obtained indirectly from measurements of diffuse global upper hemispheric irradiance. The second type is a measurement of the solar aureole and sky radiance distribution using a CCD camera, or a scanning radiometer viewing in and perpendicular to the solar principal plane.

From the two types of measurements, the optical properties of aerosols, highly variable in space and time, can be derived. Because of the high variability, the aerosol properties should be known at the time of satellite overpass. Atmospheric optics measurements, however, are not easy to perform at sea, from a ship or any platform. This complicates the measurement protocols and data analysis. Some instrumentation cannot be deployed at sea, and is limited to island and coastal sites. In the following, measurement protocols are described for radiometers commonly used to measure direct atmospheric transmittance and sky radiance, namely standard sun photometers, fast-rotating shadow-band radiometers, automated sky scanning systems, and CCD cameras. Also discussed are methods of data analysis and quality control, as well as proper measurement strategies for evaluating atmospheric correction algorithms and atmospheric parameters derived from satellite ocean color measurements.

5.1 AUTOMATIC SUN PHOTOMETER AND SKY RADIANCE SCANNING SYSTEMS

The technology of ground-based atmospheric aerosol measurements using sun photometry has changed substantially since Volz (1959) introduced the first hand-held analog instrument almost four decades ago. Modern digital units of laboratory quality and field hardiness collect data more accurately and quickly and are often equipped for onboard processing (Schmid *et al*. 1997; Ehsani 1998, Forgan 1994; and Morys *et al*. 1998). The method used remains the same, *i.e.*, a detector measures through a spectral filter the extinction of direct beam solar radiation according to the Beer-Lambert-Bouguer law:

$$V(\lambda) = V_o(\lambda)\left(\frac{d_o}{d}\right)^2 \exp\left[-\left(\tau(\lambda)M\right)\right] t_g(\lambda), \tag{5.1}$$

where $V(\lambda)$ is the measured digital voltage, $V_o(\lambda)$ is the extra-terrestrial voltage, M is the optical air mass, $\tau(\lambda)$ is the total optical depth, λ is wavelength, d and d_o are respectively the actual and average earth-sun distances, and $t_g(\lambda)$ is the transmission of absorbing gases. The total optical depth is the sum of the Rayleigh and aerosol optical depth.

The earth-sun distance correction is calculated using the approximation

$$\left(\frac{d_o}{d}\right)^2 = 1 + 0.034\cos\frac{2\pi J}{365}, \tag{5.2}$$

where J is the number of the day of the year (Iqbal 1983).

Air mass $M(\theta_o)$ is a function of the sun zenith angle. Currently, the same value of air mass is used for Rayleigh, ozone, and aerosol factors. Air mass is calculated as

$$M = \left\{\cos\frac{\pi\theta_o}{180°} + 0.15*(93.885 - \theta_o)^{-1.253}\right\}^{-1}, \tag{5.3}$$

where the sun zenith angle θ_o is expressed in degrees.

Sky-scanning spectral radiometers that measure the spectral sky radiance at known angular distances from the sun have expanded the aerosol knowledge base. They provide, through inversion of the sky radiance, aerosol physical properties, such as size distribution, and optical properties, such as the aerosol scattering phase function (Nakajima *et al*., 1983, 1996; Tanré *et al*., 1988; Shiobara *et al*., 1991; Kaufman *et al*., 1994; Dubovik *et al*., 2000; and Dubovik and King, 2000). The inversion technique to calculate these aerosol properties requires precise aureole measurements near the solar disk and good stray-light rejection. Historically these systems are cumbersome, expensive, and not weather hardy. The CIMEL[10] and PREDE (French and Japanese manufacturers respectively) sun and sky scanning spectral radiometers overcome most of such limitations, providing retrievals of aerosol and water vapor abundance from direct sun measurements, and of aerosol properties from spectral sky radiance measurements. Since the measurements are directional and represent conditions of the total column atmosphere, they are directly applicable to satellite and airborne observations, as well as to studies of atmospheric processes. When equipped with a sophisticated tracking system with fast responding motors, the PREDE can be installed onboard a ship, or other moving platform, to monitor aerosol optical properties at sea. In the following, we focus on the CIMEL system, since the measurement protocols are similar for both CIMEL and PREDE systems.

Description

The CIMEL Electronique 318A spectral radiometer, manufactured in Paris, France, is a solar powered, weather hardy, robotically pointed sun and sky spectral radiometer. At each wavelength, this instrument has approximately a 1.2^o field-of-view (full angle) and filtered solar aureole and sky radiance. The 33 cm collimators were designed for 10^{-5} stray-light rejection for measurements of the aureole 3° from the sun. The robot mounted sensor head is pointed at nadir when idle to prevent contamination of the optical windows from rain and foreign particles. The sun/aureole collimator is protected by a quartz window, allowing observation with an ultraviolet enhanced silicon detector with sufficient signal-to-noise for spectral observations between 300 nm and 1020 nm. The sky collimator has the same 1.2^o field of view, but uses an order of magnitude larger aperture-lens system to improve dynamic range for measuring the sky radiance. The components of the sensor head are sealed from moisture and packed in desiccant to prevent damage to the electrical components and interference filters. Eight ion assisted deposition interference filters are located in a filter wheel rotated by a direct drive stepping motor. A thermistor measures the temperature of the detector, allowing compensation for any temperature dependence in the silicon detector.

A polarized model of the CE-318 is also used in SIMBIOS. This version executes the same measurement protocol as the standard model, but makes additional hourly measurements of polarized sky radiance at 870 nm in the solar principal plane (Table 5.1 and 5.2).

[10] Certain commercial equipment, instruments, or materials are identified in this document to foster understanding. Such identification does not imply recommendation or endorsement by the National Aeronautics and Space Administration, nor does it imply that the materials or equipment identified are necessarily the best available for the purpose.

Installation

The installation procedures for the CIMEL instrument are summarized below. More detailed information is available from the AERONET web page (http://aeronet.gsfc.nasa.gov).

The site should have a clear horizon and be representative of the regional aerosol regime. The basic assembly is relatively simple to mount. The cables are labeled clearly and most fit only in one place. Once the robot is assembled, it should be oriented so the zenith motor casing is pointing roughly east (the metal claw to which the sensor head is attached, then points to the west). The round connector end of the data cable should be attached to the sensor head, and the flat connector should be plugged into the white CIMEL control box. Strap the sensor head to the robot metal claw using the silver metal band. Make sure that the face of the sensor head is flush with the edge of the metal claw. Also, ensure that the long axis of the collimator cross-section is perpendicular to the axis of the zenith motor casing and claw. Verify that the robot itself is level. Do not use the embedded bubble level on top of the robot. Place the supplied bubble level on top of the flat ledge of the central robot tubular body (below the sensor head motor) This should be level in both the N/S and E/W axes. Verify that the CIMEL control box "TIME" and "DATE" are correct, *i.e.*, that they agree with the VITEL transmitter clock. If the Time or Date is wrong, the CIMEL will <u>not</u> find the sun on a "GOSUN" command.

Next, put the CIMEL in manual mode using the white control box display screen. In Manual mode, the main screen reads: "PW MAN SCN VIEW". Do a "PARK" procedure. When "PARK" is complete the sensor head collimator should be pointing down, perpendicular to the ground. Place the bubble level on the top of the metal claw arm and verify that this is level. If not, loosen the zenith bolt's hex nut (below the permanent bubble level on the top of the robot) and level it by rotating the zenith motor casing with your hand. Re-tighten the zenith nut tightly. It is important to perform another "PARK" procedure, or two, and make sure it is in fact level.

Using the right 2 buttons, change the display to read "GOSUN". Select "GO" to initiate. The sensor head should point to the sun. The hole at the top of the collimator should allow the sunlight to illuminate the marker spot at the base of the collimator. When the bright spot is on the mark, the instrument is aligned. If it is off to the left or right, rotate the robot base to align it. After you rotate the robot, you will need to verify that the robot is still level as before. Park the instrument and perform another "GOSUN" to check that the alignment is still good. If not, ensure that the robot is level, and that the sensor head is level when manually parked. One note: when you level the sensor head and do a "GOSUN", repeat this process a few times to be sure of the alignment. The first "GOSUN" after leveling is often not correct, because moving the sensor head while leveling can temporarily offset the robot's zeroing point. Re-parking the sensor and doing a second "GOSUN" should yield a more accurate alignment. Repeat this procedure until the alignment remains accurate and consistent on repetition.

Press "PW" then increment to 4, and place the instrument in "AUTO" mode. The main "AUTO" mode display should read: "PW AUTORUN VIEW". The CIMEL should be left in this mode in order to perform automatic measurement sequences.

The VITEL transmitter has a multi-level menu with "TIME DATE" etc in top level, and sub categories below each top-level item. The exact menu structure varies with software version (2.01, 2.9, and 2.11). Refer to the version most similar to your particular transmitter. One may operate the VITEL display by using the control buttons. To initiate an action, press the "SET-UP" button, and then press the "SCROLL" button repeatedly to view the categories in the current menu level. To choose any subcategory, press the "SELECT" button when the desired feature is shown in the display window. To change a parameter use the right 2 buttons "CHANGE" and "ENTER"". At any time, one may return to the previous (higher) menu level by pressing the "SET-UP" button.

Measurement Protocols

The radiometer makes only two basic measurements, either direct solar flux, or sky radiance. Each type of measurement involves several programmed sequences.

Direct sun measurements are made in eight spectral bands distributed between 340 nm and 1020 nm (440, 670, 870, 940 and 1020 nm are standard). Each measurement requires approximately 10 sec. A sequence of three such measurements are taken 30 sec apart creating a triplet observation per wavelength. Triplet observations are made during morning and afternoon Langley calibration sequences and at standard 15 min intervals in between (Table 5.1). The time variation of clouds is typically much greater than that of aerosols, and therefore significant variation

in the triplets may be used to screen cloud-contaminated measurements from the data. Variability over the 15 min interval also allows another check for cloud contamination at a lower frequency.

Sky measurements are performed at 440 nm, 670 nm, 870 nm and 1020 nm (Table 5.1). A single spectral measurement sequence (Langley sky) is made immediately after the Langley air mass direct sun measurement, with the sensor pointed 20° from the sun. This is used to assess the stability of the Langley plot analysis (O'Neill *et al.* 1984). Two basic sky observation sequences are made, "almucantar" and "principal plane". The objective of these sequences is to retrieve size distribution, phase function and aerosol optical thickness (AOT). This objective is approached by acquiring aureole and sky radiance observations spanning a large range of scattering angles, relative to the sun's direction, and assuming a constant aerosol profile.

An "almucantar sequence" is a series of measurements taken at the same sun elevation for specified azimuth angles relative to the Sun position. The range of scattering angles decrease as the solar zenith angle decreases, thus almucantar sequences made at an optical air mass of 2, or more, achieve scattering angles of 120°, or larger. Scattering angles of 120° are typical of many sun-synchronous viewing satellites, and thus a measure of the satellite path radiance is approximated from the ground station. During an almucantar measurement, observations from a single channel are made in a sweep at a constant elevation angle across the solar disk and continue through 360° of azimuth in about 40 sec (Table 5.2). This is repeated for each channel to complete an almucantar sequence. A direct sun observation is also made during each spectral almucantar sequence.

More than four almucantar sequences are made daily at optical air masses of 4, 3, 2 and 1.7, both morning and afternoon. An almucantar sequence is also made hourly between 9 AM and 3 PM local solar time for the standard instrument, and skipping only the noon almucantar for the polarization instrument.

The standard principal plane sky radiance measurement sequence is similar to the almucantar sequence, but the sensor scans in the principal plane of the sun, and therefore all angular distances from the sun are scattering angles, regardless of solar zenith angle. This measurement pointing sequence begins with a sun observation, moves 6° below the solar disk then sweeps through the sun's principal plane, taking about 30 sec for each of the four spectral bands (Table 5.2). Principal plane observations are made hourly when the optical air mass is less than 2 to minimize the variations in radiance due to the change in optical air mass.

Polarization measurements of the sky at 870 nm are an option with this instrument. The sequence is made in the principal plane at 5° increments between zenith angles of –85° and +85°. The configuration of the filter wheel requires that a near-IR polarization sheet be attached to the filter wheel. Three spectrally matched 870 nm filters are positioned in the filter wheel exactly 120° apart. Each angular observation is a measurement of the three polarization filter positions. An observation takes approximately 5 sec and the entire sequence about 3 min. This sequence occurs immediately after the standard measurement sequence in the principal plane.

Data Analysis

The present protocols adopt the data analysis procedures established for the AERONET program (Holben *et al*, 1998), with specific components and characteristics summarized in Table 5.3.

The AERONET *al*gorithms impose a processing standardization on all of the data taken in the network, thus facilitating comparison of spatial and temporal data between instruments.

A link from the SIMBIOS Web Page to the AERONET archival system allows the ocean color community to access either the raw, or processed, data via internet for examination, analysis and/or reprocessing, as needed. Alternatively a user may connect directly to the AERONET web page: aeronet.gsfc.nasa.gov.

The algorithms, inputs, corrections, and models used in computing the aerosol optical thickness, precipitable water (P_w), spectral irradiance, and sky radiance inversions are referenced in Table 5.3. The algorithms comprise two principal categories; time dependent retrievals such as AOT and P_w, and sky radiance retrievals such as size distribution, asymmetry parameter, single scattering albedo and complex index of refraction. As new and improved approaches and models are accepted within the community, the revised processing methods may be applied uniformly to the network-wide database. The specific implementation used by the SIMBIOS Project to compute AOT is described below in Sect. 5.5.

Sky radiance Inversion Products

Two alternative inversion algorithms are used retrieve optical properties of the aerosol in the atmospheric column: that of Nakajima *et al*. (1983, 1996) and the new algorithm developed by the AERONET Project (Dubovik and King 2000; Dubovik *et al*. 2000).

a) Inversions by the Nakajima et al. (1983, 1996) algorithms

The code inverts sky radiance in two ways:

1. simultaneously at four wavelengths (440 nm, 670 nm, 870 nm and 1020 nm) in the aureole angular range (scattering angle between 2.8^{o} and 40°; or
2. separately at each of four wavelengths (440 nm, 670 nm, 870 nm and 1020 nm) in the whole solar almucantar (scattering angle greater than 2.8^{o}) - option "single channel inversion".

The inversion assumptions are that aerosol particles are homogeneous spheres with a fixed index of refraction (1.45 – i 0.005). The retrieved variables are: $\frac{dV(r)}{d\ln r}$ (in $\mu m^{-3}/\mu m^{-2}$), the volume particle size distribution in range of sizes: 0.057 μm < r < 8.76 μm, plus the scattering optical thickness and phase function (including an asymmetry parameter) at the wavelengths 440 nm, 670 nm, 870 nm and 1020 nm.

b) Inversions by the new AERONET code (Dubovik and King 2000; Dubovik et al. 2000)

The code inverts $\tau_a(\lambda)$ and sky radiances simultaneously at four wavelengths (440 nm, 670 nm, 870 nm and 1020 nm) in the whole solar almucantar (scattering angles greater than 2.8^{o}). Aerosols are assumed to be homogeneous spheres, but the index of refraction is not fixed.

The retrieved variables are the volume particle size distribution $\frac{dV(r)}{d\ln r}$ [$\mu m^{-3}/\mu m^{-2}$] in the range of sizes 0.05 μm < r < 15 μm, the volume concentration, the mean and standard deviation of volume radius, and the effective aerosol radius for total (t), fine (f), and coarse (c) modes.

Note that the fine and coarse mode variables can be used only if the retrieved $\frac{dV(r)}{\ln r}$ is bi-modal. There is no automatic check for bi-modality. Also retrieved for wavelengths 440 nm, 670 nm, 870 nm, and 1020 nm are the real and imaginary parts of the complex refractive index, $m(\lambda) = n(\lambda) - i\, n'(\lambda)$, ($1.33 < n(\lambda) < 1.6$; $0.0005 < n'(\lambda) < 0.5$), the single scattering albedo, and the phase function (including its asymmetry parameter). It is assumed that particles in the range 0.05 μm - 0.6 μm are fine mode and those in the range 0.6 μm – 15 μm are coarse mode aerosols (Dubovik *et al*., 2000). This definition is not completely correct in all size distributions. Nevertheless, experience has shown it to hold true in the majority of practical cases.

Quality Control

The AERONET $\tau_a(\lambda)$ quality assured data are cloud screened following the methodology of Smirnov *et al*. (2000), and here we present just a brief outline of the procedure. The principal filters used for the cloud screening are based on temporal variability of the $\tau_a(\lambda)$, with the assumption being that greater temporal variance in τ_a is due to the presence of clouds. The first filter is a check of the variability of the three τ_a values measured within a one-minute period. If the difference between minimum and maximum $\tau_a(\lambda)$ within this one-minute interval is greater than 0.02 or $\tau_a(\lambda)$*0.03 then the measurement is identified as cloud contaminated. Then the remaining points are analyzed. If the standard deviation for $\tau_a(500)$ (optical thickness at 500 nm) is less than 0.015, then the entire day's data are passed. If not, the $\tau_a(\lambda)$ time series are checked for the presence of rapid changes or spikes in

the data. A filter based on the second derivative of the logarithm of $\tau_a(\lambda)$, as a function of time, is employed to identify rapid variations, which are then filtered as observations affected by clouds. This filter value is expressed as

$$D = \sqrt{\frac{1}{(N-2)}\sum_{i=1}^{N}\left[\frac{\ln(\tau_i)-\ln(\tau_{i+1})}{t_i - t_{i+1}} - \frac{\ln(\tau_{i+1})-\ln(\tau_{i+2})}{t_{i+1}-t_{i+2}}\right]^2} \tag{5.4}$$

where t_i is the time, expressed as the fraction of the day, for data point *i,* and N is the number of data points in the day. If the value of D is greater than 16, the day is deemed cloudy. The data point whose value contributed most to D is removed, and D is recalculated. This is repeated until the value for D falls below 16 or there are less than three points left (at which point all data for the day are rejected). After this, data whose $\tau_a(500)$ or Angstrom parameter, α, value exceeds three standard deviations from the mean for that day are rejected. Unscreened data are fully available from the AERONET homepage (aeronet.gsfc.nasa.gov). Automatic cloud screening of the almucantar and principal plane data is done by checking the distributions of data about the solar disc for symmetry and smoothness.

5.2 SKY RADIANCE DISTRIBUTION CAMERA SYSTEMS

Camera systems for sky radiance distribution are useful to collect the entire hemisphere of sky radiance data in a quick manner. The resulting data images usually contain the sun, so that the measurement geometry can be determined accurately and unambiguously. Also images can be checked for cloud contamination and other measurement artifacts more easily than can be done with data from scanning systems. The limitation of camera systems is that the dynamic range of the whole scene must be contained in each image. Therefore, the camera system must have large dynamic range and some method must be used to attenuate the direct sunlight before it strikes the imaging optics. To get a complete sky radiance distribution, including the solar aureole, it may be necessary to have an auxiliary system to measure the sky radiance near the sun (Ritter and Voss, 2000).

In addition, a sky radiance system, fitted with polarizers, can measure the Stokes parameters dealing with linear polarization (Voss and Liu 1997). These additional parameters are useful for investigating the polarization properties of the atmospheric aerosols and improving the aerosol optical models.

One of the most important areas of the sky radiance distribution to measure is near the horizon, opposite the sun, in the principal plane (the plane containing the sun and the zenith direction). This portion of the sky contains information on the large scattering angle portion of the atmospheric aerosol phase function, and it is very important for determining the aerosol optical properties relevant to atmospheric correction for ocean color satellites.

The second very important region of the sky is the solar aureole, the region near the sun. Because the aerosol scattering phase function is strongly peaked in the forward direction, information in this region is important in determining the aerosol single scattering albedo. Techniques for converting sky radiance measurements to aerosol properties have been described in Wang and Gordon (1993), Gordon and Zhang (1995) and Zhang and Gordon (1997a, 1997b).

An example of a camera system for sky radiance distribution is described in Voss and Zibordi (1989). The system described has been upgraded, for greater dynamic range, with a cooled CCD array. The basic system consists of a fisheye lens, a spectral/polarization filter changer, and a digital camera. To block direct sunlight from hitting the array, an occulter is manually adjusted to shadow the fish-eye lens. The size of the occulter is approximately ± 20° of the almucantar when the sun is at 60° zenith angle; the effect of the occulter is obvious in data images shown in Liu and Voss (1997). Four spectral filters select the wavelength range to be measured. Polarization filters are used to collect 3 planes of polarization in data images. These images can be combined to determine the linear polarization stokes vectors.

Measurement Protocols

Obviously, the first order requirement is that the field of view of the camera system is as unobstructed as possible, and that the measurement site is appropriately located with respect to the ship's stack exhaust. If the whole

field of view cannot be clear (as is usually the case), then one should try for a clear hemisphere, where data between obstructions in the other hemisphere can be used for checking the sky symmetry.

As the desired objective is to derive the aerosol scattering parameters, the sky must also be cloud free. Clouds cause two problems. The first is easy to detect and is the direct effect of having a bright cloud in the scene (in particular on the almucantar or principle plane). Almost any cloud will overwhelm the effect of aerosols in determining the sky radiance. This effect of clouds is usually quite evident in the sky radiance image. The second problem is the indirect effect of clouds shadowing aerosols and reducing the skylight caused by aerosol scattering. This second effect is more difficult to handle and places a more stringent requirement on the state of cloudiness during a measurement sequence. This effect can often be quite visible when the atmospheric aerosol loading is high, causing light beams to be evident in the aerosol layer. For these reasons, measurements with clouds present should be avoided if at all possible.

The maximum scattering angles existing in the sky radiance distribution occur near the horizon in the principle plane opposite the sun. For a given solar zenith angle, the maximum scattering angle is given by adding $\frac{\pi}{2}$ to the solar zenith angle. Since knowledge of the aerosol phase function at large scattering angles is important for the atmospheric correction process, measurements of the sky radiance distribution should be taken when the sun is at large zenith angles. The optimum angle is a compromise between getting large scattering angles and working too close to the horizon, where multiple scattering effects are large because of long optical paths through the atmosphere. A solar zenith angle of 60° has been chosen as optimum, because of these constraints.

Concurrent with the sky radiance measurements, it is important to measure the aerosol optical depth. By combining the aerosol optical depth and sky radiance distribution, the aerosol scattering properties can be determined, together with the single scattering albedo of the aerosols (Wang and Gordon, 1993; Gordon and Zhang, 1995; Zhang and Gordon, 1997a).

Data Analysis Protocols

Data reduction of the sky radiance data is very straightforward, and is described in Voss and Zibordi (1989). Basically with camera images, the data reduction process consists of simple image processing. Each image is multiplied by an absolute calibration factor and by an image that corrects for camera lens roll-off. This last factor is very important with a fisheye lens, because the important portion of the image is near the edge where the roll-off can become very significant. Once the image has been converted to radiometric data, specific areas can be selected for further analysis. In particular the almucantar and principal plane can easily be extracted for use in inversion routines.

Reduction of the sky radiance data to get the polarization properties is slightly more complicated. The current method is described in Voss and Liu (1997). Basically the Mueller matrix of the camera system is described as interacting with the Stokes vector of the skylight. There are three orientations of a linear polarizer in the system providing three separate Mueller matrices describing the camera system. For each sky direction (a pixel in the camera images), these Mueller matrices and the resultant intensities measured by the camera form a set of simultaneous equations with the unknowns being the sky Stokes vectors. For each pixel, these equations are inverted to obtain the Stokes vector of the skylight. While these images have been evaluated qualitatively (Liu and Voss, 1997), work is currently being done to do more quantitative inversions following the methods of Zhang and Gordon (1997b).

5.3 HAND-HELD SUN PHOTOMETERS

These instruments offer the simplest and most cost-effective means to collect data on aerosol optical thickness at sea. They are based on the measurement of the solar beam intensity, and therefore, the direct atmospheric transmittance. From this transmittance, after proper correction for attenuation by air molecules, the aerosol optical thickness may be obtained [equation (5.1)]. The technique is straightforward in principle. It is difficult for an observer to point the photometer at the sun accurately from a moving platform, but this difficulty is obviated with modern-day instruments. The value of these instruments also resides in the fact that, in most of the oceans, aerosol optical thickness measurements at the time of satellite overpass are sufficient to verify the atmospheric correction of ocean color (Schwindling *et al.* 1998). They allow one to estimate, via the Angstrom coefficient, the “pseudo” phase

function of the aerosols (the product of the single-scattering albedo and the phase function), a key atmospheric correction variable.

Many types of sun photometers have been built and are available commercially. In the following, we focus on two instruments, the MicroTops sun photometer, manufactured by Solar Light, Inc., and the SIMBAD radiometer, built by the University of Lille.

The NASA SIMBIOS Program maintains a set of these instruments for use during ocean-color evaluation cruises. The objective is to collect accurate aerosol optical thickness measurements during the ship cruises for comparison with values derived from satellite algorithms.

a) MicroTops

The Solar Light, Inc. MicroTops sun photometer is a hand held radiometer used by many investigators throughout the world. The popularity of MicroTops sun photometers is due to their ease of use, portability, and relatively low cost. The instruments have five channels whose wavelengths can be selected by interference filters. In order to follow the specifications given by the World Meteorological Organization (WMO), the wavelengths are typically chosen at 440 nm, 500 nm, 675 nm, and 870 nm, with an additional channel at 940 nm to derive integrated water vapor amounts. If an additional sun photometer is available, then it is also desirable to make measurements at 380 nm and 1020 nm.

The MicroTops sun photometers use photodiode detectors coupled with amplifiers and A/D converters. The collimators are mounted in a cast aluminum block with a 2.5^{o} full field of view. The MicroTops sun photometer has built-in pressure and temperature sensors and allows for a GPS connection to obtain the position and time. A built in microprocessor can calculate the aerosol optical depth, integrated water vapor, and air mass in real time and display these values on a LCD screen. Frequency of measurements is approximately 3 Hz. Temperature effects are corrected by taking dark count measurements with the lid covered on startup. Further information on MicroTops sun-photometers can be found in Morys (1998).

b) SIMBAD

The SIMBAD radiometer was designed - by the University of Lille - to measure aerosol optical thickness and diffuse marine reflectance, the basic atmospheric correction variables. The radiometric measurements are made in 5 spectral bands centered at 443 nm, 490 nm, 560 nm, 670 nm, and 870 nm. The ocean surface and the sun are viewed sequentially. The same 3° field-of-view optics, interference filters, and detectors are used in both ocean and sun viewing modes. A different electronic gain, low and high, is used for each mode, respectively. A third operating mode allows measurement of the dark current. The optics are fitted with a vertical polarizer to reduce reflected skylight when the instrument is operated in ocean-viewing mode (Fougnie *et al*., 1999). The polarizer does not affect the sun intensity measurements, because direct solar radiation is not polarized.

A GPS unit is attached to the instrument for automatic acquisition of geographic location at the time of measurement. Also acquired automatically are pressure, temperature, and view angles. Frequency of measurements is 10 Hz. In sun-viewing mode, only the highest intensity measured over one second is kept to avoid sun-pointing errors on a moving platform. Data is stored internally and downloaded onto diskette at the end of the day, or cruise. The instrument is powered with batteries, allowing six hours of continuous use. In normal use during a cruise (see below), the internal memory and batteries allow for three months of operations without downloading data or recharging the batteries.

Installation and Maintenance

The MicroTops and SIMBAD instruments need to be pointed at the sun manually. The sun is correctly aligned when its image appears in the cross hair on a small screen (MicroTops) or on a target (SIMBAD). After 10 min to 20 min of practice the user will become familiar with the pointing procedure and the process will become second nature. It is important to get familiar with this pointing procedure on land as ship based measurements require more skill.

The exterior of the instrument lenses can accumulate salt spray and should be inspected and cleaned if needed. For the open ocean, salt is the primary contaminant. Under these conditions, a lens tissue can be wet with clean

(filtered if possible) water or ethanol and used to remove the salt, then a dry lens tissue used to remove remaining water drops.

Faulty electronics pose a potential problem that is not always easy to detect when using MicroTops instruments. In the past it has been found that a leaky capacitor lowered the power and created erratic behavior for the shorter wavelengths where more gain is required. One can also get some idea of the instrument stability by taking numerous measurements with the lid covered. The voltage on all five channels should be less than ±0.03 mV. If the values are greater than this the unit should be sent back to the manufacturer for repair. Voltage variability will give some idea of the noise present in the photometer.

Measurement Protocols

During stable conditions (land or calm seas) pointing the radiometers at the sun is straightforward and most of the measurements will be accurate. Under rough ocean conditions, pointing at the sun can become the major source of uncertainty, with many of the measurements being off the sun. The measurements that are off the sun will have higher apparent aerosol optical depths, artifacts that positively bias the average. For data acquired under rough sea conditions, repeated measurements of aerosol optical depths are typically distributed in a comet shaped pattern, with a cluster of lower values and a tail extending to higher values. In these cases, the smaller optical depth values are more accurate and the larger values, which are likely due to pointing error, must be removed in post processing. Since many measurements may be discarded in post processing, it is suggested that 25, or more, measurements should be made within a short period of time (less than 5 min).

In general, the SIMBAD instrument is used alternatively in sun- and ocean-viewing mode. The sun intensity measurements also allow one to compute downwelled solar irradiance accurately in clear sky conditions, or when the sky is partly cloudy (<30 %) with the sun not obscured by clouds. The modeled values of solar irradiance are used to normalize water-leaving radiance measurements.

The recommended protocol is to make consecutively one "dark" measurement, three measurements in sun-viewing mode, one "dark" measurement, three measurements in ocean-viewing mode, one "dark" measurement, three measurements in sun-viewing mode, and one "dark" measurement. It requires about 15 min to collect a complete data set (ocean, sun, optical zero), including deploying the instrument and logging ancillary data (wind speed, sea state, cloud cover, etc.).

The current protocol (K. Knobelspiesse, Pers. Comm.) is to set the MicroTops to internally record the highest of 20 sequential measurements, and repeat the measurement at least 15 times. This procedure will allow measurements made when the instrument was not pointed accurately at the sun to be filtered and removed during post-processing.

The MicroTops sun photometer performs dark current measurements when it is first turned on. If the instrument's temperature changes subsequent to this dark current measurement, the calculated aerosol optical thickness value may be incorrect (Porter *et al*. 2000). Exposure to the sun for only a few minutes can have an effect, so the MicroTops should be turned off and on frequently. It is recommended that the MicroTops be shut off and on every ten seconds when making measurements, or after every five continuous measurements. Temperature variations should not be a problem for the SIMBAD, since the measurement protocol includes dark current measurements to be made before and after each set of *in situ* measurements.

On several instances we have found condensation to be a problem when radiometers were stored in an air-conditioned room prior to making measurements in the humid marine atmosphere. Condensation may occur outside the SIMBAD radiometer, but can also occur inside the MicroTops (*i.e.* it is not always possible to wipe it off). This problem can be avoided by storing the instrument at temperatures expected during measurement.

For the MicroTops sun photometer, the latitude, longitude and time can be set manually, or by connecting the GPS unit directly to the radiometer. Using either method, the time can be set to within one second of GMT. The latitude and longitude can also be stored in the MicroTops for measurements at fixed sites. The embedded GPS unit in the SIMBAD automatically acquires the geographic location and time at the beginning of each acquisition in the dark-current, sun-viewing, and ocean-viewing modes.

In order to maintain the quality of the aerosol optical thickness measurements, the procedures suggested above should be followed and the radiometers should be calibrated at least twice a year (more frequently if the calibration site is not stable – see Volume II, Chapter 4). When possible, it is also advisable to make measurements with two types of instruments. This redundancy will help to determine if any problems are occurring.

Data Analysis

Several types of external data need to be gathered to support the conversion from instrument voltages to aerosol optical thickness values. The air mass $M(\theta_o)$ must be calculated for the location and time of the measurement using equation (5.3). The optical depth values due to water vapor, ozone, trace gas and molecular scattering must all be determined and removed from the signal. Calculation of these values is described in detail in Section 5.5.

Once AOT values have been calculated, points representing erroneous measurements must be removed. It can be difficult to point a hand held sun photometer at the sun accurately from a moving platform, such as a boat at sea. Measurements taken when the instrument wasn't pointed at the sun will produce erroneous AOT values. A poorly pointed instrument mistakenly records less than the full direct solar radiance, so the computed AOT is much higher than reality. This is a significant problem with the MicroTops II sun photometer, as its measurement cycle of about 3 Hz is not always fast enough to avoid ship motion (Porter *et al*. 2000). This is less of a problem with the SIMBAD, as its measurement cycle is about 10 Hz.

Erroneous measurements from the SIMBAD are removed manually by plotting the data and removing large values that are not part of a systematic trend. Poor pointing artifacts will appear as noise, while real aerosol variations will have a more systematic behavior when plotted as a short time series. This visual inspection and removal of large values is done for each channel, as erroneous measurements in one channel may not affect another channel. This procedure is iterated until the optical depth variability does not exceed 20% of the average value, or until a threshold of 0.025 is obtained when the optical depths are below 0.08. This approach may slightly bias the data to lower values but it will remove the unrealistic larger values that would occur if the data were not filtered.

Two steps were taken to reduce the possibility of recording erroneous measurements with the MicroTops. First, the measurement protocol was changed. Unlike the default protocol, which saves the average of the 4 largest (out of 32) voltage values, the new protocol logs the largest single value of 20 measurements. This has several advantages. The largest voltage is the only value recorded, so the chance of keeping a contaminated point is minimized. In addition, the total time needed to make this measurement is smaller than with the default protocol, so more measurements can be taken in a short period of time. After the experiment, a post-processing algorithm is applied. This algorithm calculates the coefficient of variation (standard deviation divided by the mean) for each set of measurements in each band. If the coefficient of variation is above an arbitrary threshold of 0.05, the lowest voltage (highest AOT) value is removed, and the coefficient of variation is recalculated. This is repeated until the coefficient of variation is less than 0.05, or there are not enough points left to calculate the standard deviation. Only data points that pass this iterative process in all bands are accepted and retained.

5.4 FAST-ROTATING SHADOW-BAND RADIOMETERS

An estimate of τ_a can be made from calibrated measurements of the solar beam irradiance, $E_N(\lambda)$, at normal incidence when there are no clouds in front of the solar disk. Two sun photometer designs are commonly used to measure $E_N(\lambda)$: a narrow-beam detector mechanically pointed at the solar disk and a wide-field-of-view radiometer with a solar occulting apparatus. The first type of sun photometer requires careful angular positioning and can provide additional information about the forward scattering phase functions that help characterize the aerosol constituents. In contrast, a radiometer equipped with an occulting apparatus, known as a shadow-band radiometer, measures the diffuse and global (upper hemispheric) irradiance and computes $E_N(\lambda)$ from the difference between the two. The device gets its name from the hemispherical metal strip that rotates around the detector and blocks the direct solar beam to yield a signal that is from the sky only (after the effect of the arm is included).

The multiple-wavelength rotating shadow-band radiometer (Harrison *et al*., 1994) uses independent interference-filter-photodiode detectors and an automated rotating shadow-band technique to make spatially resolved measurements at seven wavelength pass-bands. The uncertainty of the direct normal spectral irradiance measurement made with this type of sun photometer is comparable with that made by narrow-beam tracking devices. A significant advantage of the shadow-band technique is that the global and diffuse irradiance measurements can be used to study the solar radiation budgets and the fractional cloud cover at the time of the measurement. The latter capability is particularly important for satellite validation studies. In the SIMBIOS context, direct solar and diffuse sky irradiances are critical terms for correcting down-looking in-water radiometers for self-shading (Volume III, Chapter 2).

A marine version of the multiple-wavelength rotating shadow-band radiometer has been developed at the Brookhaven National Laboratory (BNL). The BNL marine version uses a slightly modified version of the detector used for continental applications. It has seven channels: one broadband silicon detector and six ten-nm-wide channels at 415 nm, 500 nm, 610 nm, 660 nm, 870 nm, and 940 nm. Modifications to the detector circuitry used for continental applications are necessary, because the response time of the original circuitry is too slow for use on a moving ship. If the response time of the detector is too slow, wave action may cause the orientation of the radiometer to change appreciably during the time the shadow-band is occulting the sun. The rotation of the shadow-band itself must be sufficiently fast for the same reason. The marine version of the shadow-band radiometer is hereafter referred to as the BNL Fast-Rotating, Shadow-band Radiometer (FRSR). Implicit in this terminology is that the FRSR is a multi-filter or "spectral" radiometer.

The response of the silicon cell in the detector used for continental applications is faster than one millisecond, yet the internal preamplifiers have integrating low-noise amplifiers that slow the overall response. The response time of the detector is made faster for marine applications by reducing the magnitude of the low-pass filter capacitors. Laboratory tests do not show additional noise in the measurements as a result of this modification. The processing algorithms, which incorporate pitch, roll and heading measurements, are key to the instrument's ability to derive direct-normal beam irradiance without gimbals and a gyro-stabilized table.

Installation and Maintenance

The installation location of the instrument on a ship must be carefully selected. Ideally, FRSRs should be mounted in an exposed location as high as possible and free of nuisance shadows from other objects. This is often difficult. Radiation measurements on a ship always need to consider errors from the ubiquitous masts and antennas. A ship's communication antennas have highest vertical priority as do the running lights, and one must be careful of radar beams that can cause severe electronic noise. Once a suitable location has been found and the instrument mounted, the diffuser should be rinsed with distilled water and wiped with a moistened cloth at least once per day. The FRSR is typically mounted as a part of a portable radiation package that includes independent broadband solar and IR radiometers. The glass domes on these radiometers should be rinsed with distilled water and wiped with a moistened cloth.

Calibration is the most essential element of a radiation measurement program. A thorough and ongoing calibration process is required before the FRSR can make accurate radiometric measurements at sea. To ensure accurate measurements, there are two important elements for FRSR measurement protocol: calibration of the instrument circuitry, which includes temperature stabilization of the detector during measurements, and determination of the extra-terrestrial constants. These elements are discussed in Volume II, Chapter 4.

Data Analysis

The shadow-band radiometer must properly measure the global and diffuse irradiances from which the direct-beam solar irradiance is derived by the subtraction as

$$E_{\text{sun}}(\lambda) = E_{\text{S}}(\lambda) - E_{sky}(\lambda), \tag{5.5}$$

where $E_{\text{sun}}(\lambda)$ is the direct-beam solar incident irradiance projected onto a horizontal plane, $E_{\text{S}}(\lambda)$ is the global irradiance incident on the horizontal plane, and $E_{\text{sky}}(\lambda)$ is the diffuse incident irradiance from non-forward scattering. The global irradiance, $E_{\text{S}}(\lambda)$, is measured when the band is out of the field of view and the sensor is exposed to full sunlight. The irradiance normal to the incident solar beam is determined as

$$E_{\text{N}}(\lambda) = E_{\text{sun}}(\lambda)\sec\theta_{\text{o}}. \tag{5.6}$$

A correction for the amount of sky that is blocked by the occulting band is essential for an accurate measurement. An automatic correction for the shadowband is possible through measurement of ``edge" irradiance as is done with the land-based shadow-band radiometers. The shadow irradiance, $E_{\text{Shadow}}(\lambda)$, occurs when the sun is completely covered by the shadowband, but a portion of the diffuse irradiance is also blocked. The edge irradiance, $E_{\text{Edge}}(\lambda)$, is measured when the band is just to one side of the solar disk and provides a good estimate of the global irradiance minus the portion of sky that is blocked by the shadowband at the time it blocks the solar disk. In practice,

$E_{\text{Edge}}(\lambda)$ is selected from two measurements taken when the shadow is on one side or the other of the diffuser. Generally an average is taken, but in some cases in the early morning or late evening only one of the edges is acceptable. It is easy to show that the fully corrected direct solar incident irradiance is

$$E_{\text{sun}}(\lambda) = E_{\text{Edge}}(\lambda) - E_{\text{Shadow}}(\lambda). \tag{5.7}$$

With the fast-rotating technique, an advantage of using (5.7) to determine $E_{\text{sun}}(\lambda)$ is that the edge and shadow measurements are made in a very short time, which reduces noise significantly, especially on partly cloudy days. Also, if the electronics have a constant bias, the bias is removed by the subtraction. On a moving platform, some smoothing of the data is necessary. It was found that simple averages over a two-minute period (16 sweeps) would reduce the sampling uncertainty by a factor of approximately 4, and yield worst-case measurement uncertainties of about 5 W m^{-2} nm^{-1} for the global values and less than 1 W m^{-2} nm^{-1} for the shadow value. For perspective, two minutes is the approximate time for the sun to move by one diameter across the celestial sphere. A discussion and an example of the effectiveness of the two-minute averaging process are shown in Reynolds *et al.* (2000).

The shadow-band theory must be modified for a moving platform, when the radiometric collector head might not be oriented in a horizontal plane. Three measurement quantities for each channel are computed from the two-minute mean voltages: the global signal, V'_{G}, the shadow signal, V'_{S}, and the edge value, V'_{E}. The primes indicate the measurement is referenced to the plane of the head, which can be different than a horizontal plane. Two global measurements, V'_{G1} and V'_{G2}, are combined to produce the best estimate of global voltage, V'_{G}. The mean shadow voltage is V'_{S}. The edge value is selected from the two-minute composite sweep using an objective algorithm that accounts shadow width dependence on solar zenith and relative azimuth angles. The objective selection of the edge voltage uses one, or a mean of both, edge measurements to get the best estimate of V'_{E}. The voltage due to direct-beam irradiance falling onto the plane of the instrument is given by

$$V'_{\text{H}} = V'_{\text{E}} - V'_{\text{S}}. \tag{5.8}$$

This equation automatically corrects for the sky that is blocked by the shadow-band and also removes any bias term in the calibration equation. An important point in (5.8) is that the right-hand quantities are measured in a few tenths of a second, while the shadow crosses the diffuser. In such a short time interval the ship attitude changes insignificantly and interference from moving clouds is minimized. The diffuse component of the irradiance signal is computed from

$$V_{\text{D}} = V'_{\text{G}} - V'_{\text{H}}. \tag{5.9}$$

As we have stated previously, V_{D} is relatively unaffected by small amounts of platform motion.

The exact azimuth and elevation of the solar beam relative to the head must be computed from the following variables measured externally:

$$\{\theta_{\text{h}}, \phi_{\text{h}}\} = f(\phi_{\text{S}}, \alpha_{\text{P}}, \alpha_{\text{R}}, \theta_{\text{o}}, \phi_{\text{o}}), \tag{5.10}$$

where $\{\theta_{\text{h}}, \phi_{\text{h}}\}$ are the solar zenith and azimuth angles relative to the plane of the head, ϕ_{S} is the mean heading of the ship in true coordinates, α_{P} is the ship mean pitch, and α_{R} is the corresponding mean roll over the two-minute period. The solar azimuth and zenith angles in geographic coordinates, as seen by the observer, are θ_{o} and ϕ_{o}. Equation (5.10) represents three two-dimensional coordinate transformations in heading, pitch, and roll to shift the solar beam vector to a coordinate system aligned with the tilted FRSR head. The matrix transformation technique is well known and discussed in many textbooks on matrix algebra. Once θ_{h} and ϕ_{h} are determined, the calibration table can be consulted and an interpolated cosine-response correction value, $\gamma(\theta_{\text{h}}, \phi_{\text{h}})$, can be derived.

The response of the tilted instrument to the direct solar beam incident on the plane of its collector, V'_H, is converted to a direct-beam response for a plane normal to the solar beam using the relationship

$$V_{\text{N}} = \frac{V'_{\text{H}}}{\gamma(\theta_{\text{h}}, \phi_{\text{h}})\cos\theta_{\text{h}}}. \tag{5.11}$$

The global and horizontal voltages are re-computed for the Earth frame of reference:

$$V_{\text{H}} = V_{\text{N}} \cos\theta_{\text{o}}, \tag{5.12}$$

and

$$V_G = V_H + V_D. \tag{5.13}$$

The calibration equation is used to compute E_s, E_{sky}, E_{sun}, and E_N from the adjusted signals V_G, V_D, V_H, and V_N, respectively. From these terms, the Beer-Lambert-Bouguer law [equation (5.1)] can be used for estimating the calibration constant and $\tau_a(\lambda)$.

Cloud filtering is the most important challenge for FRSR data processing. Because the FRSR operates autonomously, cloud observations are naturally part of the signal that must be processed to obtain $\tau_a(\lambda)$. The cloud filter that is currently used is based on two steps: computing signal statistics over windows of periods of less than two hours and using these statistics to judge the quality of the observation under consideration. If the standard deviation of the observations in a two-hour moving window is less than 0.05, a subjectively defined threshold, and the observation at the center of the window is also less than 0.05, the central observation is accepted. The underpinning of this cloud filtering technique is that $\tau_a(\lambda)$ is relatively constant over a period of two hours, while the cloud signal is highly variable. This approach has proven relatively successful, although improvements in the filter are expected in the future.

5.5 SIMBIOS PROJECT AOT EXTRACTION PROTOCOLS

The SIMBIOS Project is concerned with ocean color satellite sensor intercomparisons and merger for biological and interdisciplinary studies of the global oceans. Imagery from different ocean color sensors can now be processed by a single software package using the same algorithms, adjusted by different sensor spectral characteristics, and the same ancillary meteorological and environmental data. This capability enables cross-comparisons to be made between similar data products derived from different satellite sensors. Internally consistent cross-validation of these products may then be approached by integrating *in situ* measurements of ocean and atmospheric parameters. The objective of these analyses is to merge the data products from the different satellites to provide continuity of ocean color information over long temporal and large spatial scales. Atmospheric correction of satellite radiances and, in particular, estimation of aerosol effects on the upwelling radiance at the top of the atmosphere, is one of the most difficult aspects of satellite ocean color remote sensing. Analyses comparing aerosol properties obtained from *in situ* observations with those derived from satellite ocean color sensor data are essential elements in the validation of the atmospheric correction algorithms. The uncertainty sources and magnitudes of AOTs determined from *in situ* measurements are discussed in earlier sections of this chapter. When the *in situ* measurements are matched against atmospheric properties derived using data from a satellite sensor, additional uncertainties result from the different viewing angles of the satellite and surface instruments, and from discrepancies in time between the satellite and *in situ* observations. In the case of the atmosphere, these uncertainties are considerable. The uniform calibration, measurement, data analysis and quality control protocols described in this chapter are designed to minimize these overall sources of uncertainty.

Extraction of in situ AOT

The Project has recently implemented its own correction strategy for instrument voltages corresponding to AOT. The approach ensures a uniform AOT processing for all instruments, making the AOTs comparable amongst the instruments, and between instruments and satellite sensor AOTs derived by means of the atmospheric correction. Also, the method uses a consistent set of tuning variables, such as ancillary data, concurrently applied for the correction of satellite radiances. Therefore, some stages of the satellite and *in situ* data processing are identical, contributing to increasing confidence in the match-ups.

First, instrument-specific procedures are used to retrieve sun intensity measurements, $V(\lambda)$, from individual sun photometers. In the case of the shadow-band radiometer, the data must be processed to determine direct beam intensity on a plane normal to the solar beam [equations (5.10) and (5.11)]. The following processing is otherwise uniform for all instruments, taking account, however, of the distinct spectral wavelengths used by each sensor.

The Beer-Lambert-Bouguer law (equation 5.1) can be expanded as

$$V(\lambda) = V_o(\lambda) * \left(\frac{d_o}{d}\right)^2 e^{-M(\theta_o)\left[\tau_R(\lambda)+\tau_{O_3}(\lambda)+\tau_a(\lambda)\right]}, \tag{5.14}$$

where τ_R, τ_{O3},and τ_a are the molecular (Rayleigh) and ozone and aerosol optical thickness, respectively, and the other terms have been previously defined. Equation (5.14) assumes that the signal, $V(\lambda)$, is measured when the instrument is pointing directly at the sun and that gaseous absorption is only due to ozone.

The earth-sun distance adjustment, $(d_0/d)^2$ and air mass, M, are calculated using equations 5.2 and 5.3, respectively. Currently, the same value of air mass M is used for Rayleigh, ozone, and aerosol factors.

The desired AOT, τ_a, is extracted from equation (5.14) by calculating all other variables, using known constants from references in Table 5.3, and measured ancillary data. The following estimations of earth and atmospheric parameters to obtain AOT coincide with the SeaWiFS satellite sensor correction, including the choice of meteorological and ozone ancillary data.

Rayleigh optical thickness is calculated using contemporary atmospheric pressure readings obtained from the daily global pressure maps provided by the National Centers for Environmental Prediction. The Rayleigh optical thickness is extracted as

$$\tau_R(\lambda) = k_{Ray}(\lambda) * e^{-\frac{A}{7998.9}} * \frac{P}{P_o}, \tag{5.15}$$

where A is the altitude in m, P is the current atmospheric pressure in hPa, P_o is the standard atmospheric pressure of 1013.25 hPa (Kasten and Young 1989). The quantity k_{Ray} is defined as

$$k_{RAY}(\lambda) = \frac{28773.597886}{\lambda^4}\left\{4\left[g(\lambda)\right]^2 + 4\left[g(\lambda)\right]^3 + \left[g(\lambda)\right]^4\right\}, \tag{5.16}$$

where

$$g(\lambda) = \left[8342.13 + \frac{2406030}{130-\lambda^{-2}} + \frac{15997}{38.9-\lambda^{-2}}\right]\times 10^{-8}, \tag{5.17}$$

and wavelength λ is in μm and the coefficients are taken from Penndorf (1957), Elden (1966) and Young (1980).

The ozone optical thickness is acquired from spatial and temporal interpolation of daily satellite global measurements of ozone amounts. Preferably, ozone data are determined from the Total Ozone Mapping Spectrometer (TOMS) data. If TOMS data are unavailable, ozone counts from the TIROS Operational Vertical Sounder (TOVS) are used. Finally, if TOVS data are missing, ozone climatology files are applied. The ozone optical thickness is calculated from the ozone amount, in *Dobson* units, using a scaling factor $k_{oz}(\lambda)$,

$$\tau_0(\lambda) = k_{oz}(\lambda) * \frac{Dobson}{1000}, \tag{5.18}$$

where $k_{oz}(\lambda)$ is the specific absorption coefficient (per *Dobson*) given below for the following spectral bands (Nicolet at al., 1981):

λ = (315, 340, 380, 400, 415, 440, 443, 490, 500, 560, 610, 660, 670, 675, 862, 870, 936, 1020 nm);

and

k_{oz} (λ) = (1.35, 0, 0.00025, 0.00065, 0.00084, 0.0034, 0.00375, 0.02227, 0.0328, 0.10437, 0.12212, 0.05434, 0.04492, 0.0414, 0.00375, 0.0036, 0, 0).

REFERENCES

Bass, A.M. and R.J. Paur, 1984: The ultraviolet cross-section of ozone:1. *The measurements, in Atmospheric Ozone*, edited by C.S. Zerefos & A. Ghazi, pp. 606-610, Reidel, Dordrecht.

Bruegge, C.T., J.E. Conel, R. O. Green, J.S. Margolis, R.G. Holm, and G. Toon, 1992: Water vapor column abundance retrievals during FIFE. *J.Geophys. Res*., **97**(D19), 18759-18768.

Burcholtz, A., 1995: Rayleigh-scattering calculations for the terrestrial atmosphere, *Appl. Opt.,* **34**, 2765-2773.

Dubovik**,** O. and M.D.King,, 2000: A flexible inversion algorithm for retrieval of aerosol optical properties from Sun and sky radiance measurements, *J. Geophys. Res*., (submitted).

Dubovik, O., A.Smirnov, B.N.Holben, M.D.King, Y.J. Kaufman, T.F.Eck, and I.Slutsker, 2000: Accuracy assessments of aerosol optical properties retrieved from AERONET Sun and sky-radiance measurements, *J. Geophys. Res*., **105**, 9791-9806.

Edlen, B., 1966: The refractive Index of Air, *Meteorol*., **2**, 71-80.

Ehsani, A. R., J. A. Reagan, and W. H. Erxleben, 1998: Design and performance analysis of an automated 10-channel solar radiometer instrument, *J. Atmos. Ocean. Tech*., *15*, (in press).

Forgan, B.W., 1994: General method for calibrating Sun photometers, *Applied Optics*, **33**, 4841-4850.

Fougnie, B., R, Frouin, P. Lecomte, and P-Y. Deschamps, 1999: Reduction of skylight reflection effects in the above-water measurement of marine diffuse reflectance. *Applied Optics*, **38**, 3844-3856.

Gordon, H. R., J. W. Brown, and R. H. Evans, 1988: Exact Rayleigh scattering calculations for use with the Nimbus-7 coastal zone color scanner, *Applied Optics*, **27**, 862-871.

Gordon, H.R., and K. Ding, 1992: Self shading of in-water optical instruments. *Limnol. Oceanogr.,* **37**, 491--500.

Gordon, H. R. and T. Zhang, 1995: Columnar aerosol properties over oceans by combining surface and aircraft measurements: simulations. *Applied Optics*, **34**, 5552 – 5555.

Hansen, J. E., and L. D. Travis, 1974: Light scattering in planetary atmospheres. *Space Sci. Rev.*, **16**, 527-610.

Harrison, L. and J. Michalsky, 1994: Objective algorithms for the retrieval of optical depths from ground-based measurements, *Applied Optics*, **33** ,5126-5132.

Harrison, L., J. Michalsky, and J. Berndt, 1994: Automated multi-filter rotating shadow-band radiometer: an instrument for optical depth and radiation measurements, *Applied Optics,* **33,** 5126-5132.

Holben, B.N., T. F.Eck, I.Slutsker, D.Tanre, J.P.Buis, A.Setzer, E.Vermote, J.A.Reagan, Y.Kaufman, T.Nakajima, F.Lavenu, I.Jankowiak, and A.Smirnov 1998: AERONET - A federated instrument network and data archive for aerosol characterization, *Rem. Sens. Environ*., **66**, 1-16.

Iqbal., M., 1983: *An introduction to Solar Radiation,* Academic, San Diego, Calif., 390 pp.

Kasten F. and A. T. Young, 1989: Revised optical air mass tables an approximation formula, *Applied Optics***, 28**: 4735-4738.

Kaufman, Y.J., A. Gitelson, A. Karnieli, E. Ganor, R.S. Fraser, T. Nakajima, S. Mattoo, B.N. Holben, 1994: 'Size Distribution and Phase Function of Aerosol Particles Retrieved from Sky Brightness Measurements', *J. Geophys. Res.,* **99**, 10341-10356.

Kneizys, F.X., E.P. Shettle, L.W. Abreu, J.H. Chetwynd, G.P. Anderson, W.O. Gallery, J.E.A. Selby, and S.A. Clough, 1988: Users Guide to LOWTRAN 7, AFGL-TR-88-0177, (NTIS AD A206773), Air Force Geophysics Laboratory, Hanscom Air Force Base, Massachusetts.

Komhyr, W. D., R. D. Grass, and R. K. Leonard, 1989: Dobson Spectrophotometer 83: a standard for total ozone measurements, 1962-1987, *J. Geophys. Res*., **94,** 9847-9861.

Liu, Y. and K. J. Voss, 1997: Polarized radiance distribution measurements of skylight: II. experiment and data. *Applied Optics*, **36**,8753 - 8764.

London, J., R. D. Bojkov, S. Oltmans, and J. I. Kelley, 1976: Atlas of the global distribution of total ozone July 1957 - June 1967, *NCAR Technical Note 133+STR*, National Center for Atmospheric Research, Boulder, Colorado, 276 pp.

Michalsky, J. J., 1988: The astronomical almanac's algorithm for approximate solar position (1950 - 2050), *Solar Energy*, **40**, 227 - 235.

Morys, M., F.M. Mims III, and S.E. Anderson, 1998: Design, calibration and performance of MICROTOPS II hand-held ozonometer.

Nakajima, T., M. Tanaka and T. Yamauchi, 1983: Retrieval of the optical properties of aerosols from aureole and extinction data. *Applied Optics*, **22**, 2951-2959.

Nakajima, T., G. Tonna, R. Rao, P. Boi, Y. Kaufman, and B. Holben, 1996: Use of sky brightness measurements from ground for remote sensing of particulate polydispersions, *Applied Optics*, **35**, 2672-2686.

Nicolet M., 1981: The solar spectral irradiance and its action in the atmospheric photodissociation processes, Planet. *Space Sci*., **29**, 951-974.

Penndorf, R., 1957: Tables of the Refractive Index for Standard Air and the Rayleigh Scattering Coefficient for the Spectral Region Between 0.2 and 20.0 Microns and their Application to Atmospheric Opt., *J. Opt. Soc. Am*., **47,** 176-182.

Porter, J. N., M. Miller, C. Pietras, and C. Motell, 2000: Ship-based sun photometer measurements using MicroTops sun photometers*, J. Ocean. Atmos. Tech*. (in press).

Reagan, J.A., K.J. Thome, and B.M. Herman, 1992: A simple instrument and technique for measuring columnar water vapor via Near-IR differential solar transmission measurements. *IEEE Trans. Geosci. Remote Sensing*, **30**, 825-831.

Reynolds, R.M., M.A. Miller, and M.J. Bartholomew, 2000: Design, Operation, and Calibration of a Shipboard Fast-Rotating Shadow-band Spectral Radiometer, *Jour. Atmos. Ocean. Tech*., (accepted).

Ritter, J. M. and K. J. Voss, 2000: A new instrument to measure the solar aureole from an unstable platform. J. Atmos. Ocean. Tech., in press.

Schmid, B., C. Matzler, A. Heimo and N. Kampfer, 1997: Retrieval of Optical Depth and Particle Size Distribution of Tropospheric and Stratospheric Aerosols by Means of Sun Photometry, *IEEE Trans. on Geosci. and Rem Sens*., **15**, 172-182.

Schwindling, M., P.-Y. Deschamps, and R. Frouin. 1998: Verification of aerosol models for satellite ocean color remote sensing. *J. Geophys. Res.,* 24,919-24,935.

Shaw, G. E., 1983: Sun Photometry, *Bull. Amer. Meteor. Soc.*, **64**, 4-11.

Shiobara, M., T. Hayasaka, T. Nakajima and M. Tanaka, 1991: Aerosol monitoring using a scanning spectral radiometer in Sendai, Japan. *J. Meteorol. Soc. of Japan***, 60**, 57-70.

Smirnov, A., B.N.Holben, T.F.Eck, O.Dubovik, and I.Slutsker, 2000: Cloud screening and quality control algorithms for the AERONET data base. *Rem. Sens. Environ*., (accepted).

Tanré, D., C. Devaux, M. Herman and R. Santer, 1988: Radiative properties of desert aerosols by optical ground-based measurements at solar wavelengths. *J. Geophys. Res*., **93**, 14223-14231.

Tanré, D., C. Deroo, P. Duhaut, M. Herman, J.-J. Morcrette, J. Perbos, and P.-Y. Deschamps, 1990: Description of a computer code to simulate the signal in the solar spectrum: the 5S code. *Int. J. Remote Sensing*, **11**, 659-668.

Vigroux, E., 1953: Contribution a l'etude experimentale de l'absorption de l'oxone, *Annales de Phys*., **8**, 709.

Volz, F.E., 1959: Photometer mit Selen-photoelement zurspektralen Messung der Sonnenstrahlung und zer Bestimmung der Wallenlangenabhangigkeit der Dunsttrubung. *Arch. Meteor. Geophys Bioklim*. **B10**, 100-131.

Voss, K. J. and Y. Liu, 1997: Polarized radiance distribution measurements of skylight: I. system description and characterization. *Applied Optics*, **36**, 6083-6094.

Voss, K. J., 1989: Electro-optic camera system for measurement of the underwater radiance distribution. *Optical Engineering*, **28**, 241-247.

Voss, K. J. and G. Zibordi, 1989: Radiometric and geometric calibration of a spectral electro-optic "fisheye' camera radiance distribution system. *J. Atmos. Ocean. Tech*.., **6**, 652-662.

Wang, M. and H. R. Gordon, 1993: Retrieval of the columnar aerosol phase function and single-scattering albedo from sky radiance over the ocean: simulations. *Applied Optics*, **32**,4598 – 4609.

Young, A.T., 1980: Revised Depolarization Corrections for Atmospheric Extinction, *Applied Optics*, **19**, 3427-3428.

Zhang, T. and H. R. Gordon, 1997a: Columnar aerosol properties over oceans by combining surface and aircraft measurements: sensitivity analysis. *Applied Optics***, 36**, 2650 – 2662.

Zhang, T. and H. R. Gordon, 1997b: Retrieval of elements of the columnar aerosol scattering phase matrix from polarized sky radiance over the ocean: simulations. *Applied Optics,* **36**,7948 – 7959.

Table 5.1: Measurement sequences of the CIMEL Sun/Sky scanning spectral radiometer.

	Spectral Range nm	**Target**	**No. Obs.**	**Obs. Interval**	**Application**
BASIC DIRECT SUN	340 to 1020	Sun	1 each λ	~ 8 sec. for. 8 λ	AOT, Pw, α
Triplet Observation	340 to 1020	Sun	Three direct sun	3 @ 30 sec. apart, 1 min total	AOT, Pw, α & cloud screening
Standard Measurement Sequence	340 to 1020	Sun	Variable: depends on day length	Ea. 15 min m=2 AM to m=2 PM	AOT, Pw, α
Langley	340 to 1020	Sun	16, am & PM between m 7 & 2	m=7 - 5, incr of.5 m m=5 - 2, incr. of.25	Langley, Cal., AOT, Pw, α
BASIC SKY	440 to 1020	Sky	1 each λ	none	Sky Radiance
Langley sky	440 to 1020	Sky	16 between m 7 & 2	m=7 - 5,.5; m=5- 2,.25	Stability of Lngly Plot
Almucantar	440 to 1020	Sky	72 (Table 2)	>8/day: m= 4, 3, 2, 1.7 hrly 9AM to 3PM	Size Dist. and P(θ), AOT, α
Polarization	870	Sky	42 (Table 2)	hourly m=3 AM to m=3 PM	Size Dist. and P(θ)
Principal Plane	440 to 1020	Sky	42 (Table 2)	hourly m=3 am to m=3 PM	Size Dist. and P(θ) AOT, α

Table 5.2: Almucantar and Principal Plane sequences for the standard and polarization instruments.		
	Sun	**Sky (°)**
ALMUCANTAR Azimuth angle relative to sun	0°	6.0, 5.0, 4.5, 4.0, 3.5, 3.0, 2.5, 2.0, -2.0,-2.5, -3.0, -3.5, -4.0, -4.5, -5.0, -6.0, -8.0, -10.0, -12.0, -14.0, -16.0, -18.0, -20.0, -25.0, -30.0, -35.0, -40.0, -45.0, -50.0, -60.0, -70.0, -80.0, -90.0, -100.0, -110.0, -120.0, -130.0, -140.0, -160.0, -180.0 Duplicate above sequence for a complete counter clockwise rotation to –6
PRINCIPAL PLANE: Standard Scattering Angle from sun (negative is below the sun)	0°	-6.0, -5.0, -4.5, -4.0, -3.5, -3.0, -2.5, -2.0, 2.0, 2.5, 3.0, 3.5, 4.0, 4.5, 5.0, 6.0, 8.0, 10.0, 12.0, 14.0, 16.0, 18.0, 20.0, 25.0, 30.0, 35.0, 40.0, 45.0, 50.0, 60.0, 70.0, 80.0, 90.0, 100.0, 110.0, 120.0, 130.0, 140.0
PRINCIPAL PLANE: Polarization Scattering Angle from sun (negative is in the anti solar direction)	-	-85.0, -80.0, -75, -70, -65.0, -60.0, -55.0, -50.0, -45.0, -40.0, -35.0, -30.0, -25.0, -20.0, -15.0, -10.0, -5.0, 5.0, 10.0, 15.0, 20.0, 25.0, 30.0, 35.0, 40.0, 45.0, 50.0, 55.0, 60.0, 65.0, 70.0, 75.0, 80.0, 85.0

Table 5.3: Procedure of the AERONET Program		
Variable, algorithm or correction	**Comments**	**References**
Basic Computations		
Rayleigh Optical Depth, τ_r refractive index of air depolarization factor	Input elevation in m	Penndorf, 1957 Edlen, 1966 Young, 1980 Burcholtz, 1995
Solar Zenith Angle, θo		Michalsky, 1988
Earth sun distance, d		Iqbal, 1983
Ozone amount, O_3	Table lookup by 5° lat. long.	London *et al*., 1976
Aerosol optical air mass, m_a		Kasten and Young, 1989
Rayleigh optical air mass, m_r		Kasten and Young, 1989
O_3optical air mass, m_o		Komhyr *et al*., 1989
Corrections		
Temperature, T	~0.25%/°C for 1020 nm specific for each inst.	Hamamatsu Inc. and Lab measurements
Water Vapor for 1020 AOT	from Pw retrieval, Lowtran	Kneizys *et al*, 1988
Rayleigh, all wavelengths	from elevation	
O_3 abs. coef. $\lambda > 350$ nm		Vigroux, 1953
O_3 abs. coef. $\lambda < 350$ nm		Bass and Paur, 1984
Time, t	CIMEL, UTC, DAPS time stamps, ±1 second	Refer to Homepage
Retrievals		
Spectral direct Sun AOT,Langley Plots	Beer's Law	Shaw, 1983
Pw: (a, k, Vo)	Modified Langley	Bruegge *et al*., 1992; Reagan *et al*., 1992
Size Dist., Phase function	From spectral sky radiance	Nakajima *et al*., 1983 Dubovik and King, 2000
Procedures		
Cloud Screening	Thresholds, λ AOT & t	Smirnov *et al*., 2000
Climatology, Direct Sun	AOT, Pw, Wavelength Exp.	Refer to Homepage
Climatology, Sky	Size Dist., Phase function, g	Refer to Homepage